Doctoral Dissertations Student Scholarship

Fall 2008

Surface structure and composition determination by low-energy electron scattering and Monte Carlo simulations

Jiebing Sun
University of New Hampshire, Durham

Follow this and additional works at: https://scholars.unh.edu/dissertation

SURFACE STRUCTURE AND COMPOSITION DETERMINATION BY LOW-ENERGY ELECTRON SCATTERING AND MONTE CARLO SIMULATIONS

BY

Jiebing Sun

B.S., Wuhan University (1999)
M.S., Wuhan University (2002)

DISSERTATION

Submitted to the University of New Hampshire
in partial fulfillment of
the requirements for the degree of

Doctor of Philosophy

in

Physics

September, 2008

UMI Number: 3333529

INFORMATION TO USERS

The quality of this reproduction is dependent upon the quality of the copy submitted. Broken or indistinct print, colored or poor quality illustrations and photographs, print bleed-through, substandard margins, and improper alignment can adversely affect reproduction.

In the unlikely event that the author did not send a complete manuscript and there are missing pages, these will be noted. Also, if unauthorized copyright material had to be removed, a note will indicate the deletion.

UMI®
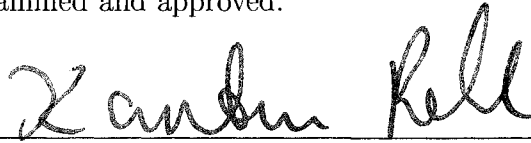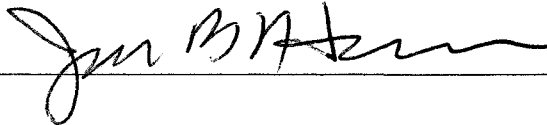
This dissertation has been examined and approved.

Karsten Pohl

Dissertation Director, Associate Professor of Physics

James B Hannon

Dissertation Co-Director, IBM Watson Research Center

Olof E. Echt

Professor of Physics

James M. E. Harper

Professor of Physics

Martin A. Lee

Professor of Physics

08/14/08

Date

DEDICATION

To my parents.
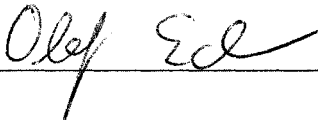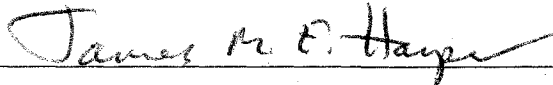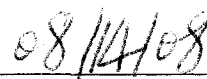
ACKNOWLEDGMENTS

In the journey to my PhD degree, many people gave me endless help. Without their help, this work would not have been possible. Hereby I would like to express my sincerest gratitude to all of them.

I am deeply indebted to my academic adviser, Professor Karsten Pohl. His guidance and encouragement brought me tremendous enthusiasm and inspiration which led me to today's fulfillment of the PhD work. His readiness for research discussions helped me go through all the difficulties and achieve more. His care for various aspects of my research - the teaching, the travel grants and the introduction to collaborative work - is highly appreciated.

Dr. James B. Hannon, from IBM Thomas J. Watson Research Center, is the one I have been frequently contacting in the last several years. He is both my research co-adviser and a collaborator. I learned a lot from him, in both experiments and numerical simulations. I feel extremely lucky to have been working with such a wonderful research partner.

Professor Philip Hofmann, the Director of the Institute for Storage Ring Facilities at the University of Aarhus in Denmark, offered me generous use of the LEED facility in his lab. Graduate students Justin Wells and Maria F. Jensen in Philip's lab provided much help in the experiment on the Bi(001) surface.

The collaborating group, Dr. Gary L. Kellogg and Dr. Ezra Bussmann, is from the Sandia National Laboratories at Albuquerque, New Mexico. I want to say special thanks to Dr. Kellogg for offering me a precious opportunity to work on their LEEM equipment. During my visit, he helped me much in both research and life. He picked me up from the

TABLE OF CONTENTS

LIST OF TABLES

LIST OF FIGURES

xxiii

ABSTRACT

SURFACE STRUCTURE AND COMPOSITION DETERMINATION BY LOW-ENERGY
ELECTRON SCATTERING AND MONTE CARLO SIMULATIONS

by

Jiebing Sun
University of New Hampshire, September, 2008

This thesis reports on surface and surface alloy structural and compositional determination with low-energy electron scattering and Monte Carlo simulations. Low-energy electron diffraction (LEED) technique and the newly developed low-energy electron microscopy (LEEM) IV technique are used to measure the electron scattering intensity spectra and dynamical multiple scattering analysis is performed to optimize the surface structural and non-structural parameters via comparison between the experimental spectra and calculated ones. My work focuses on the following four surface systems.

(111), (110) and (001) surface structures of the semimetal bismuth are determined with LEED. The unreconstructed (1×1) structure is revealed for all three surfaces. The interlayer spacings for several outermost layers are resolved. All results agree with those obtained by first-principles calculations. The Debye temperatures for the Bi(111) and Bi(110) surface are found to be lower than that of the Bi bulk. In conjunction with the LEED technique, scanning tunneling microscopy (STM) observation is performed on the Bi(001) surface. Surface topology images show dominant bilayer steps and no single layer step.

The newly developed LEEM-IV technique is used to investigate the PdCu surface alloy on the substrate Cu(001). Studies include quantifying the temporal evolution of Pd concentration on the Cu(001) terrace, mapping the 3D heterogeneous surface chemical compo-

sition, and identifying a step-overgrowth thin film growth mechanism. It is found that, at the initial deposition stages, Pd atoms reside in the second layer at the sample temperature of 473 K, and the Pd concentration increases exponentially with time. The heterogeneous structure and composition near the steps are found to be a result of the step-overgrowth. We highlight the LEEM-*IV* technique which provides a high lateral resolution at surfaces. We demonstrate a 3D profile of Pd concentration in the surface region by using the LEEM-*IV* technique.

The reconstructed Si(001)-2×1 surface has been intriguing due to its great scientific and technical significance. Unfortunately, no satisfactory agreement between the LEED experimental and theoretical data have been achieved. Some controversies over this surface, such as the flip-flop dimer dynamics and the ground-state structure, still require further study. Utilizing LEEM to get electron scattering spectra from a single domain, we get a refined asymmetric tilted dimer structure.

We investigate the 6H-SiC(0001) surface phase transition in order to ultimately understand the formation of graphene on it. LEEM diffraction data from a large single domain are analyzed for 3×3, 1×1 and $\sqrt{3}\times\sqrt{3}$ phases. All the surface structures turn out to have an "A" bi-layer bulk termination. It is found that the amount of Si at the surface decreases with increased temperature. Adatom-trimer-adlayer model for the 3×3 surface does not give a satisfactory result and more work needs to be done to resolve this structure. A mixed Si-vacancy top-site overlayer on the 1×1 surface is found. A $\sqrt{3}\times\sqrt{3}$ overlayer at the T4 registry on the substrate surface generates a best fit between experimental and calculated data.

CHAPTER 1

Introduction

1.1 Surface science

Surface science is the study of physical and chemical phenomena that occur at the interface of two phases, including solid-liquid interfaces, solid-gas interfaces, solid-vacuum interfaces, and liquid-gas interfaces. It encompasses concepts such as heterogeneous catalysis, semiconductor device fabrication, fuel cells, self-assembled monolayers, abrasion, erosion, adhesives and thin-film growth. Surface science is of interest mainly due to its four characters: abundant chemical compositions and geometrical structures, intriguing electronic structures, remarkable physical properties, and challenging surface techniques. A variety of surface phenomena, such as phase transitions, optical properties, adsorption, surface reactions and thin-film growth, have been extensively investigated.

Partially because of its historical development, surface science is roughly divided into two scientific fields: surface chemistry and surface physics [7]. Surface science began with surface chemistry which centers on the study of reactions at interfaces. Some research directions in surface chemistry are surface functionalization, heterogeneous catalysis, surface adsorption, and interface study. Irving Langmuir was one of the founders of this field in the early 20th century. He was awarded the 1932 Nobel Prize in Chemistry for his discoveries and investigations in surface chemistry [8]. 75 years later, German physicist Gerhard Ertl was

awarded the 2007 Nobel Prize in Chemistry for his studies of chemical processes on solid surfaces [8].

In contrast, surface physics, which concentrates on the study of physical changes at interfaces [3], emerged as late as the 1960s. Some topics in surface physics include surface reconstruction, surface phonons and plasmons, epitaxy on surface, the emission and tunneling of electrons, spintronics, and the self-assembly of nanostructures on surfaces.

Surface science needs special research methods and techniques. Much care and inspiration has been devoted to exploring the systematic laws governing surface processes. Physicist Wolfgang Pauli once remarked on the surfaces in the following way, "God made solids, but surfaces were the work of the devil!" It is this "devil" quality of surfaces that imposes challenges to the surface scientists and stimulates our curiosity. But excitingly, much progress has been made; details can be found in excellent books [9, 7, 3, 10, 11, 12]. Fantastically, numerous advances have taken place in the last couple of decades with the development of nanotechnology. Furthermore, the significance of surface science study extends far beyond its own field, as quoted from Surface Scientist E. Ward Plummer, "Surfaces are the playground of Solid State Physics [13, 14]."

The multiple motivations for surface science study come from its significant scientific and practical importance. Surface-related phenomena, such as erosion, friction and surface tension, are everywhere in our daily life. Chemical reactions start at the solid surface and catalysts play an important role at the surfaces. To explain and understand such interesting behaviors is one mission of surface scientists. To engineer surfaces and put them into practical applications is a parallel pursuit. For instance, thin film growth on a surface or interface is crucially correlated to the quality of that surface or interface itself. This is particularly important in the modern semiconductor industry. Surface scientists

and engineers make many efforts to discover growth mechanisms of thin films and thus better control their growth. Recently, with the burgeoning development of nanotechnology, the importance of surfaces has been rising due to the increasing quantum effects resulting from the decreasing size. The high surface-to-volume ratio leads to many new properties of materials at the nanometer scale.

Specific goals in the surface investigations include probing the surface geometric structure, chemical composition and electronic structure. A wide variety of surface analysis techniques are well developed and the facilities are commercially available. Different surface techniques are used to extract different surface information and each has its own advantages and disadvantages. They can be classified in terms of probe type, resolution, operating environment, or working mode. Special expertises might be needed for individual techniques. The ultra-high vacuum (UHV) technique for the sample cleanness is an example.

Here is a partial list of techniques routinely used in many surface science laboratories: surface X-ray diffraction (XRD), X-ray photoelectron spectroscopy (XPS), ultra-violet photoelectron spectroscopy (UPS), Auger electron spectroscopy (AES), low-energy electron diffraction/microscopy (LEED/LEEM), electron energy loss spectroscopy (EELS), resolved high-energy electron diffraction (RHEED), electron/photon stimulated desorption (ESD/PSD), ion scattering spectroscopy (ISS), secondary ion mass spectrometry (SIMS), scanning tunneling microscopy/spectroscopy (STM/STS), atomic force microscopy (AFM), infrared reflection-absorption spectroscopy (IRAS), and surface enhanced Raman spectroscopies (SERS). Books describing these analytical techniques are suggested [7, 3, 9, 10, 11, 12, 15].

1.2 Thesis motivation

Determining structure and chemical composition of crystalline surfaces with high spatial resolution is the primary objective of this thesis. The surface region or the top layers ($\sim$10 Å in depth) tends to have structure different from its corresponding bulk due to the broken symmetry in the surface-normal direction. The atomic geometry and chemical composition are the most fundamental physical properties of surfaces. They are closely associated with other surface characteristics such as optical, magnetic, electronic and chemical properties. Surface structural information is essential to explain and predict material properties.

Unfortunately, 2D surface crystallography has been challenging compared to successful 3D crystallography which benefits from the X-ray diffraction (XRD) technique. The most powerful 2D crystallography tool, low energy electron diffraction (LEED), emerged only in the late 1960s thanks to the availability of ultra-high vacuum (UHV) and surface cleaning techniques although the working principle had been experimentally demonstrated in the 1920s [16]. Up to date, dynamical LEED analysis remains the most effective technique for surface crystallography. Its high sensitivity to atomic location and species, resulting from the atomic ion-core potential scattering, can be used to resolve the periodic structure of surfaces. The large scattering area (on the order of μm^2) over which the diffraction intensities are averaged, however, poses a restriction to our goal of measuring the surface structure and compositions at nanometer scale resolution in order to resolve heterogeneous structures.

Resorting to modern scanning probe microscopy/spectroscopy (SPM/SPS) turns out to be of little help. The reason is that these techniques have difficulties either in detecting the subsurface layers or in sensitively identifying the chemical elements. To overcome these hurdles, we are devoted to developing a new technique to realize our objective. The solution

4

is a combination of low-energy electron microscopy (LEEM) imaging and dynamical LEED-*IV* analysis techniques. LEEM is capable of *in situ* direct imaging of a surface, and the local surface information can be retrieved via the analysis of the local intensities in the image. In this thesis, I shall demonstrate that this technique, LEEM-*IV*, generates a 3D profile of the chemical composition of a PdCu surface alloy at 8.5 nm resolution, the first 3D mapping of surfaces at such a high resolution. Using this technique we have identified an ultra-thin film over-growth mechanism.

Furthermore, I have improved different LEED program packages to increase their versatility. The atomic structures of surfaces (111), (110) and (100) of the semimetal Bi are resolved. The surface geometries for single domains of the semiconductor surfaces, Si(001) and 6H-SiC(0001), are determined with LEEM. Monte Carlo simulations are employed to understand the energetics of the Pd/Cu(001) surface alloy system.

1.3   Content arrangement

Following this Introduction, in Chapter 2 and Chapter 3 I describe the experimental techniques of LEED and LEEM, respectively. In Chapter 4 I give an account of the Monte Carlo simulations. Results and discussions for bismuth surfaces (111), (110) and (001), the PdCu surface alloy on Cu(001) surface, the Si(001)-2×1 surface, and the 6H-SiC(0001) surface phases are presented in Chapter 5, 6, Appendix A, and B, respectively. In Chapter 7 I summarize the main results of this thesis and draw conclusions.

CHAPTER 2

Low Energy Electron Diffraction

2.1 LEED physics

2.1.1 Surface structure

The creation of a new surface by cleaving a crystal brings structural changes to the exposed surface plane. The changes could lead to dramatic differences in the physical and chemical properties between the surface and the underlying bulk. Therefore, the surface structure is of fundamental significance in surface science.

For a perfect bulk-terminated surface, the atomic structure retains the same lateral symmetry as the bulk but has a broken symmetry in the surface normal direction. Many surfaces even have more radical structural changes due to the creation of the surface-vacuum interface. The surface chemical species could be foreign atoms adsorbed on the substrate. At the uppermost several layers, atomic rearrangements are possible. Figure 2-1 illustrates some rearrangements of the surface atoms, including interlayer relaxations, atomic reconstructions, and a missing row structure. It is not surprising that these geometric reorganizations can result in a dramatic change in physical and chemical properties. A surface lattice structure of foreign atom B on the substrate $A(hkl)$ is usually denoted by $A(hkl)$-$(m \times n)$-$R\theta°$-B, where m and n are the length ratios of two overlayer unit cell vectors to two substrate unit cell vectors and $\theta°$ represents the angle between the substrate unit cell vectors and the

6

→| a |←	→| 2a |←	→| 2a |←
(a) Relaxation	(b) Reconstruction	(c) Missing row reconstruction
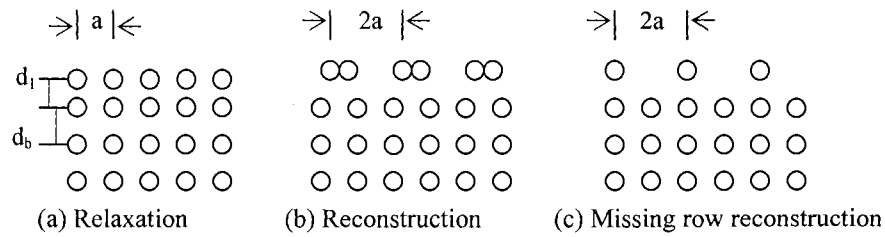
Figure 2-1: The side view of surface atom rearrangements in a simple cubic lattice with the lattice constant a. (a) The atomic layer spacing is contracted with $d_1 < d_b$, where d_1 and d_b are the first interlayer and bulk interlayer spacings, respectively. (b) A dimerization causes a new surface lattice vector length of 2a. (c) A missing row reconstruction also leads to a new surface lattice vector length of 2a.

overlayer unit cell vectors. $R\theta°$ can be omitted when $\theta = 0$. B can be omitted when B atom is A atom itself.

Another aspect of real surfaces is the existence of defects. Zero-dimensional or point defects involve adatoms, ledge adatoms, kinks, and vacancies. An important one-dimensional or line defect is the step in which the atomic ledge separates two terraces from each other. Figure 2-2 depicts a typical surface topology which shows terraces, adatoms, vacancies, steps, and kinks. Steps are important in the formation of high-index surfaces. Because of defect-induced local variation in important physical quantities, such as binding energy, coordination and electronic states, the defect structure of a surface plays a predominant role in surface processes such as crystal growth, evaporation, surface diffusion, adsorption, and surface chemical reactions.

The four systems studied in this thesis have different surface structures. The Bi(111), (110) and (001) surfaces all retain the truncated bulk surface lattice structures. The Pd ultra thin film on the Cu(001) substrate has a $c(2\times2)$ underlayer intermixing structure.

1. Terrace
2. Adatom
3. Terrace vacancy
4. Monatomic ledge
5. Kink
6. Ledge-adatom
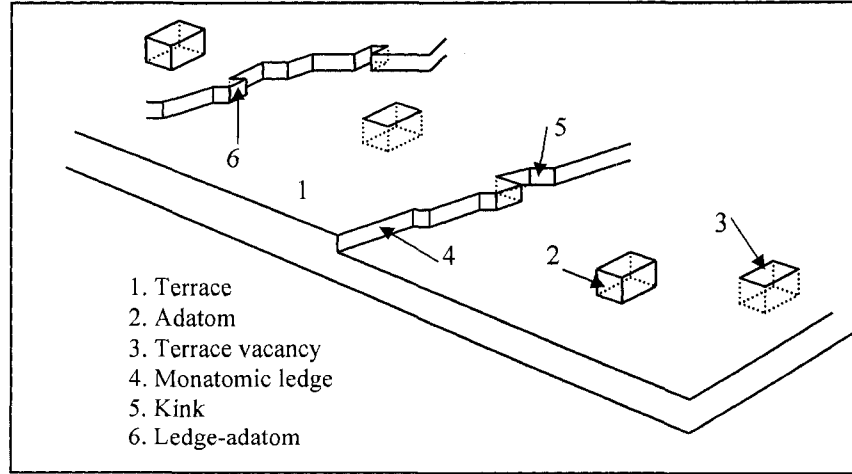
Figure 2-2: A schematic view of a typical surface topology. Surface structures/defects include terraces, adatoms, vacancies, kinks and steps.

The Si(001) surface reconstructs into a 2×1 dimer superlattice. The 6H-SiC(0001) surface exhibits rich surface phases at different temperatures; they include 1×1, 3×3, $\sqrt{3}\times\sqrt{3}$-$R30°$ and $6\sqrt{3}\times6\sqrt{3}$ structures.

For a 2-dimensional (2D) periodic atom net, only five ways exist to arrange the lattice points, and the resulting lattices are the five Bravais lattices shown in Figure 2-3. They are the oblique, primitive rectangular, centered rectangular, square, and hexagonal lattices. The corresponding reciprocal lattices can be obtained by defining base vectors $(\vec{b}_1, \vec{b}_2)$ in reciprocal space in terms of base vectors $(\vec{a}_1, \vec{a}_2)$ in direct space as

$$\vec{a}_i \cdot \vec{b}_j = 2\pi\delta_{ij} \ (i, j = 1, 2).$$
(2.1)

A 2D reciprocal lattice possesses the same symmetry as its corresponding real space lattice. This characteristic can be used to infer the real lattice structure from the lattice diffraction pattern. Details will be described later in this chapter.
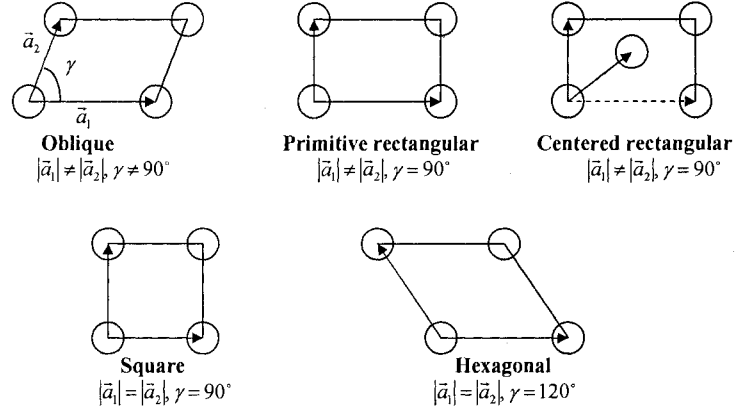
Figure 2-3: Unit cells of five 2D Bravais lattices. $\vec{a}_1$ and $\vec{a}_2$ are surface lattice vectors. γ is the angle between these two lattice vectors.

2.1.2 Electron diffraction

Among the surface probes of photons, electrons, ions and atoms, electrons are uniquely suitable to resolve the atomic surface structure. The short electron mean-free-path (eMFP) at low energy makes electrons particularly sensitive to the surface region. Figure 2-4 gives plots of the universal eMFP against electron kinetic energy in many solids. One can see that the eMFP is between 5 and 10 Å for an electron energy range of 20 to 500 eV. This eMFP is comparable to the thickness of about 3 to 5 atomic layers that we are interested in. Meanwhile, the wavelength of the electrons in this energy range is comparable to the interatomic spacing, which makes the diffraction possible.

In principle, low energy electron diffraction is analogous to X-ray diffraction which is used to determine bulk lattice structures. The kinematic theory of the diffraction is sufficient to explain the experimental diffraction principle. The Laue equation describes the diffraction condition:

$$\Delta \vec{K}^{\parallel} = \vec{K}_s^{\parallel} - \vec{K}_i^{\parallel} = \vec{g}_{hk},\qquad(2.2)$$

9

where $\vec{K}_i^{\parallel}$ and $\vec{K}_s^{\parallel}$ are the components of the incident and scattering wave vector $\vec{K}_i$ and $\vec{K}_s$ parallel to the surface. $\Delta\vec{K}^{\parallel}$ is the parallel component of momentum transfer and $\vec{g}_{hk}$ is a vector of the 2D surface reciprocal lattice point (hk). Moreover, the elastic diffraction requires $\left|\vec{K}_s\right| = \left|\vec{K}_i\right|$. We can apply an Ewald sphere to the 2D problem as long as we attribute each reciprocal 2D lattice point (hk) to a rod normal to the surface.

Figure 2-5 shows the Ewald sphere construction for elastic electron diffraction on a 2D surface lattice. The graph shows the reciprocal 2D lattice points (hk) which satisfy the diffraction Equation 2.2, given as the crossing points between the Ewald sphere and the array of parallel diffraction rods.

For surface structure determination by LEED, kinematic theory as used in X-ray diffraction is not enough. The incident electrons are scattered multiple times by the ion-core potentials before they leave the material. The scattering cross-section is very large, hence we can get intense diffracted beams. One key aspect that complicates the modeling of the scattering processes is the multiple scattering of electrons which requires a much more elaborate analysis. Fortunately, the back-reflected electrons are restricted to the first three to five atomic layers. This implies that the complications from multiple scattering are limited to the surface region. The next section will give a more detailed description of the dynamical scattering processes to be considered.

2.1.3 Dynamical processes

LEED scattering is a dynamical process. Four main ingredients of the electron-solid interaction are addressed individually as follows:

- ion-core potential scattering

    Like other probes such as ions, atoms and photons, impinging electrons interact with

10
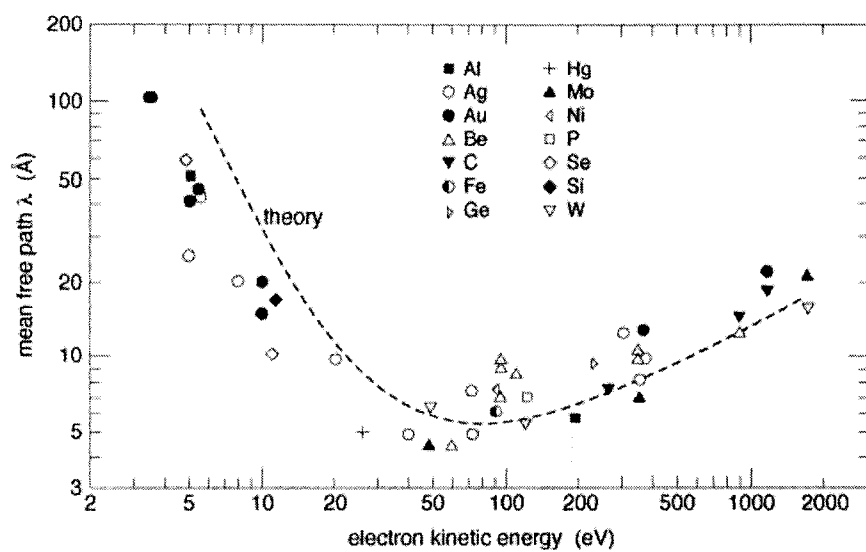
Figure 2-4: Measured (markers) and calculated (the dashed curve) mean-free-path of electrons in a solid. After Zangwill [3] and references therein.
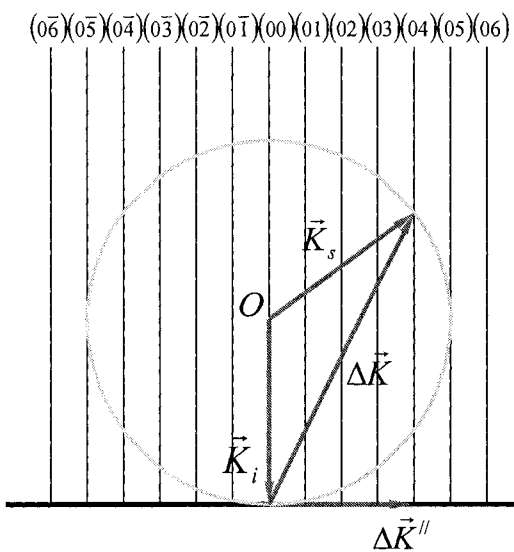
Figure 2-5: Ewald sphere construction for LEED. Indices of surface diffraction rods are given at the top.

a solid in a way that follows their own intrinsic nature. The chosen electron energy is low, ranging from 10 to 500 eV, and the electron carries a negative charge and a small mass. The electron will feel the Coulomb force in an atom from both the nuclei and the surrounding electrons. As the Coulomb potential decays rapidly far away from the nucleus, we can model the potential of the atomic lattice as a muffin-tin shape, i.e. a spherically symmetric potential within the muffin-tin radius of the atom and a constant potential V_0 in between the atoms. As a consequence, the electron-atom interaction is an electron interaction with ion-core potential. This model gives a simple spherical form of the scattering wave and facilitates the dynamical LEED analysis. One complication caused by the many-body interaction is simplified by the Slater approximation in the Hartree-Fock exchange-correlation term.

- inelastic effects

For the LEED pattern and LEED-IV spectrum, we consider only elastically-scattered electrons. Typically, intensities of elastically scattered electrons account to the order of 1% of the incident electrons. Many of the other electrons suffer inelastic collisions. On one hand, we experimentally exclude the inelastically scattered electrons by collecting only the elastically scattered electrons. On the other hand, we benefit from the strong inelastic processes. The inelastic effects cause the short mean-free-path of the electrons at the applied energies. The inelastic scattering could be caused by many different surface processes. Surface plasmon excitations, conduction electron excitations and core-level excitations are main sources. Surface state resonances and phonon excitations are also important in some cases. The electron attenuation by the inelastic scattering is normally simulated by an imaginary part of the self-energy which is also referred to as damping potential or optical potential V_{0i}. At low plasmon

energies around 20 eV, the pronounced energy loss leads to a small damping potential. Below the plasmon energy, single electrons can be excited from the conduction band producing a smaller damping potential. Just above the plasmon energy, the damping potential rises rapidly, and at higher energies the speed of the electron reduces absorption resulting in a slowly increasing damping potential [17]. The change of damping potential with the electron energy explains the inelastic scattering mean-free-path changing trend in Figure 2-4.

- thermal effects

  Thermal vibration is an intrinsic property of atoms. The scattering intensity damping due to thermal absorption is inevitable even at low temperatures. The higher the temperature the stronger the reduction of the beam intensity. In the dynamical analysis, the Debye-Waller factor, a concept borrowed from XRD, is used to model this effect. By optimizing the vibrational amplitude of the surface atoms, information on the surface Debye temperature can be obtained.

- multiple scattering

  Kinematic scattering theory, i.e. single scattering theory, is not sufficient to model low energy electron scattering. LEED is very different from XRD in this respect. LEED analysis requires more complicated multiple scattering calculations. Within kinematic theory, the peaks interpreted are called primary peaks; while in the LEED-*IV* spectra, additional peaks, or secondary peaks, show up and demand a dynamical interpretation. In the dynamical analysis, the multiple scattering is taken into account for both intraplane and interplane scattering.

2.2 LEED experiment

Figure 2-6 shows a schematic LEED setup and its optical system. An electron gun and the optical system produces a collimated beam of electrons which strike the sample surface. The backscattered electrons travel to a four-grid optical system which selects elastically scattered electrons and accelerates them onto a fluorescent screen. The visible pattern on the screen at a certain kinetic energy provides a picture of the reciprocal lattice points active in diffraction. When we ramp up the incident electron energy, the diffraction spots' positions and intensities change. By recording a series of diffraction patterns at different electron energies, we can extract the beam intensity vs ramp-voltage (IV) curves. The surface structural information will be obtained by comparing the calculated IV spectra with those obtained in the measurements.

We performed the Bi surfaces measurements on the LEED system of Prof. David Adams at the Institute for Storage Ring Facilities at the University of Aarhus in Denmark. A schematic setup of the LEED apparatus and the main parts of the system are shown in Figure 2-7. An effective set of vacuum pumps generates a base pressure of $7 \cdot 10^{-9}$ Pa in the main UHV chamber. A semi-spherical electron energy analyzer is employed to detect Auger electrons in order to monitor the surface cleanliness. An ion gun is used for sample sputtering. A fast low-temperature CCD camera (not shown in the picture) is mounted facing the LEED screen. The LEED pattern is recorded by the CCD camera and displayed on a computer monitor. By using kinematic theory, the calculated diffraction pattern is superimposed onto the observed pattern. The sample position can be aligned by finding the best overlap of these two patterns. In this way, the angles of incidence can be adjusted to be within $0.5°$. The detailed experimental conditions for each surface will be given in Chapter 5.
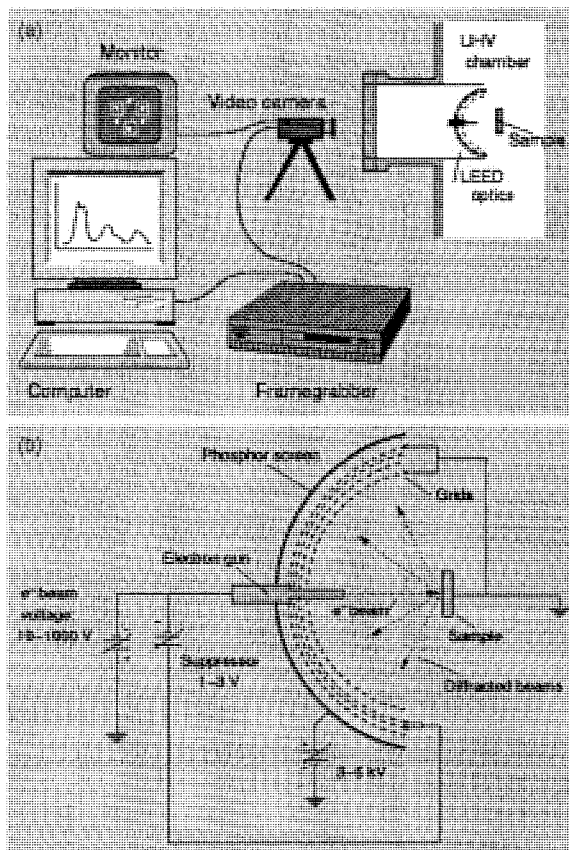
Figure 2-6: (a) A schematic LEED setup. (b) The LEED optical system.
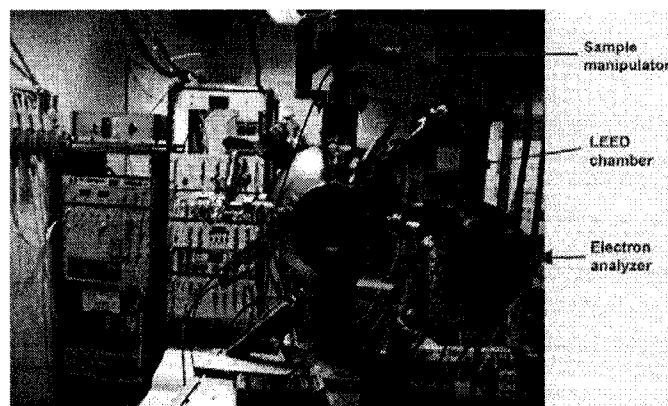
Figure 2-7: Aarhus LEED system for our work on Bi surfaces. The semi-spherical electron analyzer, the LEED main chamber and the sample manipulator are indicated.

2.3 Numerical implementation

Compared to many other surface techniques, LEED requires more complicated theoretical work. The reason is, as discussed in Section 2.1.3, the dynamical processes in low energy electron scattering. A full dynamical analysis is a must for a complete explanation of the spectrum structures. While being subject to many unknown structural or dynamical parameters, an appropriate and effective theory, either with an exact or approximate method, is needed. The efficiency of implementing a theory to computations is an extra consideration in order to reduce the computing time and efforts.

2.3.1 Calculation procedure

The excellent books by Pendry and Van Hove *et al.* [17, 18, 19] have detailed descriptions of LEED theories and their implementation in computing programs. The following is a brief introduction to the dynamical analysis scenario.

- phase shifts and atomic *t*-matrix calculations

Based on the simple plane-wave scattering by a spherically symmetric potential described in most quantum mechanics textbooks, the form of an asymptotic scattering wave can be expressed in terms of scattering amplitude $t(E, \theta)$:

$$e^{i\vec{k_0}\cdot\vec{r}} + t(E, \theta)\frac{ik_0 r}{r}, \tag{2.3}$$

where $\vec{k_0}$ is the wavevector of the incident plane wave, $\vec{r}$ is the distance vector from the atomic nucleus, θ is the polar angle, $k_0 = \left|\vec{k_0}\right|$, and $r = |\vec{r}|$. The scattering amplitude is then expanded in terms of *t*-matrix t_l and Legendre polynomials $P_l(cos\theta)$ as

$$t(E, \theta) = 4\pi \sum_{l=0}^{\infty} (2l + 1)t_l P_l(cos\theta), \tag{2.4}$$

$$\text{where} \qquad t_l = \frac{e^{2i\delta_l} - 1}{4ik_0} = \frac{e^{i\delta_l} sin\delta_l}{2k_0}. \tag{2.5}$$

16

Assuming that the radial wavefunction for the incident electrons with the angular momentum l is $\phi_l(r)$ and defining $L_l = \phi_l'(R)/\phi_l(R)$ where R is the muffin-tin radius, we obtain δ_l as the following formula by applying the continuity condition at the muffin-tin radius:

$$e^{2i\delta_l} = \frac{L_l h_l^{(2)}(\kappa R) - h_l^{(2)'}(\kappa R)}{h_l^{(1)'}(\kappa R) - L_l h_l^{(1)}(\kappa R)},\qquad (2.6)$$

where $\kappa = \sqrt{2(E - V_0)}$. $h_l^{(1)}$ and $h_2^{(1)}$ are spherical Hankel functions of the first and second kinds, respectively. E is the kinetic energy of incident electrons and V_0 the muffin-tin potential.

The radial wavefunction $\phi_l(r)$ is calculated from the radial Schrödinger equation below.

$$-\frac{\hbar^2}{2m}\left[\frac{1}{r}\right]\frac{d}{dr}\left[r^2\frac{d\phi_l(r)}{dr}\right] + \frac{\hbar^2 l(l+1)}{2mr^2}\phi_l(r) + [V_H(r) + V_{ex}(r) + V_0]\,\phi_l(r) = E\phi_l(r),\quad (2.7)$$

$$V_H(r) = -\frac{Ze^2}{r} + V_{sc}(r) + \sum_j \frac{\left|\psi_j(r')\right|^2}{|\vec{r} - \vec{r}'|}d^3\vec{r}',\qquad (2.8)$$

where Z is the nuclear charge at position $\vec{r}$ and $V_{sc}(r)$ is the potential due to the charge that screens the LEED electron (it is usually neglected). $\psi_j(r')$ is the wavefunction for the jth-core-electron. $V_{ex}(r)$ is the exchange-correlation term, a functional of charge density through the Slater's local potential approximation [20, 21, 22]. V_0 is the real part of inner potential.

The core-electron wavefunction is sufficiently tightly bound that they can be taken to be unchanged from those of the free atom. Calculations of free atom wavefunctions have been made by various authors [23, 24, 25] and are readily available. The accuracy of using such wavefunctions to construct ion-core potentials has been extensively checked through band structure calculations [26].

In Schrödinger equation 2.7, only the real part of the inner potential is included. The complex inner potential including both real part and imaginary part could have been incorporated. Then we would get complex phase shifts whose imaginary part implies that either

more or less flux is being absorbed inside the muffin-tin than would be absorbed by V_{0i} in the absence of the ion core, i.e. the scattering wave will be damped by $e^{-2Im\delta_l}$. Although this is a complete and proper way, in practice the inelastic effects are often not included in the phase shifts, but rather in the interatomic-wave propagation. The main reason is that as a consequence of this choice, the value of the imaginary part of the potential V_{0i} can remain unspecified until later and can thus be revised without having to recompute the phase shifts [19]. One justification to do so is that the choice of the treatment of V_{0i} is not critical because the correction to the phase shifts is small [17].

The atomic scattering phase shift is the only parameter in the LEED calculation to distinguish different chemical identification in substitutional alloys. So the difference in scattering properties for Pd and Cu is crucial for this binary system. We calculated the phase shifts and then the scattering amplitude $t(E, \theta)$ for both Cu and Pd atoms. The angular distribution of the scattering amplitude squared $|t(E, \theta)|^2$ is plotted in a polar coordinate system in Fig. 2-8. Three different electron kinetic energies are considered with respect to the vacuum zero. They are 2, 4 and 7 Rydbergs, respectively (1 Rydberg $\approx$ 13.605 eV). For both Cu and Pd, the amplitude squared ratio of forward scattering to the back scattering increases with increasing energies, which indicates prominent multiple scattering at lower energies and stronger electron damping at higher energies. By comparing the scattering strength for Cu and Pd, the scattering is much stronger by Pd than by Cu by noting the scale difference between the two panels in Fig 2-8. Based on the Equation 2.4, the total scattering cross section is obtained as

$$\sigma_T = \frac{4\pi}{k_0^2} \sum_l (2l + 1) sin^2(\delta_l), \tag{2.9}$$

where $k_0 = \sqrt{2(E + V_0)}$ because we have included the muffin-tin zero in the elastic scattering potential. The total scattering cross sections for Cu and Pd at the energy range

18

from 10 to 150 eV are calculated and drew in Fig. 2-9. We see that the total cross section is about $5a_0^2$ for Cu and $20a_0^2$ for Pd where a_0 (≈ 0.529 Å) is the Bohr radius. Their comparability in magnitude to the Cu(001) lattice unit cell size of $23.3a_0^2$ indicates strong electron scattering by atoms. The total cross section for Pd is apparently much stronger than Cu. This character follows the general trend that the scattering strength increases with increasing atomic number (29 for Cu and 46 for Pd). The difference in the scattering strength would account for our ability to distinguish Pd from Cu in the LEED scattering intensity calculations employed in our LEEM-*IV* technique.

- single layer scattering matrices

A layer with only one atom per unit cell is called a Bravais-lattice layer. The diffraction matrices for a Bravais layer between the incident wave $e^{i\vec{k}_{\vec{g}}^{\pm} \cdot \vec{r}}$ and $e^{i\vec{k}_{\vec{g}'}^{\pm} \cdot \vec{r}}$ are given by Pendry [27, 17]:

$$M_{\vec{g}'\vec{g}}^{\pm\pm} = \frac{8\pi^2 i}{A \left| \vec{k}_0 \right| k_{\vec{g}'\perp}^+} \sum_{\substack{l'm' \\ lm}} \left\{ i^l (-1)^m Y_{l-m} \left[\Omega(\vec{k}_{\vec{g}}^{\pm}) \right] \right\} (1-X)_{lm,l'm'}^{-1}$$

$$\times \left\{ i^{-l'} Y_{l'm'} \left[\Omega(\vec{k}_{\vec{g}'}^{\pm}) \right] \right\} e^{i\delta_{l'}} sin\delta_{l'} \quad (2.10)$$

In $M_{\vec{g}'\vec{g}}^{\pm\pm}$, the subscripts and superscripts read from right to left. The symbol "+" indicates the vacuum-to-surface direction and "−" the reverse direction. $\vec{g}$ and $\vec{g}'$ stand for two reciprocal lattice vectors. A is the area of the unit cell. $\vec{k}_0 = \sqrt{2(E - V_0)}$ and $\vec{k}_{\vec{g}} = \sqrt{2(E - V_0 - iV_{0i} - |\vec{g}|^2)}$. δ_l ($l=0$, 1, 2...) represent the set of phase shifts. $Y_{lm} \left[\Omega(\vec{k}_{\vec{g}}^{\pm}) \right]$ are the spherical harmonics where $\Omega(\vec{k}_{\vec{g}}^{\pm})$ is the solid angle of the beam.

The Eq. 2.10 has incorporated intralayer multiple scattering in a self-consistent fashion. It is implemented in the following way, and detailed mathematical deduction can be found in Ref. [27, 28] by Pendry. When the incident wave is expanded into spherical waves about the jth atom in a plane, the incident flux on the ion cores for each partial wave is denoted
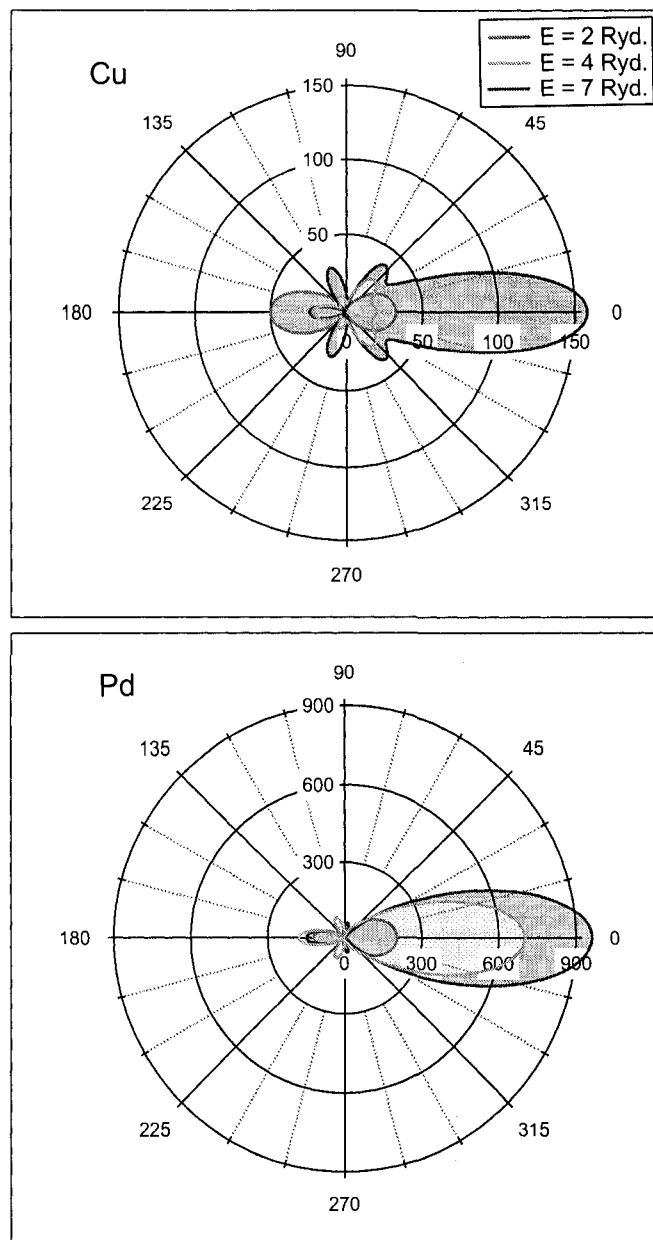
Figure 2-8: Polar plot of the atomic scattering amplitude squared $|t(E, \theta)|^2$ for Cu (upper panel) and Pd (lower panel) at three different electron kinetic energies 2 Ryd (red), 4 Ryd (green) and 7 Ryd (blue) (1 Ryd. $\approx$ 13.605 eV). Note the scale different between the two panels.

20
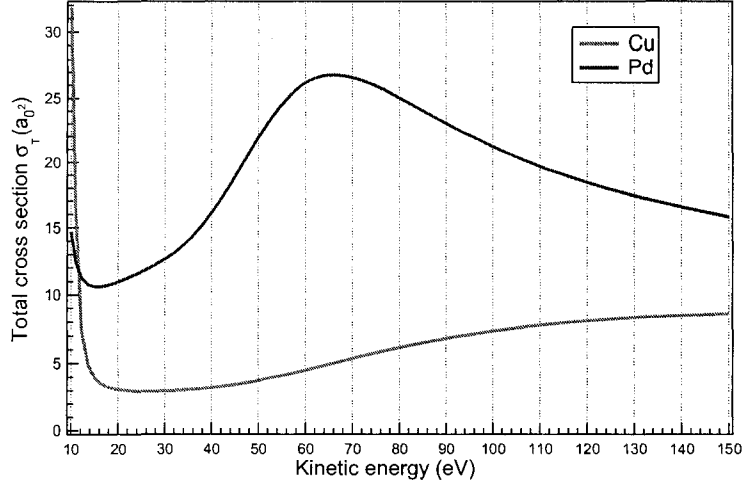
Figure 2-9: Total scattering cross sections for Cu (red curve) and Pd (blue curve) at the energy range of 10 to 150 eV with respect to the vacuum zero.

as $A_{lm}^{(0)}$. The scattering wave would be related to the flux via the phase shifts addressed in the preceding calculation procedure. To include the multiple scattering, the total flux must consist of two parts: the incident flux $A_{lm}^{(0)}$, and the scattered flux by other atoms $A_{lm}^{(s)}$. We hence get the total flux incident onto the jth atom:

$$A_{lm} = A_{lm}^{(0)} + A_{lm}^{(s)}, \tag{2.11}$$

where $A_{lm}^{(s)}$ itself depends on A_{lm} and therefore must be determined self-consistently. Provided that the A_{lm} are known, the incident flux on other atoms is obtained just by multiplying a phase factor from the jth atom to the other atoms. Then we get the flux incident on the jth atom scattered from other atoms. We expand this flux in the form of partial wave about the jth site and get

$$A_{lm}^{(s)} = \sum_{l'm'} A_{l'm'} X_{lm,l''m''}, \tag{2.12}$$

where X is the intralayer multiple diffraction matrix expressed in angular momentum space:

$$X_{lm,l''m''} = \sum_{l'+m'=even} C^l(l'm',l''m'')F_{l'm'}e^{i\delta_{l'}}sin\delta_{l'}. \qquad (2.13)$$

$C^l(l'm',l''m'')$ are the Clebsch-Gordon coefficients multiplied by some prefactors and $F_{l'm'}$ is the lattice sum in a plane. They are expressed as follows.

$$C^l(l'm',l''m'') = 4\pi(-1)^{(l-l'-l'')/2}(-1)^{m'+m''}Y_{l'-m'}(\frac{\pi}{2},0)$$
$$\times \int Y_{lm}(\Omega)Y_{l'm'}(\Omega)Y_{l''-m''}(\Omega)d\Omega \quad (2.14)$$

$$F_{l'm'} = \sum_j{}' e^{i\vec{k}_{0\parallel}\cdot\vec{R}_j}h_{l'}^{(1)}(k_0|\vec{R}_j|)(-1)^{m'}e^{-im'\phi(\vec{R}_j)} \qquad (2.15)$$

The sum in Equation 2.15 is taken over the layer's lattice vectors R_j excluding the origin atom. $\phi(\vec{R}_j)$ is the azimuthal angle of the vector R_j, and $k_0 = \sqrt{2(E-V_0-iV_{0i})}$.

Total flux A_{lm} would be given in terms of A_{lm}^0 and X by inserting Eq. 2.12 into Eq. 2.11 and finally the scattering matrices are obtained as Eq. 2.10.

When the beam symmetries and temperature effects are incorporated [18], we get

$$M_{\vec{g1}',\vec{g1}}^{\pm\pm} = \delta_{\vec{g1}',\vec{g1}}\delta_{\pm\pm}+$$
$$\frac{8\pi^2i}{A|\vec{k}_0||k_{\vec{g1}'\perp}^+|}\sum_{l'm'\atop lm}\left\{i^l(-1)^m\sqrt{\frac{J}{I}}\sum_{i=1}^I e^{i(\vec{g1}'-\vec{g_i})\cdot\vec{s}}e^{-i[m\phi(\vec{g_i})-m\phi(\vec{g1})]}Y_{l-m}\left[\Omega(\vec{k}_{\vec{g1}}^{\pm})\right]\right\}$$
$$(1-X)_{lm,l'm'}^{-1}\times\left\{i^{-l'}Y_{l'm'}\left[\Omega(\vec{k}_{\vec{g1}'}^{\pm})\right]\right\}e^{i\delta_{l'}(T)}sin\delta_{l'}(T),$$

where I and J both represent groups of plane waves related to each other by the same symmetry. In order to perform the symmetry reduction in the calculations, the origins of coordinates must be in the symmetry axis or plane. For multiple layers, the origins are not necessarily at the center of atoms in all layers. In this case, new origins in some layers must be referred to. Here $\vec{s}$ is the 2D vector relating the new origin of coordinates to the old one.

The thermal effect is represented by a temperature-dependent scattering amplitude which equals to a Debye-Waller factor e^{-M} multiplied by the scattering amplitude at 0

22

K, where

$$M = \frac{1}{6} \left| \Delta \vec{k} \right|^2 \langle (\Delta \vec{r})^2 \rangle_T . \tag{2.16}$$

The $\Delta \vec{k}$ is the momentum transfer and the $\Delta \vec{r}$ is the atomic vibrational vector. Since the temperature-dependent scattering amplitude can be expressed in terms of temperature-dependent phase shifts, we can instead include the thermal effect by replacing the phase shifts δ_l at 0 K with the temperature-dependent phase shifts $\delta_l(T)$. $\delta_l(T)$ can also be seen as effective phase shifts at temperature of T. By angular momentum expansion, the relation between $\delta_l(T)$ and δ_l is obtained as

$$e^{i\delta_l(T)} sin\delta_l(T) = \sum_{l'l''} i^{l'} e^{-4\alpha(E-V_0)} j_{l'} [-4i\alpha(E - V_0)]$$

$$\times e^{i\delta_{l''}} sin\delta_{l''} [\frac{4\pi(2l' + 1)(2l'' + 1)}{2l + 1}]^{1/2} B^{l''} (l'0, l0), \quad (2.17)$$

where

$$\alpha = \frac{1}{6} \langle (\Delta \vec{r})^2 \rangle_T \tag{2.18}$$

and

$$B^{l''} (l'0, l0) = \int Y_{l''m''}(\Omega) Y_{l'm'}(\Omega) Y_{l-m}(\Omega) d\Omega. \tag{2.19}$$

- composite layer scattering matrices by matrix inversion

A composite layer refers to a layer with more than one atom per unit cell. A matrix inversion formalism can be used to calculate the composite layer scattering matrices [28, 29]. Given a N-subplane layer, the following quantities are defined in a spherical wave representation with $L = (l, m)$.

$t_l^i = \frac{1}{2k_0} e^{i\delta_l} sin\delta_l$: scattering t-matrix of a single atom in subplane i;

$\tau_{LL'}^i$: scattering matrix containing all scattering paths within subplane i;

$T_{LL'}^i$: scattering matrix including all those scattering paths within the composite layer that terminates at subplane i;

$G_{LL'}^{ji}$: structural propagators describing all unscattered propagations from atoms in the subplane i to atoms in the subplane j.

$G_{LL'}^{ji}$ can be expressed either as a sum over lattice points in real space or as a sum over reciprocal-lattice points. Here we show the latter form:

$$G_{LL'}^{ji} = e^{-i\vec{k}_{\vec{g}}^{\pm} \cdot (\vec{r}_j - \vec{r}_i)} \hat{G}_{LL'}^{ji},$$ (2.20)

with

$$\hat{G}_{LL'}^{ji} = -\frac{16\pi^2 i}{A} \sum_{\vec{g_1}} \frac{e^{i\vec{k}_{\vec{g_1}}^{\pm}(\vec{r}_j - \vec{r}_i)}}{\vec{k}_{\vec{g_1},\perp}^{+}} Y_L^*(\vec{k}_{\vec{g_1}}^{\pm}) Y_{L'}(\vec{k}_{\vec{g_1}}^{\pm}).$$ (2.21)

The $\vec{r}_i$ and $\vec{r}_j$ are the positions of arbitrary reference atoms in subplanes i and j, respectively. The sum over $\vec{g_1}$ converges rapidly because $\vec{k}_{\vec{g_1}}^{\pm}$ has an increasing imaginary part as the magnitude of $\vec{g_1}$ becomes large.

The subplane τ-matrix is represented by the following expression (I is the unit matrix) [30]:

$$\tau_{LL'}^i = [(I - t^i G^{ii})^{-1}]_{LL'} t_l^i.$$ (2.22)

The matrices $T^i (i=1, ..., N)$ are obtained in the following way [28].

$$
\begin{pmatrix} T^1 \\ T^2 \\ \cdot \\ \cdot \\ \cdot \\ T^N \end{pmatrix}
=
\begin{pmatrix}
I & -\tau^1 G^{12} & ... & -\tau^1 G^{1N} \\
-\tau^2 G^{21} & I & ... & -\tau^2 G^{2N} \\
\cdot & \cdot & & \cdot \\
\cdot & \cdot & \cdot & \cdot \\
\cdot & \cdot & & \cdot \\
-\tau^N G^{N1} & -\tau^N G^{N2} & ... & I
\end{pmatrix}^{-1}
\begin{pmatrix} \tau^1 \\ \tau^2 \\ \cdot \\ \cdot \\ \cdot \\ \tau^N \end{pmatrix}
$$

Factoring out the following quantity $R_{\vec{g}}^{i\pm}$ from Equation 2.20,

$$R_{\vec{g}}^{i\pm} = e^{\pm i\vec{k}_{\vec{g}}^{\pm} \cdot \vec{r}_i}$$ (2.23)

we get the composite layer diffraction matrices

$$M_{\vec{g}'\vec{g}}^{\pm\pm} = -\frac{16\pi^2 i}{A} \sum_{LL'} \frac{Y_L(\vec{k}_{\vec{g}}^{\pm})Y_{L'}^*(\vec{k}_{\vec{g}}^{\pm})}{k_{\vec{g}\perp}^+} \sum_{i=1}^{N} \left[R_{\vec{g}}^{i\pm}(R_{\vec{g}}^{i\pm})^{-1}T_{LL'}^i \right].$$ (2.24)

- bulk reflection matrix calculation

Once the Bravais layer and composite layer matrices have been obtained by the above formalisms, one can stack these layers to get the bulk scattering matrices. The bulk reflection matrix can be calculated by the layer-doubling method or the renormalized forward scattering (RFS) perturbation method.

The layer-doubling method stacks two identical layers (or slabs) to get a new layer (slab) which will be the new stacking layer (or slab). This double layers stacking is repeated until reflected beams converge. For the two diffraction layers A and B, each having diffraction matrices r_A^{+-}, r_A^{-+}, t_A^{++}, t_A^{--} and r_B^{+-}, r_B^{-+}, t_B^{++}, t_B^{--}, respectively, the combined slab has diffraction matrices given by Pendry [17] shown below.

$$
\begin{aligned}
R^{-+} &= r_A^{-+} + t_A^{--}P^-r_B^{-+}P^+(I - r_A^{+-}P^-r_B^{-+}P^+)^{-1}t_A^{++} \\
T^{++} &= t_B^{++}P^+(I - r_A^{+-}P^-r_B^{-+}P^+)^{-1}t_A^{++} \\
R^{+-} &= r_B^{+-} + t_B^{++}P^+r_A^{+-}P^-(I - r_B^{-+}P^+r_A^{+-}P^-)^{-1}t_B^{--} \\
T^{--} &= t_A^{--}P^-(I - r_B^{-+}P^+r_A^{+-}P^-)^{-1}t_B^{--}
\end{aligned}
$$ (2.25)

The P^+, P^- are propagating matrices from a reference point in the layer A to a reference point in the layer B. If $\vec{r}_{BA}$ is the vector of these two points from layer A and B, we have

$$P_{\vec{g}}^{\pm} = e^{\pm i\vec{k}_{\vec{g}}^{\pm}\cdot\vec{r}_{BA}}.$$ (2.26)

The RFS method [31] assumes that the reflection by all layers is weak and the perturbation is therefore based on an expansion of the total reflectivity of the surface in terms of the number of reflections. The 1st order perturbation contains all the paths that have been reflected only once, the 2nd order contains only triple-reflection paths, and so on. The RFS

25

scheme typically uses less than 20 layers and less than 6 orders of iteration for convergence. See more details in literature [18, 31].

It should be noted that these two stacking methods have their own limits. The layer-doubling method has good convergence only when the interlayer spacing is larger than ~0.5 Å. The RFS method must have the interlayer spacing larger than ~0.9 Å. In other cases, one must employ the composite layer method to calculate the closely spaced layers.

2.3.2 Reliability factor

Once the experimental *IV* curves are obtained, we compare them with simulated ones for trial structures. A reliability factor R is chosen to measure the level of agreement. By optimizing some structural and other non-structural parameters, the best-fit structure is regarded as the real surface structure.

The two most widely used R factors are the R_p (Pendry R factor) [32] and the R_2 factor [33, 34, 35]. R_p is particularly sensitive to the relative peak position and the existence of small peaks but less sensitive to relative heights and relative peak width. The R_p is defined in the following way. The logarithmic derivative L of the diffraction intensity is given first by

$$L = \frac{dln(I(E))}{dE} = \frac{1}{I(E)}\frac{dI(E)}{dE}.$$ (2.27)

A function Y is then introduced

$$Y = \frac{L}{1 + V_{0i}^2 L^2},$$ (2.28)

where V_{0i} is the imaginary part of the inner potential.

The R_p factor is defined as

$$R_p = \frac{\int (Y_{exp} - Y_{cal})^2 dE}{\int (Y_{exp}^2 + Y_{cal}^2)dE}$$ (2.29)

The R_p factor is a simple quadratic function of the discrepancy and so is easily analyzed statistically. We assume that, due to random fluctuations, the residual value of R_P at the minimum value $R_{P\,\mathrm{min}}$ is

$$\Delta R_P = R_{P\,\mathrm{min}} \times \sqrt{\frac{8|V_{0i}|}{\Delta E}}, \tag{2.30}$$

where ΔE is the total energy range compared in the IV analysis. From this number and the curvature in R_P near the minimum, we can estimate errors in optimized parameters.

In contrast, the R_2 factor compares the IV curve intensities point by point, quite similar to the χ^2 used in X-ray diffraction. It takes into account the absolute magnitude of the intensity. From beam to beam, the same scaling factor is used. The R_2 factor is defined as:

$$R = \sum_{hk,i} \left(\frac{I_{hk,i}^{ex} - cI_{hk,i}^{cal}}{\sigma_{hk}}\right)^2 \Big/ \sum_{hk,i} \left(\frac{I_{hk,i}^{ex}}{\sigma_{hk}}\right)^2, \tag{2.31}$$

where $I_{hk,i}^{ex}$, $I_{hk,i}^{cal}$ are the experimental and calculated intensities, respectively. The index i represents the data points spanning over the electron energy range. The experimental uncertainty of the beam (hk), σ_{hk}, is obtained by comparing symmetry-equivalent beams [35]. The global scaling constant c can be determined by $\partial R / \partial c = 0$:

$$c = \sum_{hk,i} \left(\frac{I_{hk,i}^{ex} I_{hk,i}^{cal}}{\sigma_{hk}^2}\right) \Big/ \sum_{hk,i} \left(\frac{I_{hk,i}^{cal}}{\sigma_{hk}}\right)^2. \tag{2.32}$$

Estimates of the parameter uncertainties σ_i have been taken to be

$$\sigma_i = \left(\frac{R_{min}\epsilon_{ii}}{N_{free} - n}\right)^{1/2}. \tag{2.33}$$

were n is the number of parameters and R_{min} is the local minimum value. The error matrix ϵ can be obtained from the curvature matrix α via $\epsilon = \alpha^{-1}$, where [36]

$$\alpha_{ij} = \frac{1}{2}\left(\frac{\partial^2 R}{\partial x_i \partial x_j}\right) \simeq \sum_{hk,i} \left(\frac{\partial I_{hk,i}^{cal}}{\partial x_i}\right)\left(\frac{\partial I_{hk,i}^{cal}}{\partial x_j}\right). \tag{2.34}$$

N_{free} is taken to be

$$N_{free} = \sum_{hk} \frac{\Delta k_{\perp,hk}(E_2) - \Delta k_{\perp,hk}(E_1)}{2\pi/d}, \tag{2.35}$$

where $\Delta k_{\perp,hk}(E)$ is the surface-normal component of the diffraction vector for the beam (hk) at energy E. $[E_1, E_2]$ is the energy interval for each measured beam (hk), and d is the bulk interlayer spacing.

2.3.3 Program packages

We use several different packages for different surface systems. One package is a fully automatic procedure for structure search by Adams [37]. This dynamical LEED procedure is based on the computer programs [38, 39] developed from the programs of Pendry [17] and of Van Hove and Tong [18]. The layer-doubling method is used for bulk matrix calculation. In order to realize simultaneous optimization of all structural and nonstructural parameters, a new procedure has been constructed for the R factor minimization. For details of this procedure and the quadratic tensor model (QTM) algorithm, see Ref. [37] and Ref. [40], respectively. Other striking advantages of this package include its high computing efficiency by dynamically allocating matrix sizes with Fortran 90 codes and the friendly interactive environment by implementing a graphical user interface (GUI) to control the LEED program. Figure 2-10 shows the flow chart of the program. We adapt this package to the Bi(111) surface by allowing for the composite layer matrices input for bulk matrices calculation. This package is also used for the Pd/Cu(001) system by implementing an energy-dependent inner potential. The second package is the standard package SATLEED (Symmetrized Automated Tensor LEED) by Barbieri and Van Hove [41] within the renormalized forward scattering perturbation formalism. This package has been used to resolve the Bi(110) surface structures. It is also used to check the results by other packages.

The third one is the non-symmetrized automated tensor LEED programs for multiple angles of incidence and/or surface structures (ATLMLEED) [41]. It is suitable for calcu-

```
┌─────────────────────────────────────────────────────────────┐
│ Write parameter values of trial structures into input data files │
└─────────────────────────────────────────────────────────────┘
                              │
     ┌───────────────────────▼───────────────────────────┐
  ┌─►│     Calculate scattering matrices of bulk layers    │
  │  └────────────────────────┬───────────────────────────┘
  │  ┌────────────────────────▼───────────────────────────┐
  │  │    Calculate total bulk matrices by layer doubling   │
  │  └────────────────────────┬───────────────────────────┘
  │  ┌────────────────────────▼───────────────────────────┐
  │  │   Calculate scattering matrices of surface layers    │
  │  └────────────────────────┬───────────────────────────┘
  │  ┌────────────────────────▼───────────────────────────┐
  │  │  Calculate intensity vs. energy curves by combining  │
  │  │     scattering matrices of bulk and surface layers   │
  │  └────────────────────────┬───────────────────────────┘
  │  ┌────────────────────────▼───────────────────────────┐
  │  │     Calculate model functions or derivatives of model│
  │  │          functions and the R-factor                  │
  │  └────────────────────────┬───────────────────────────┘
  │  ┌────────────────────────▼───────────────────────────┐
  │  │     Read model function values into QTM algorithm    │
  │  └────────────────────────┬───────────────────────────┘
  │  ┌────────────────────────▼───────────────────────────┐
  │  │   Obtain new values of parameters by QTM algorithm   │
  │  └────────────────────────┬───────────────────────────┘
  │  ┌────────────────────────▼───────────────────────────┐
  │  │   Has convergence been reached by QTM algorithm?     ├──┐
  │  └────────────────────────┬───────────────────────────┘  │
  │                        Yes│                           No  │
  │             ┌─────────────▼───────────┐                   │
  │             │  Optimization finished.  │                  │
  │             └─────────────────────────┘                   │
  │  ┌──────────────────────────────────────────────────┐    │
  └──┤   Write new values of parameters into input data files │◄──┘
     └──────────────────────────────────────────────────┘
```

Figure 2-10: Flow chart describing the LEED calculation and optimization process. QTM stands for the quadratic tensor model algorithm.

lations of several different coexisting structures (multiple domains). We use this one for the Bi(001) and Bi(110) surfaces. Both SATLEED and ATLMLEED use the Tensor LEED method for a quick structure search [42].

Atomic scattering phase shifts have been calculated using a muffin-tin potential model and the standard Barbieri/Van Hove phase shift package available online [41]. The phase shifts have been renormalized by the thermal effects of rms isotropic vibrational amplitudes.

2.4 LEED technique development

LEED remains the most powerful tool for 2D atomic structure determination due to the unique information it acquires. The diffraction pattern is just a Fourier transform of the real space and hence retains the symmetry of the real space. According to this relationship, we can infer the surface lattice structure from a diffraction pattern. However, this simple analysis can not determine the atomic positions within the unit cell. The quantitatively dynamical analysis of the diffraction intensities can solve this problem. The dynamical analysis can be done by following the steps described in 2.3.1. Multiple scattering is incorporated for the intralayer and interlayer scatterings. Inelastic scattering and thermal effects are considered. The energy dependent diffraction intensity is very sensitive to the structural parameters. In the surface-normal direction, the order of magnitude of 0.01 Å can be accurately obtained.

So far, the LEED technique has successfully resolved numerous surface structures. They include simple metal surfaces, surface alloys, and metal oxide compounds and other adsorbates on surfaces. A super cell as big as (7×7) on the Si(111) surface has been resolved [43]. Recently, complex transition metal oxide surface structures have been determined [44] and the application to nanostructure diffraction has been tried [45]. A Fortran-90 LEED program has been developed to handle non-diagonal t-matrices describing the scattering of non-spherical potentials, anisotropic vibrations, and anharmonicity [46]. There is still much potential to further develop the technique. Diffuse LEED, direct LEED holography, and spin polarized LEED (SP-LEED) have been developed and they are under improvement. Diffuse LEED works for disordered surface structures. Direct LEED holography gives a fast and highly efficient determination of atom locations. SP-LEED can be used to characterize magnetic materials. Much more work can be invested in these promising techniques. In

this thesis, I shall describe the development of a LEEM-*IV* technique in chapter 6 which

has resolved the 3D surface region structure and chemical composition.

CHAPTER 3

Low Energy Electron Microscopy

3.1 Introduction

LEEM (low energy electron microscopy) is a relatively new modern surface analytical technique. It was invented by Bauer in 1962 on glass-based vacuum apparatuses [47]. The first operational LEEM instrument was constructed under UHV conditions by Telieps and Bauer in 1985 [48, 49]. In the IBM T. J. Watson Research Center, the LEEM-I system was developed by Tromp and Reuter in 1991 [50], and the LEEM-II system by Tromp *et. al* in 1998 [4, 51]. Commercialized LEEM facilities are available from only two manufacturers: ELMITEC GmbH since 1995 and SPECS GmbH since 2007. At present, there are about 30 LEEM facilities in operation throughout the world [52].

LEEM possesses the combined functions of electron diffraction and real-time *in-situ* direct imaging techniques. The high lateral spatial resolution and high temporal resolution makes it a powerful unique tool in surface studies. For instance, the IBM LEEM-II system reaches a high spatial resolution up to 5 nm. As a result, LEEM is particularly suited for studying surface dynamical processes at nanometer scale such as surface phase transition, surface adsorption, thin film growth, and surface reaction. In an early review, Bauer presented a detailed description of studies by LEEM [53].

Although the diffraction principle in LEEM is the same as in LEED, an aperture, in

LEEM, can be placed in the back-focal plane of the objective lens allowing only one beam to go through. Consequently, electrons in this beam, reflected from an illuminated surface area, will be projected onto the imaging plane forming a spatially-resolved intensity image. By recording and analyzing the contrast variation in the image, structural and compositional information could be extracted. With respect to its capability of 3D surface structural and compositional determination, the LEEM technique plays an irreplaceable role in surface analytical techniques.

3.2 LEEM equipment setup

LEEM may be better understood by comparison with transmission electron microscopy (TEM). Although both use electron probes and electron diffraction, their essential difference is the path of diffracted electrons. In TEM, the electrons go through thin samples while, in LEEM, the imaging electrons are backscattered. This difference makes the LEEM apparatus design more complicated and difficult. As a solution, a magnetic deflection prism was devised to direct the diffracted electrons. Another difference between LEEM and TEM is the energy range of incident electrons. TEM uses electrons with high energy up to tens of keV, while LEEM uses electrons with energy from 0 to 100 eV. This clearly leads to different electron penetration depths, which explains why the LEEM is suitable to detect the surfaces while TEM is used to detect the bulk. The following shows the setup of two LEEM systems, ELMITEC III and IBM LEEM-II, respectively.

The ELMITEC III system is shown in Figure 3-1 (a). The main components are an electron illumination column, a sample diffraction column, an imaging column, and a magnetic beam splitter. The magnetic sample loadlock provides easy load of a sample from air to the preparation chamber, and transfer of the sample between the preparation chamber and the

electron diffraction chamber. A detailed layout for each column is depicted in Figure 3-1 (b). The illuminating column is composed of an electron gun, a condenser, two deflectors, and a gun stigmator. The sample diffraction column contains an objective lens and an objective stigmator. The imaging column consists of a projector deflector, a contrast aperture, a transfer lens, two projectors, and a screen. The digital image is sent to a computer for information processing. All the electronic optics parameters are computer-controlled. In the crossing of three columns is the deflection prism which is also called a beam splitter shown in Figure 3-1 (b). We can see an angle of 120° between any two columns. This means the electron beam is deflected to the sample surface by 120°, and the backscattered beams are deflected as well, by 120°, to the imaging column. As will be seen in the following, the deflection angle difference is the primary difference between the ELMITEC III and IBM LEEM-II systems.

The IBM LEEM-II system is shown in Figure 3-2. The main components include an electron gun, three condenser lenses, a 90° deflection double-focusing prism array, a rotation-free objective lens doublet, and five lenses in the projector column (a transfer lens, a diffraction lens, and three projector lenses). In addition, there are two sets of stigmators in the condenser lens system, as well as three sets of steering coils. The objective lens contains a set of stigmators, and the projector column contains a set of steering coils. It is evident that the deflection angle of this system is 90° while that of ELMITEC III is 120°. Detailed descriptions of the design by Tromp *et al.* can be found in Ref. [4, 51].

3.3   LEEM working modes

Figure 3-2 (a) shows the electronic optics when a bright-field image is formed in the IBM LEEM II system. The emitted electrons from the electron gun are accelerated to 15 keV,
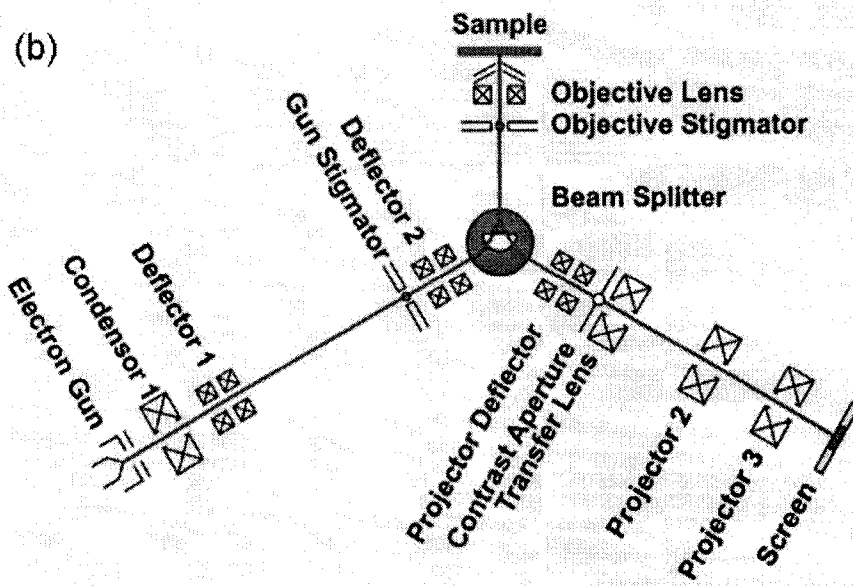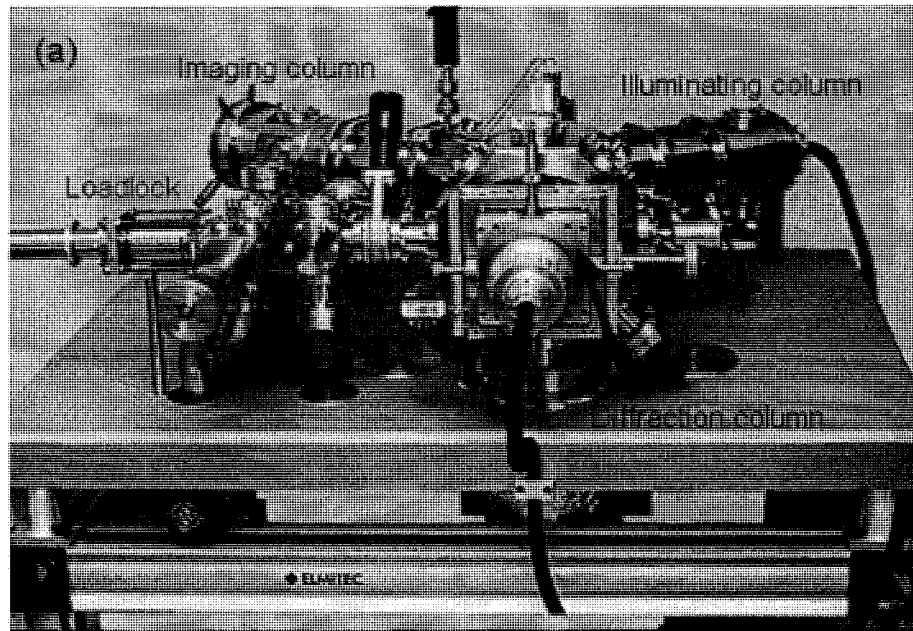
Figure 3-1: A schematic of the ELMITEC III LEEM system. (a) The main components include an electron illumination column, a sample diffraction column, an imaging column, and a beam splitter at the crossing of the above three columns. (b) Detailed components in each column.

15 keV
electron gun

condensor
lenses

magnetic
deflector
(prism array)

objective
lens

sample

-15 kV

aperture

projector
lenses

viewing screen

(a)

sample

objective lens

backfocal plane (bfp)

image plane

(b)
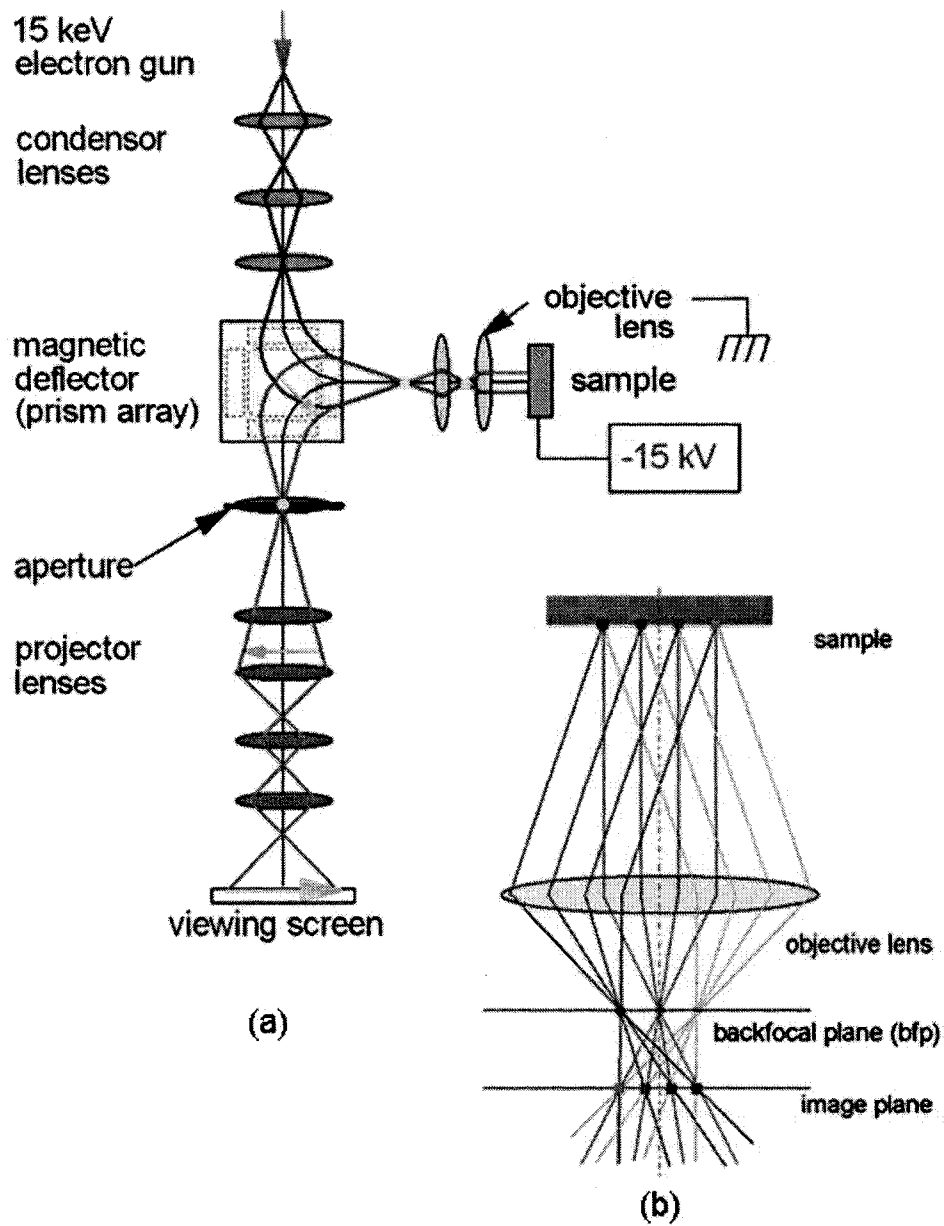
Figure 3-2: IBM LEEM II system by Tromp *et al.* [4]. (a) The LEEM optical system in the bright-field imaging mode. (b) A detailed schematic of the combined diffraction with an objective lens.

go through the condensor lenses and are deflected by the magnetic prism array by 90° to the objective lens. A bias of - 15 kV bettwen the sample and the objective lens decelerates the electron to be 0 to 200 eV. Then the slow electrons are reflected after diffraction at the crystalline surface. Reflected electrons are accelerated and focused by the objective lens. Once more they are deflected by 90° by the magnetic prism array downward to the aperture plane. The aperture allow only (00) beam to go through, and therefore the electrons in the (00) beam contribute to the image formed in the screen after passing the projector lenses. The image reflects the electron reflectivity of the illuminated surface area. By analyzing the contrast variation at different places in the image, information about the surface heterogeneity can be obtained. Figure 3-2 (b) depicts in more detail how the electron diffraction work with the objective lens. Three sets of parallel paths indicate three different diffracted beams from a large surface area. Each set of parallel beams are focused onto the back-focal plane by an objective lens. An aperture can be put on the back-focal plane to allow only one beam to transfer, resulting in an image projected onto the screen.

Besides the frequently used bright-field imaging, LEEM is a multifunctional device used for many different scientific purposes. The facility has always been equipped with a photo-electron emission microscopy. Figure 3-3 shows a chart of its working modes. The switching between different modes can be realized with easy and quick operations, as briefly described below [54].

- Reflectivity contrast

  Since different areas on the surface might show a difference in electron reflectivity, which dependes on the surface material or even the surface structure, and the reflectivity coefficient depends on the incident electron energy, the contrast can be optimized. The most famous example is the difference between the (7 × 7) reconstruction and
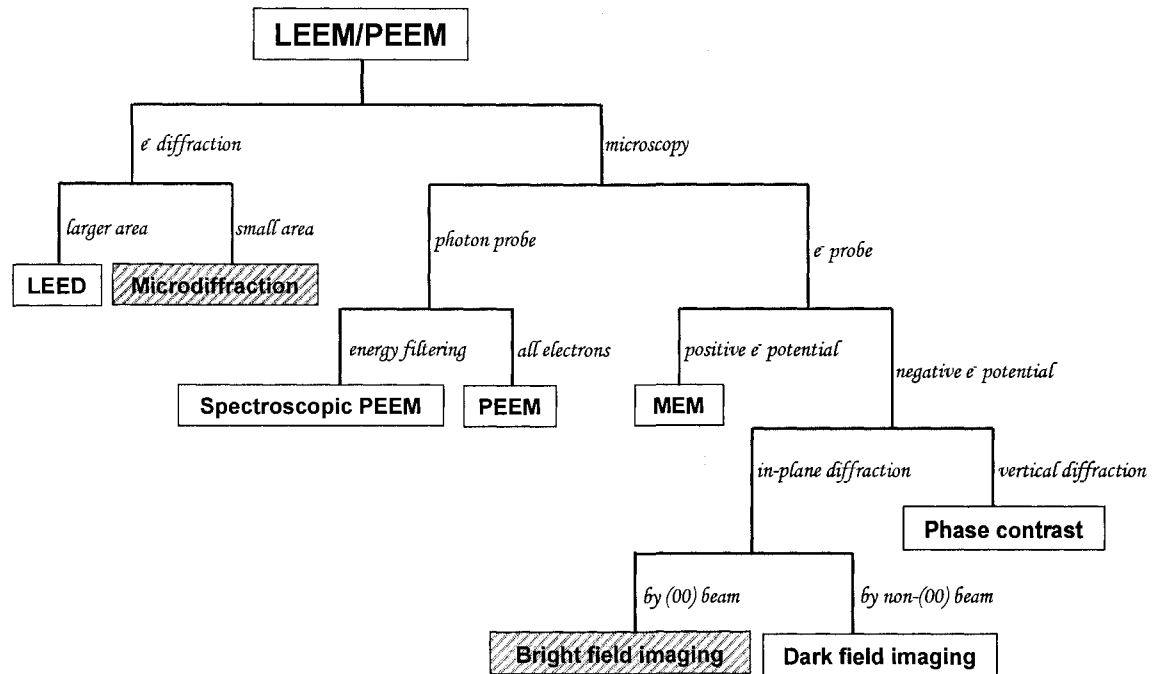
Figure 3-3: LEEM/PEEM working modes.

the (1×1) structure on the Si(111) surface at about 850°C. At an electron energy of about 10 eV the (7×7) areas appear much brighter than the remaining surface.

- Dark-field imaging

  One non-specular LEED spot is used in the intermediate plane for imaging. All areas on the surface that contribute to the existence of this spot appear bright in the image, and all other areas appear dark.

- Phase contrast

  The wave nature of the incident electron beam is used to generate a vertical diffraction contrast. The different topologies on the surface lead to different phase shifts of the electron wave and thus result in brightness contrast in the imaging. One example is that steps are made visible on the surface.

- MEM (mirror Electron Microscopy)

  The electron energy is reduced to the limit, when the electrons return in the retarding field, before they hit the sample surface. The incident electron potential is normally between -5 and 0 eV. The basic mechanism is that all height variations on the sample surface, such as steps, grains etc., change the local properties of the retarding field and therefore have influence on the reflected electron beam. The intensity of the reflected beam is very high, and there is no LEED image visible; since no scattering process takes place, all reflected electrons are in the specular beam.

- LEED

  Since a diffraction pattern is formed in the back-focal plane of the objective lens, it is possible to image this pattern on the screen by removing the aperture. This working mode gets the diffraction information LEED provides from which the surface lattice structure can be derived.

- Microdiffraction

  By restricting the electron beam to only a very small area on the surface (fraction of a μm), it is possible to determine the crystal structures and orientations of small areas on the surface, such as single islands or terraces. For the IBM LEEM II system, the illumination size can be limited down to 50 nm. We use this technique for Si(001)-(2×1) and 6H-SiC(0001) surfaces as described in Chapters A and B.

- PEEM (photoelectron emission microscopy)

  The illumination source of electrons of the LEEM is switched to an ultra-violet (UV) light source making use of the photoelectric effect. The resolution is not as good as in LEEM, but at lower magnification, differences in the work function of different

materials are easily visible. There is no LEEM image visible in the intermediate image plane but the photoelectron angular distribution. This mode is often conveniently used to align the sample position to get a normal electron incidence.

- Spectroscopic imaging with energy filter

  In the PEEM mode, a sophisticated energy filter enables imaging with an energy resolution down to 250 meV with a minimal impact on the high spatial resolution in the commercialized FE-LEEM P90 system by SPECS based on the design by Tromp [55].

3.4 A novel technique: LEEM-*IV* analysis

As described above, the direct imaging of a surface area represents the reflectivity of every point in this surface region. Recording the bright-field imaging intensity against the incident electrons energy for an local area, one could extract the structural and chemical information about that local area by analyzing the electron diffraction intensities. This is the basic idea for the LEEM-*IV* technique to be tested on the PdCu surface alloy system. In this way, a high lateral spatial resolution could be obtained. The IBM LEEM II system principally reaches an spatial resolution of up to 5 nm and the ELMITECH III system up to 8 nm. Figure 3-4 illustrates the LEEM-*IV* technique. On the left, the bright-field image of the heterogeneous PdCu surface alloy at 41 eV is shown. A series of images can be acquired by changing the electron energy, and on the right side, *IV* curves can be recored from the images for two local spots indicated on the left. The differences between the two curves are evident. They can be used to distinguish the heterogeneous structures between these spots.
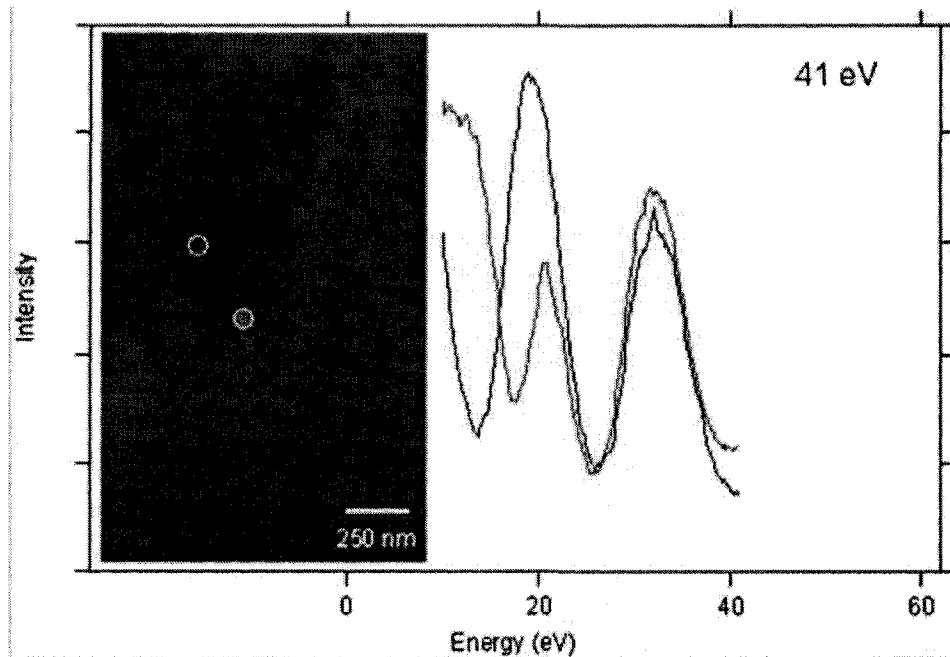
Figure 3-4: An illustration of the LEEM-*IV* technique. Left panel: the bright-field image of the heterogeneous PdCu surface alloy at 41 eV. A series of images are formed when the electron energy is ramped up. Right panel: two *IV* curves corresponding to the two spots indicated on the left panel.

The main differences between the LEEM-*IV* technique and the conventional LEED-*IV* technique are compared in Table 3.1. In spite of the big advantage of this technique in its much higher lateral resolution over the LEED technique, in practice, two of the differences impose serious challenges to the dynamical analysis of the intensity. They are (1) the relatively low electron kinetic energy in LEEM compared to LEED, and (2) the limited electron kinetic energy range in our LEEM experiments.

The electron kinetic energy in our LEEM experiments (10∼100 eV) is lower than that typically used in LEED *IV* (50∼500 eV). This complicates the quantitative analysis because, within about 50 eV of the vacuum level, the mean-free path of electrons in solids is strongly energy dependent [19]. Consequently, in calculations of the electron reflectivity, the inelastic

41

Table 3.1: Major differences between LEEM-*IV* and conventional LEED techniques.

LEEM-*IV*	Conventional LEED
Real time, *in situ*, direct imaging	Reciprocal space ($\vec{k}$-space) patterns
Reflectivity of only (00) beam	Many beams in diffraction patterns
Electron beam energy: 5~100 eV	50~500 eV
Spatial resolution: ~5 nm	Intensity averaged over an area of μm^2

damping potential (i.e. the imaginary part of the inner potential V_{im}) cannot be assumed to be constant as in conventional LEED-*IV* analysis. After evaluating various proposed models for the imaginary part of the inner potential, we found that $V_{im}(E) \propto E^{1/3}$ consistently gave the best agreement between the measured and calculated *IV* curves.

For the real part of the inner potential $V_0(E)$ (in units of eV) we used the form proposed by Rundgren for copper [56], which is based on an excited-state potential for the exchange and correlation energy of electrons by using the Hedin-Lundquist local density approximation [57, 58, 59]:

$$V_0(E) = \begin{cases} -13.4 & \text{for } E \leq 36 \text{ eV} \\ -3.6 - 65.8/\sqrt{E + 10.0} & \text{for } E > 36 \text{ eV} \end{cases} . \qquad (3.1)$$

Furthermore, we include an overall additive constant (ΔV_0) to Equation 3.1 as an independent non-structural parameter in our optimization. These energy-dependent inner potential models proved to describe the surface alloy very well. For the small energy range, careful error analyses have been performed to verify the reliability of optimized structures. More details and results will be presented in Chapter 6 where we shall demonstrate that the LEEM-*IV* works well with the PdCu surface alloy system.

CHAPTER 4

Monte Carlo simulations

4.1 Introduction

When a deterministic method is difficult, unfeasible or impossible, in solving a mathematical problem, a stochastic scheme could be conceived as a solution. The Monte Carlo (MC) simulation is such a statistical method for this need. Originally, it was a type of random method under the name of "statistical sampling". An early use of the Monte Carlo method was to evaluate high-dimension definite integrals. In the 1940s, the Monte Carlo simulation got its current name after a famous casino in Monaco in honor of the pioneer Stanislaw Ulam's uncle who was a gambler in that casino. Before this naming, a rather simple form of this method was actually used by Enrico Fermi in the 1930s [60] when he was working on neutron diffusion in Rome. Attributed to the advent of electronic computers in 1940s, a groundbreaking and far-reaching success was achieved in the application of Monte Carlo simulations to neutron multiplication in fission process. This accomplishment strongly accelerated the rapid development of the Monte Carlo method [61]. The following decades have seen broad applications of this method and its high effectiveness in solving an indeterministic problem. Today, the Monte Carlo method is used in computational physics, computational chemistry, material science, biology, video games, finance, economics, and other fields.

4.2 Metropolis Monte Carlo algorithm

The Metropolis Monte Carlo algorithm is a standard technique for statistical physics simulations. It was proposed by Metropolis and coworkers in 1953 [62]. In this algorithm, the variable, temperature, is introduced in the sampling procedure. Specifically, a Boltzmann factor is incorporated in the procedure of accepting or rejecting a trial move so that the sampling follows the Boltzman distribution property closely. This is also called importance sampling – very different from the random sampling (or simple sampling) also used in Monte Carlo simulations where all random moves are accepted in the searching space. With Metropolis' algorithm, the thermal average of a system property can be easily calculated.

Assume that a system in its initial state 0 has an energy of ϵ_0. A trial move is from the state 0 to a randomly chosen state 1 which has an energy of ϵ_1. We define the change in system energy ϵ as $\Delta\epsilon = \epsilon_1 - \epsilon_0$. T is the temperature and k the Boltzmann constant. A pseudo-number generator, to be explained in the next section, is used to produce a random number R between 0 and 1. The acceptance or rejection of the new state 1 is determined by the following decision criteria.

1) accepted, if $\Delta\epsilon < 0$; otherwise:

2) accepted, if $R < e^{-\Delta\epsilon/kT}$.

rejected, if $R > e^{-\Delta\epsilon/kT}$.

In importance sampling, the probability of a state being sampled must be the same as the actual probability of that state. Significantly, step 2 insures this requirement.

The expectation value of a physical observable, say A, can be calculated. For each move attempt i up to N, we have a value of A_i for this variable. The expected value will be the average of A_i under the condition that the sampling conforms to the Boltzmann distribution

44

$e^{-\epsilon/kT}$:

$$A = \frac{\sum A_i}{N} \tag{4.1}$$

Note that N could be a very large number leading the system to a statistically stable one since, rigorously, the above equation is only valid for an infinite number of attempts, i.e. an infinite number N.

4.3   Pseudo-random number generator

The Monte Carlo simulations rely heavily on fast and efficiently generated random numbers. For the new state 1 discussed in the preceding section, a random number is used for choosing this new state, i.e. determining which new state the system possibly moves to. Furthermore, a random number is used in the acceptance and rejection criterion. Obviously, it is crucial to have a good random number generator to give a random number uniform in the interval [0, 1]. This random number, in practice, is generated by a computing software which however makes the random number virtually deterministic. Therefore, a pseudo-random number generator generates a sequence of numbers which are not truly random. The outputs of a pseudo-random number generator only approximate some properties of the random numbers.

In our simulations, the recently invented Mersenne Twister algorithm [63] is adopted. This algorithm was developed in 1997 by Makoto Matsumoto and Takuji Nishimura. The Mersenne Twister generator, MT 19937, has many advantages over most other generators. It has a colossal period of $2^{19937} - 1$. It generates numbers equi-distributed in 623 dimensions, and runs faster than all but the most statistically unsound generators.

4.4 Constant-NVT and Constant-μVT MC simulations

In statistical physics, partition functions are connected to thermodynamical properties, however, it is hard to get analytical forms for the partition functions resulting from the complexity of a system with a huge number of particles. Multidimensional integration in the continuity case is a nearly intractable problem with the current computing power. Amazingly, the Monte Carlo simulations can solve this problem by sampling the configuration space and averaging values generated in all samplings.

Monte Carlo simulations can be designed for different ensembles, for example, the microcanonical ensemble, canonical ensemble, and grand-canonical ensemble. One can choose a most appropriate ensemble for the system under study. Here we briefly describe two ensembles, canonical ensemble and grand-canonical ensemble, used in our PdCu surface alloy study.

When the Monte Carlo simulation is applied in the canonical ensemble, the system has the number of particles N, volume V and temperature T fixed. So this method is also called constant-NVT Monte Carlo simulation. For an attempted move from an old state to a randomly selected new state, the acceptance rule obeys the Metropolis criteria described in Section 4.2. One example shown in Figure 4-1 is used to illustrate this method. It is a mixed system of components A and B with the total number of A and B, system volume, and system temperature being constant. A trial move is the location exchange of A and B. This exchange could change the system energy and numerous exchanges will ultimately lead the system to an equilibrium state. Once the equilibrium is reached, trial moves stop and the expectation values of physical variables can be obtained. We are going to use this constant-NVT simulation to simulate the Pd atom partition in the first two atomic layers.

The other ensemble we used is the grand-canonical ensemble, which is also called a

46
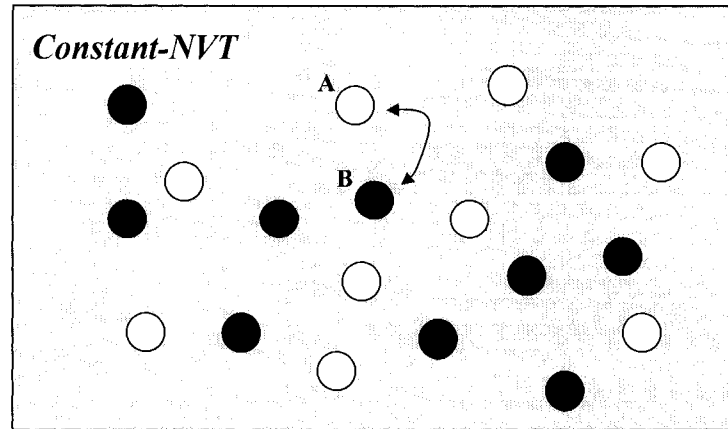
Figure 4-1: A schematic canonical ensemble of component A and B. A trial move is the swapping of A and B.

constant-μVT ensemble. In this ensemble, the temperature, volume, and chemical potential are fixed. The number of particles in a system can be obtained as a function of external conditions imposed by a reservoir. The trial moves can be the swapping of particle identities between a multiple component system and a reservoir. Figure 4-2 depicts such a system with two components of A and B. In the small inset box, two components A and B coexist. Outside the inset box, the reservoir is treated as one with only component B, even though there is an extremely small number of A after certain trial moves. The chemical potential to take out or put in one B in the reservoir is fixed and will remain the same in the simulations. A trial move will be the exchange of A in the small box with only B in the reservoir because A-A exchange does not alter the system configuration. Note that in this case, the total energy change includes two parts: one from the A-B system due to configuration change and the other from the reservoir due to the chemical potential difference between A and B. Specifically for our PdCu system, we exchange Cu atoms in a two-layer slab with Pd atoms in a reservoir with fixed chemical potential. One additional useful piece of information
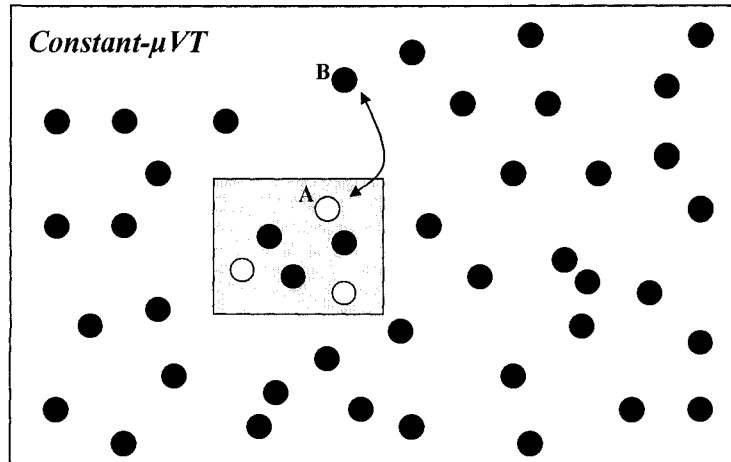
Figure 4-2: A schematic grand canonical ensemble. The system in the inset box consists of components A and B, and the reservoir outside the inset box contains only B. A trial move is the swapping of A in the system and B in the reservoir.

obtained in this simulation is the chemical potential in the slab, by which, we can judge if the surface structure is equilibrated by comparing the chemical potentials in all places of interest.

4.5 Thermodynamic integration for chemical potential calculation

Thermodynamic integration is a method to calculate the free energy and subsequently the chemical potential. The basic idea is integrating the free energy change over temperature and getting the free energy for a reference point at very high temperature so as to get the absolute value of the free energy at a given temperature. For a system of n particles, we do constant-NVT Monte Carlo simulations at a small incremental step from the system temperature to a very high temperature. The internal energy E is obtained for each temper-

48

ature in the simulations. Integrating dE/T gives entropy change at different temperatures according to

$$dS(T) = \frac{dQ}{T} = \frac{dE}{T} \tag{4.2}$$

At the reference point of a very high temperature, the system entropy is given by the Boltzmann formula

$$S = k * ln\Omega, \tag{4.3}$$

where Ω is the number of microscopic configurations of the ensemble. Then we can obtain the absolute entropy at the sample temperature.

When we vary the number of particles n in the system, this method will give the entropy difference $\Delta S(n)$ between different n at the same temperature. Subsequently, change in Helmholtz free energy will be available based on

$$\Delta F(n) = \Delta E - T * \Delta S(n). \tag{4.4}$$

One will find the chemical potential by using

$$\mu = \frac{\partial F(n)}{\partial n}. \tag{4.5}$$

This method, although involving much simulation and integration work, offers another way to obtain the chemical potential in addition to the constant-μNT simulation addressed in the last section. Both of these two methods have been tried on the Pd/Cu alloy system. In chapter 6, it will be demonstrated that they produce similar results and lead to the same conclusions.

CHAPTER 5

The 3 low-index surfaces of the semimetal bismuth

Bismuth is a group V semimetal. The total density of electrons (and the total density of holes) in Bi is about 3×10^{17} cm^{-3} – down from typical metallic densities by about a factor of 10^5. The effective masses of the carriers are small; for electrons along the trigonal axis $m^* \approx 0.003\ m_e$ where m_e is the electron mass [64]. The resistivity of Bi is typically 10 to 100 times larger than that of most metals. Bi crystallizes in the rhombohedral ($A7$) structure with two atoms in one unit cell. It has an electronic configuration of [Xe]4f^{14}5d^{10}6s^{2}6p^3. Having an even number of conduction electrons per primitive rhombohedral cell, they come very close to being insulators, but there is a slight band overlap, leading to a very low density of states at the Fermi level and a very small number of carriers. As a result, the pentavalent semimetals provide a striking illustration of the crucial importance of the crystal structure in determining metallic properties. Were it exactly a simple cubic Bravais lattice, then, having an odd valence, they would be very good metals indeed. Furthermore, theoretical work has shown that the balance between being a semiconductor or a semimetal depends crucially on the structural details [65].

This structural importance could also happen to the surfaces due to the atomic geometry change and broken symmetry. In fact, this has been manifested on the Bi surfaces. Bi surface

electronic properties have been found to be radically different from the bulk. Fascinatingly, the Bi(110) [66], Bi(001) [67] and Bi(111) [68, 69] surfaces prove to possess metallic surface states. See Ref. [70] for a detailed review by Hofmann. The metallic surface states could be caused by surface modifications due to the local atomic environment and symmetry changes. It is well known that a semiconductor, e.g. the Si(001) surface, can reconstruct into another semiconductor, not a metal. For Bi(110) and Bi(001), however, the absence of any reconstructions is unexpected and in sharp contrast to the situation on most semiconductor surfaces. Explaining the lack of the reconstruction with simple arguments is not possible.

A particularly interesting effect impacting the surface electronic structure is spin-orbit splitting. The spin-orbit interaction in the heavy element Bi is very strong. In the bulk band structure, the spin-orbit interaction is important [71] but it does not lead to a splitting of the bands with respect to the spin (i.e. to a lifting of the Kramers degeneracy) because of the inversion symmetry of the bulk structure. On the surfaces, however, no inversion symmetry is present and the surface state bands are split with respect to their spin direction [66, 72]. So far, no direct measurements of the spin-dependent surface band structure have been reported and the evidence for the spin-orbit splitting is the excellent agreement between the measured surface state dispersion and that calculated from first principles with the inclusion of the spin-orbit interaction [72]. Additional direct evidence is found in the quasiparticle interference pattern on Bi(110) [73].

Practically, when a semimetal turns into a metal, this good metallic metal on a semimetal can be taken as a model for a nearly two-dimensional metal. The surface states can be used for the field of spintronics due to its unique spin-orbit splitting features. The spin-orbit splitting of the bands will change band structure and Fermi contour. Surface state bands have a profound impact on effects like screening. The surface dictates the chemical prop-

erties of a solid. The surface importance even increases sigificantly for smaller structures. Properties of bulk Bi can be altered by quantum size effects [74]. Examples of length-scale and dimensionality related novel phenomena are: the thickness dependence of transport properties in Bi thin films [75], metal-to-semimetal transition in Bi nanowire [76], super-conductivity in granular films of Bi clusters [77], Bi ultra-thin film phase transition on Si(111) [78], and Bi thin film as a template for an organic semiconductor growth [79]. All could contribute to potential applications in relevant nanotechnology.

Although the creation or increase of surface could play an important role in the non-bulk structures, the surface structures of Bi have been largely unexplored since the pioneering qualitative work of Jona [80]. This chapter presents quantitative results for Bi(111) [81], (110) [82] and (001) surfaces.

5.1 The bismuth bulk structure

Bismuth has a rhombohedral ($A7$) crystal structure composed of two interpenetrating face-centered-cubic sublattices slightly stretched in the [111] direction [83]. There are two atoms per unit cell and three nearest neighbors for each Bi atom. The structure can be viewed as a stacking of covalently bonded bilayers in the [111] direction with much weaker bonds between these bilayers. This picture is confirmed by the overall mechanical properties of Bi which is brittle and easily cleaves along the (111) plane, presumably between two bilayers. Represented by both rhomboheral and hexagonal lattices, the lattice structure is shown in Figure 5-1. The bisectrix (C_1), binary (C_2), and trigonal (C_3) axes are taken to be the x, y, and z coordinate axes, respectively. The hexagonal lattice vectors are denoted as $\mathbf{a}$ and $\mathbf{c}$. The $\mathbf{c}$ axis lies in the rhombohedral [111] direction. The lattice constants are $a = |\mathbf{a}| = 4.535$ Å and $c = |\mathbf{c}| = 11.814$ Å at 78 K, as listed in Table 5.1. Three primitive lattice vectors in
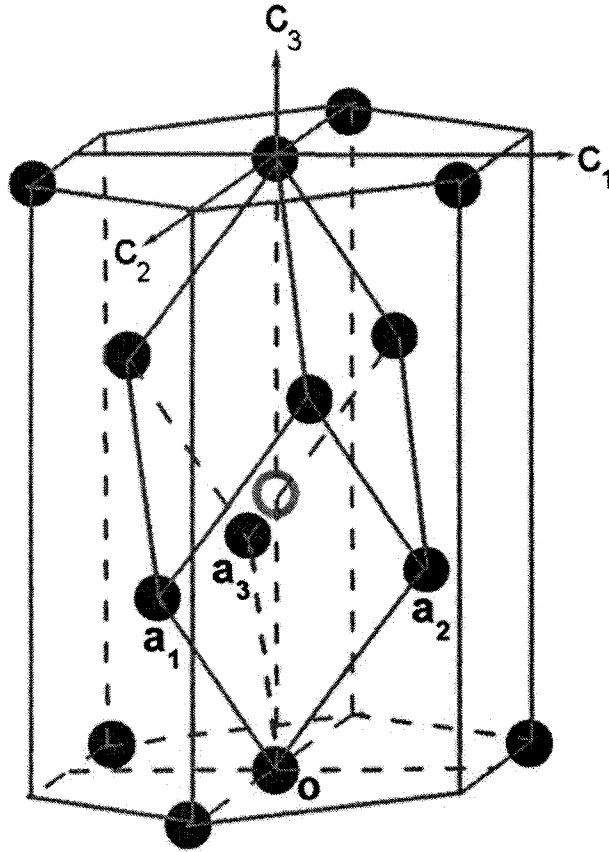
Figure 5-1: The crystal structure of Bi is indexed by both rhombohedral and hexagonal systems. In the rhombohedral unit cell, the central atom is indicated by a circle and the lattice vectors are shown as a_1, a_2, a_3 referred to the origin point $\mathbf{O}$. C_1, C_2 and C_3 are bisectrix, binary and trigonal axes, respectively.

the rhomboheral frame are denoted as a_1, a_2 and a_3. The conversion between the two sets of lattice constants is as follows.

$$\begin{cases} a_1 = (-a/2, -\sqrt{3}a/6, c/3), \\ a_2 = (a/2, -\sqrt{3}a/6, c/3), \\ a_3 = (0, \sqrt{3}a/3, c/3). \end{cases} \quad (5.1)$$

53

Table 5.1: Lattice constants of Bi in the hexagonal system at different temperatures.

	78 K	298 K
a (Å)	4.535	4.546
c (Å)	11.814	11.862

5.2 The Bi(111) surface

A quite different picture of the surface electronic structure of Bi(111) was recently presented by Ast and Höchst [84]. They have shown that very good agreement between the measured surface state dispersion and a tight-binding calculation can be obtained for a very weak spin-orbit coupling parameter. However, in order to achieve this, a strong outward relaxation of the first interlayer spacing had to be assumed. This relaxation is $\Delta d_{12}/d_{12}^{b} = 71$ % where Δd_{12} is the change in the first to second interlayer distance and d_{12}^{b} ($= 1.59$ Å) is the truncated bulk value for this distance. Such a big interlayer relaxation would be highly unusual. Moreover, the first interlayer spacing, d_{12}, would be larger than the inter-bilayer distance d_{23}, leading to a completely different type of bonding at the surface. In the first-principles calculations presented in Ref. [72] and here, the situation is quite different: they also give very good agreement with the experimental surface band structure but the spin-orbit splitting of the bands is pronounced and the interlayer relaxations are small. A direct structure determination of Bi(111) is therefore required.

The amount of structural information on the Bi surfaces in general and Bi(111) in particular is very limited. In a pioneering work, Jona has analyzed the LEED patterns for different Sb and Bi surfaces [80]. For Bi(111) he found a hexagonal (1 × 1) pattern and assumed that the surface was terminated with a short first interlayer spacing, i.e. with an

intact bilayer. A later scanning tunneling microscopy investigation by Edelman *et al.* [85] supported the presence of only one termination. However, the detailed surface atomic configuration is so far unknown.

Here we present an experimental study of the surface structure of clean Bi(111) by LEED *IV* analysis. Experimental diffraction intensities taken at sample temperatures of 140, 171, 218, 268 and 313 K at normal incidence and 139 K at off-normal incidence with polar angles $\theta = \pm 10°$ have been analyzed by comparison to dynamical LEED calculations. The optimization of the structural and non-structural parameters was carried out by minimizing a reliability (R) factor with the quadratic tensor model algorithm of Hanson and Krogh [40]. Two different surface models were tried: a termination with an intact bilayer and a termination with a broken bilayer. The agreement between measured and calculated intensities is excellent for the intact bilayer. The most important results are the structural parameters, i.e. the layer relaxations, and the mean-square vibrational amplitude of the surface atoms.

5.2.1 The bulk-truncated Bi(111) surface structure

The truncated bulk crystal structure of Bi(111) is shown in Figure 5-2. For the figure, we have assumed that the crystal is terminated with a Bi bilayer. By considering only the (1×1) LEED diffraction pattern reported by Jona [80], a different termination would also be possible: the surface could be terminated with a long first interlayer spacing, i.e. with a bilayer cut upon surface creation. This is inconceivable because of the covalent bonds that hold the bilayer together. We have indicated the locations of these bonds in the figure. To create a surface terminated with an intact bilayer, no covalent bonds have to be broken. The formation of a split bilayer, on the other hand, requires the breaking of three covalent

○ 1st layer
● 2nd layer
● 3rd layer
◉ 4th layer

(a) top view

mirror plane(s)

4.538 Å

4.538 Å

(b) side view (parallel to mirror plane)

1.594 Å

2.347 Å
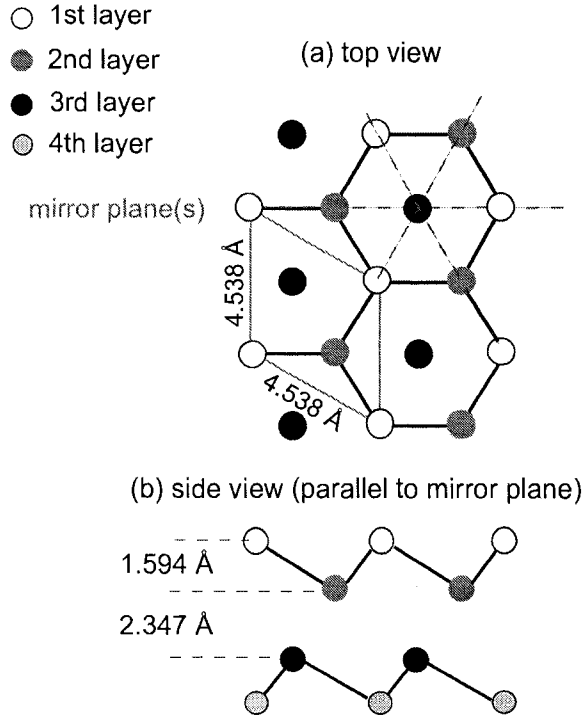
Figure 5-2: Truncated-bulk structure of Bi(111). The dark solid lines indicate covalent bonds between the atoms within the bilayers. (a) Top view of the first three atomic layers. Each layer consists of a two-dimensional trigonal lattice and the lattice constants are given. The mirror planes of the structure are also shown as dashed lines. (b) Side view (projected onto a mirror plane) of the first four layers. The alternating short and long interlayer spacings are evident.

bonds per surface unit cell. This picture is confirmed by the overall mechanical properties of Bi which is brittle and easily cleaves along the (111) plane, presumably between two bilayers. The bilayer-type structure gives rise to alternating interlayer distances. For the truncated bulk at 140 K we have: d_{12}^b =1.594 Å, d_{23}^b =2.347 Å, d_{34}^b =1.594 Å, d_{45}^b =2.347 Å and so on.

In the hexagonal system, the lattice constants for 78 K and 298 K are given in Table 5.1 [86]. Based on these lattice constants, we get the linear thermal expansion coefficients parallel and perpendicular to the (111) plane as 11.0×10^{-6} K^{-1} and 18.5×10^{-6} K^{-1}, re-

spectively, which are consistent with thermal expansion coefficients reported by Erfling [87]. We obtain the lattice constants for 140, 171, 218, 268 and 313 K by interpolation.

5.2.2 Methods

Experiment

The experiment was performed in a μ–metal ultra-high vacuum chamber with a base pressure of $7 \cdot 10^{-9}$ Pa. It is equipped with a four-grid LEED optics from Omicron. Surface contamination was measured by Auger Electron Spectroscopy (AES) using a hemispherical electron analyzer and the LEED electron gun as an electron source. The sample was mounted on a manipulator, allowing positioning to within 0.1° around all three axes of the crystal. The sample was cooled by liquid nitrogen. The sample temperature was adjusted via liquid nitrogen flow.

The surface was cleaned by cycles of Ar^+ sputtering (1 kV, $2\mu A$) and annealing to 150°C. With AES no surface contamination could be detected. Figure 5-3 shows an Auger spectrum with incident electron energy of 3 keV. The dominant peak and trough around 100 eV is by Bi. The maximum possible oxygen contamination was determined to be 0.02 monolayers.

Spot intensities were measured using a 16 bit Charge-Coupled Device (CCD) camera. A back-illuminated and Peltier cooled (−40°C) CCD chip guaranteed an extraordinarily high quantum efficiency. The camera was mounted on a base, which allowed rotation around all three axes. Great care was taken to align the camera with respect to the electron gun and the Bi crystal.

To obtain intensities of the diffracted beams as a function of electron energy, the following procedure was employed: A series of images was recorded within the energy range
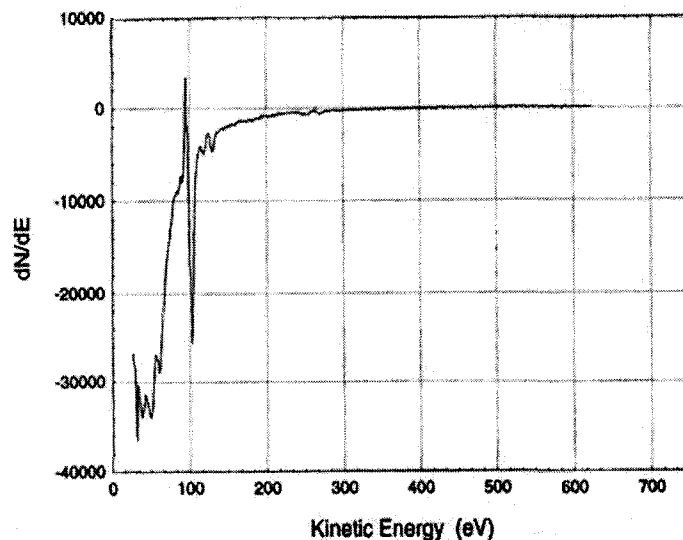
Figure 5-3: Auger electron spectrum of the cleaned Bi(111) surface. The incident electron is 3 keV in kinetic energy. No surface contamination is detected except the strong Bi peak around 100 eV.

from 30 eV to 350 eV, while the energy was increased in steps of 1 eV after every recorded image. The integrated spot intensity of every single diffracted beam hk was extracted from these images. Normal incidence was found by minimizing the R factor between symmetry-equivalent beams. In the final data set, the intensities of the symmetry-equivalent beams were averaged.

LEED calculations and R factor analysis

The dynamical LEED calculations were performed using the computer code of Adams [38, 39] which was developed from the programs of Pendry [17] and of Van Hove & Tong [18]. Atomic scattering phase shifts have been calculated using a muffin-tin potential model and the standard Barbieri/Van Hove phase shift package available online [41]. A muffin tin radius of 2.87 atomic units has been adopted for Bi. Variations in the muffin tin radius have

proved non-significant for the structure determination. Furthermore, the phase shifts have been renormalized by the thermal effects of root-mean-square (rms) isotropic vibrational amplitudes. Up to 17 phase shifts have been used because of the strong scattering of the heavy Bi atom ($Z = 83$), especially at energies above 300 eV. The muffin-tin constant V_0 and the imaginary damping potential V_{im} were both taken to be energy-independent. The surface potential step of height V_0 was located half a short bulk interlayer spacing away from the topmost layer. The reflection and transmission matrices for composite layers were calculated using Van Hove and Tong's combined space method [18]. The reflection matrices for the bulk crystal were calculated by Pendry's layer-doubling method [17]. The agreement between experimental and calculated LEED intensities is quantified by the R_2 factor defined in Equation 2.31.

Ab-initio calculations

Our collaborators performed *ab initio* calculations of the surface crystal structure of Bi(111). The full-potential linearized augmented plane wave method in film-geometry [88, 89] as implemented in the FLEUR-code was used and the local density approximation [90] to the density functional theory was employed. Spin-orbit coupling was included in the self-consistent calculations [91]. The evaluation of the surface relaxation has been carried out for the symmetric 14-layer film, both, with the inclusion of the spin-orbit coupling (SOC) term and without this term. Force calculations have been performed for the first four interlayer spacings without spin-orbit coupling while the total energy computations have been carried out for the first two interlayer spacings with the inclusion of SOC. As the latter evaluations are computationally more demanding we kept the d_{34} and d_{45} interlayer spacings equal to those obtained from the force calculation. The geometry was chosen such that both sides

of the film were terminated with an intact bilayer. A wavefunction cutoff of 3.6 a.u.$^{-1}$ was chosen and the irreducible part of the Brillouin zone was sampled with 21 **k**-points.

5.2.3 Results

Normal incidence at different temperatures

After some initial tests with both structural models for the truncated bulk, the model involving a cut bilayer, i.e. a long first interlayer spacing, was discarded because of the poor agreement with the experimental data. The structural and non-structural parameters for the surface terminated with an intact bilayer were refined using the procedure outlined above. The optimized parameters for a sample temperature of 140 K are listed in Table 5.2. These are the interlayer spacings d_{ij}, the rms atomic vibrational amplitudes u in the surface layers, the real part of the inner potential V_0, the damping potential V_{im}, and the global scaling constant c . The Debye temperatures are calculated according to the relation between Debye temperature Θ_D and mean-square atomic vibrational displacement $\langle u^2 \rangle_T$ at sample temperature T [17]

$$\langle u^2 \rangle_T = \frac{9\hbar^2}{m_a k_B \Theta_D} \left\{ \frac{T^2}{\Theta_D^2} \int_0^{\frac{\Theta_D}{T}} \frac{x dx}{e^x - 1} + \frac{1}{4} \right\} \tag{5.2}$$

where m_a is the atomic mass, $\hbar$ Planck's constant and k_B the Boltzmann constant. At a sample temperature of 140 K ten symmetry in-equivalent beams with a total energy range of 2079 eV have been used to minimize the R factor. For comparison, the Pendry R factor for the agreement between calculated and experimental spectra is found to be $R_p = 0.25$. It should be emphasized that a proper comparison requires a full and independent optimization of R_p, which is not performed in the present work. Experimental and calculated intensity-energy curves are shown in Figure 5-4. The excellent agreement between the experimental

60

Table 5.2: Optimum parameter values for the surface structure of Bi(111) at 140 K and normal incidence. Interlayer spacings between the ith and jth layer are indicated as d_{ij}; rms vibrational amplitudes for atoms in the ith layer are denoted as u_i. V_0 and V_{im} are the real part and imaginary part of inner potential, respectively. c is the global scaling constant. d^b is the corresponding interlayer spacing of the truncated bulk at 140 K. Θ_D is the Debye temperature calculated from u_i.

Parameters	starting values	optimized values	$\frac{\Delta d}{d^b}$ (%)	Θ_D (K)
V_0 (eV)	4.0	3.61 ± 0.54	-	-
d_{12} (Å)	1.594	1.602 ± 0.018	$+0.5 \pm 1.1$	-
d_{23} (Å)	2.347	2.393 ± 0.018	$+1.9 \pm 0.8$	-
d_{34} (Å)	1.594	1.594 ± 0.018	0.0 ± 1.1	-
u_1 (Å)	0.1433	0.239 ± 0.019	-	71^{+7}_{-5}
u_2 (Å)	0.1433	0.222 ± 0.020	-	77^{+8}_{-7}
V_{im} (eV)	4.0	4.34 ± 0.57	-	-
c	2.4×10^6	$5.8 \pm 2.1 \times 10^6$	-	-
R factor	0.198	0.075	-	-

and calculated results is evident.

The sensitivity of the R factor to the optimization parameters of interlayer spacings and atomic vibrational amplitudes has been investigated in the case of $T = 140$ K. Figure 5-5 shows the R factor as a function of these parameters individually. All the sensitivity curves take on a parabolic shape as discussed in Refs. [92, 39]. As expected, we can see a larger sensitivity of the R factor to the interlayer spacings than to the atomic vibrational amplitudes. From the error analysis outlined above, we determine that one standard deviation
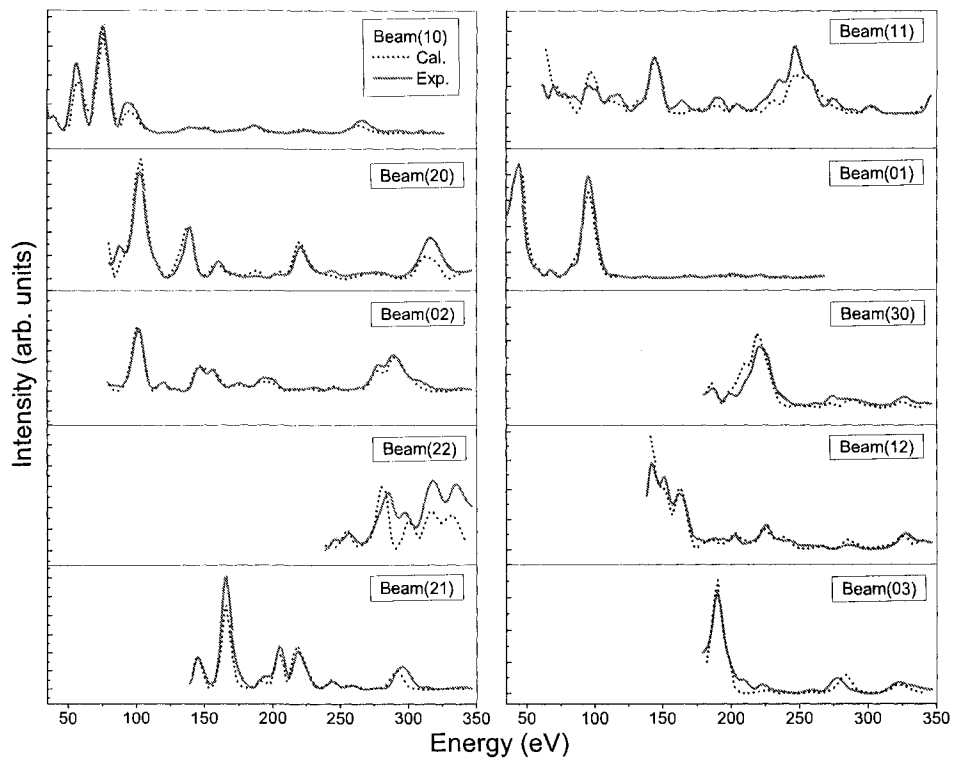
Figure 5-4: Comparison of experimental and calculated intensity versus energy curves for normal incidence on Bi(111) at 140 K. Solid lines show experimental data and dotted lines show calculated data.
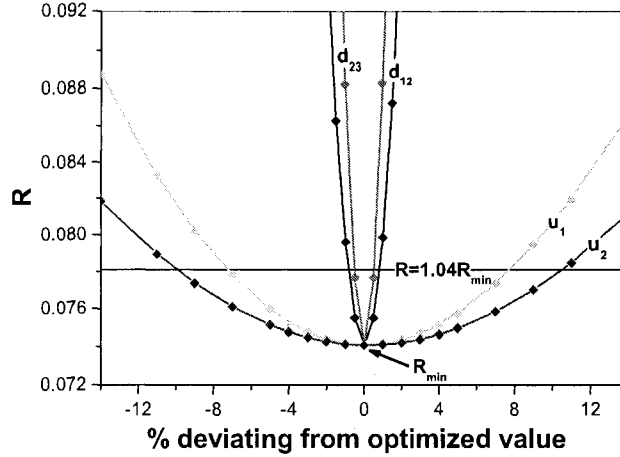
Figure 5-5: Sensitivity of R factor to deviations from the optimized parameter values d_{12}, d_{23}, u_1, u_2 at 140 K. R_{min} is the minimized R factor. The intersections between $R = 1.04R_{min}$ and the sensitivity curves correspond to the uncertainty in the individual parameters.

corresponds to 4 % increase of the R factor with respect to its minimum, i.e. $R = 1.04R_{min}$. Hence, the intersections between $R = 1.04R_{min}$ and the sensitivity curves correspond to the error bars of the individual parameters.

The optimized parameters for the complete set of temperatures are given in Table 5.3 together with the number of beams and the total energy range. The first interlayer spacing shows no significant relaxation in the temperature range studied while the second interlayer spacing shows a small expansion.

The changes of rms atomic vibrational amplitudes with temperature for the first two layers are shown in Figure 5-6. The corresponding Debye temperatures as calculated from Equation 5.2 are also given. It is found that the first two layers exhibit lower Debye temperatures than the bulk for all sample temperatures investigated. Note that the Debye temperature for the first two layers increases slightly with sample temperature. There are two reasons for this. The first is the experimental uncertainty in the determination of u

63

Table 5.3: Optimized parameters for different sample temperatures. ΔE is the total energy range for all the beams. d_{ij}^{b} is the distance between the ith layer and jth layer in the bulk at the corresponding temperature. Θ_{D1} and Θ_{D2} are the optimized Debye temperatures for the atoms in the first and second layers, respectively.

T	No. of	ΔE	$\frac{\Delta d_{12}}{d_{12}^{b}}$	$\frac{\Delta d_{23}}{d_{23}^{b}}$	u_1	u_2	Θ_{D1}	Θ_{D2}	V_0	V_{im}	R
(K)	beams	(eV)	(%)		Å	Å	(K)		(eV)	(eV)	factor
140	10	2079	0.5 ± 1.1	1.9 ± 0.8	0.239 ± 0.019	0.222 ± 0.020	71^{+7}_{-5}	77^{+8}_{-7}	3.61 ± 0.54	4.34 ± 0.57	0.075
171	10	2068	0.0 ± 1.1	2.1 ± 0.8	0.256 ± 0.019	0.237 ± 0.020	74^{+6}_{-5}	80^{+7}_{-6}	3.71 ± 0.53	4.22 ± 0.56	0.084
218	9	1375	-0.4 ± 1.3	2.0 ± 0.9	0.260 ± 0.023	0.248 ± 0.023	82^{+8}_{-7}	86^{+8}_{-5}	3.96 ± 0.61	4.01 ± 0.70	0.072
268	9	1207	-0.4 ± 1.5	1.6 ± 1.1	0.284 ± 0.024	0.268 ± 0.024	83^{+8}_{-6}	88^{+8}_{-7}	4.21 ± 0.73	4.20 ± 0.77	0.069
313	7	555	-0.4 ± 2.9	1.0 ± 1.9	0.289 ± 0.049	0.266 ± 0.049	88^{+18}_{-13}	96^{+12}_{-11}	4.61 ± 1.44	3.97 ± 1.49	0.043
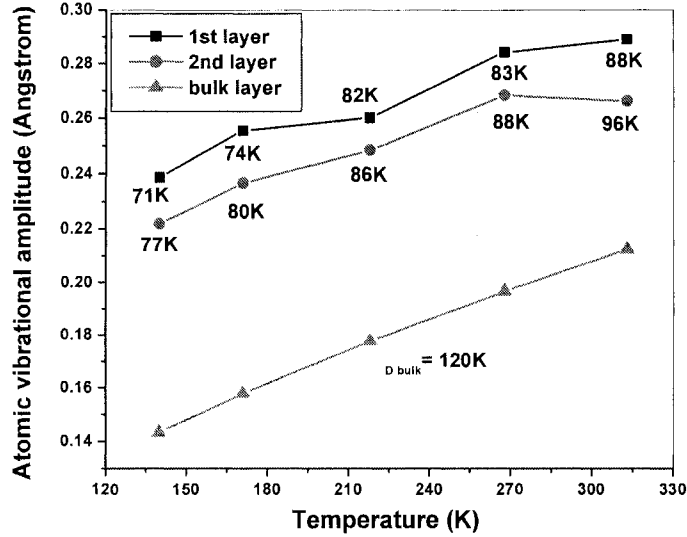
Figure 5-6: Optimized root-mean-square atomic vibrational amplitudes with error bars for the first and second top layers. Corresponding Debye temperatures are indicated for comparison with the bulk Debye temperature $\Theta_{D\ bulk} = 120$ K [5].

and the second is that the Debye model is only a very simple approximation.

Comparison to first-principles calculations

The first-principle calculations performed with the inclusion of spin-orbit interaction give bulk short and long interlayer spacings of 1.667 Å and 2.228 Å, respectively. Scalar relativistic evaluations, that do not include the SOC term, lead to a very slight modification (of approximately 1 %) of these results. To check the sensitivity of the surface relaxation to the number of atomic layers incorporated into the relaxation, we have computed the 14-layer Bi(111) film without the SOC term for two geometries. In the first geometry only the two surface layers were allowed to relax to the equilibrium and in the second geometry the four surface layers have been relaxed. Both these calculations result in a small contraction

of the first interlayer spacing ($\Delta d_{12}/d_{12}^{\mathrm{b}} \simeq -0.6$ %) and in an expansion of the second one ($\Delta d_{23}/d_{23}^{\mathrm{b}} \simeq +6.6$ %). The third interlayer spacing d_{34} ($d_{34}^{\mathrm{b}} = d_{12}^{\mathrm{b}}$ in bulk Bi) also experiences a small contraction similar to Δd_{12} while the fourth one expands by $\Delta d_{45}/d_{45}^{\mathrm{b}} \simeq +2.3$ %, i.e. significantly less than the expansion of the d_{23} distance. The inclusion of spin-orbit interaction into the calculation results in a small expansion of the d_{12} distance, $\Delta d_{12}/d_{12}^{\mathrm{b}} = +0.6$ %, and in an expansion of the second interlayer spacing, $\Delta d_{23}/d_{23}^{\mathrm{b}} = +6.2$ %. These data can be compared with the experimental results linearly fitted and extrapolated to 0 K which are: $\Delta d_{12}/d_{12}^{\mathrm{b}} = +(1.2 \pm 2.3)$ % and $\Delta d_{23}/d_{23}^{\mathrm{b}} = +(2.6 \pm 1.7)$ %. For the $\Delta d_{12}/d_{12}^{\mathrm{b}}$ relaxation a very good agreement is obtained with the computed value when the SOC term is included.

For $\Delta d_{23}/d_{23}^{\mathrm{b}}$ the theoretical value clearly lies outside the experimental error but the agreement can still be judged to be fair in view of the remaining uncertainties. In Figure 5-7 we show the calculated difference between total energies per surface atom for the films, as a function of the relaxation for the first and the second interlayer spacings as well as the whole energy landscape around the obtained energy minimum. The $\Delta d_{12}/d_{12}^{\mathrm{b}}$ relaxation curve (open squares) was computed keeping $\Delta d_{23}/d_{23}^{\mathrm{b}} = 0$ %, while the d_{23} was relaxed keeping $\Delta d_{12}/d_{12}^{\mathrm{b}} = 1$ % (open circles). As one can see in the figure, Δd_{23} shows an extremely weak energy dependence. For instance, the energy difference between $\Delta d_{23}/d_{23}^{\mathrm{b}} = 2$ % and $\Delta d_{23}/d_{23}^{\mathrm{b}} = 6$ % is about 4.3 meV/surface atom. This very small quantity can be influenced by the choice of the approximation for the exchange-correlation potential, by the finite thickness of the slab, by small inconsistencies in the **k**-point sampling between bulk and film calculations, as well as by the fact that the linear extrapolation to 0 K may be oversimplified.
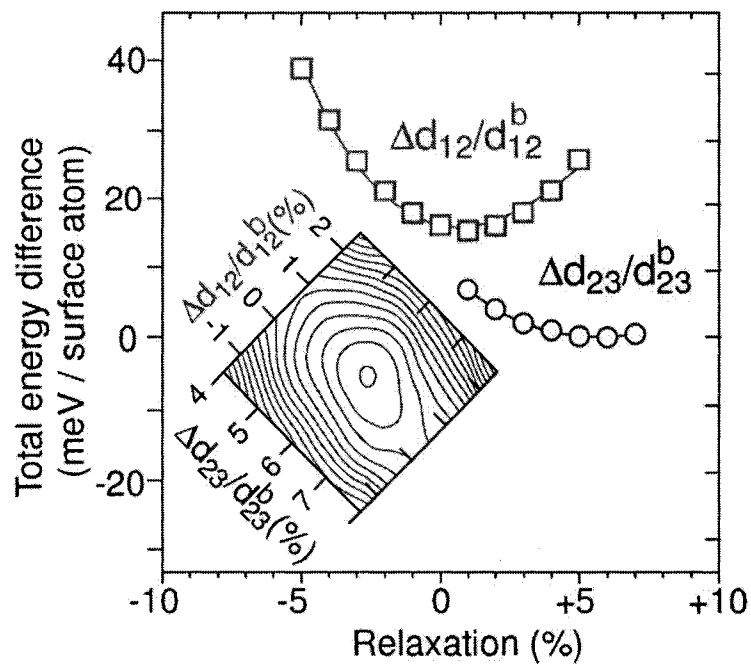
Figure 5-7: Calculated energy changes for relaxations close to the optimum value. $\Delta d_{12}/d_{12}^b$ was computed keeping $\Delta d_{23}/d_{23}^b = 0$ % while $\Delta d_{23}/d_{23}^b$ was calculated keeping $\Delta d_{12}/d_{12}^b = 1$ %. Inset: contour plot of the energy as a function of $\Delta d_{12}/d_{12}^b$ and $\Delta d_{23}/d_{23}^b$. The energy difference between the contour lines is 1/6 meV / surface atom.

Table 5.4: Optimized results for two different off-normal incident angles on the Bi(111) surface at 139 K. Θ_{D1} and Θ_{D2} are the optimized Debye temperature for the atoms in the first and second layers, respectively. Interlayer spacing d_{ij} are fixed at optimized values from normal incidence.

Incident angle θ	Optimized angle	No. of beams	ΔE (eV)	Θ_{D1} Θ_{D2} (K)	c	ΔV_0 (eV)	V_{im} (eV)	R-factor
+10	10.48	52	9044	80.3 ± 10 109.8 ± 18	$1.9 \pm 0.4 \times 10^6$	5.99 ± 0.26	3.78 ± 0.35	0.089
−10	-9.99	50	8990	81.5 ± 9 102.3 ± 14	$2.2 \pm 0.5 \times 10^6$	6.50 ± 0.37	4.02 ± 0.39	0.107

Off-normal incidence with $\theta = \pm 10°$ at 139 K

As complementary measurements to confirm the surface structure determined by normal incidence, off-normal incidence are performed. Due to the broken symmetry of the beams resulting from the off-normal incidence, there are much more symmetry-inequivalent beams used for optimization. For the $\theta = \pm 10°$, 52 and 50 beams and 9044 and 8990 eV of the total energies are compared, respectively. Small R factors and optimized results are shown in Table 5.4. The polar angle optimized are $10.48°$ and $-9.99°$ in the two situations which are very close to the measured values of $10°$ and $-10°$. The interlayer spacings are fixed as the optimized values from the normal incidence. The optimum parameter values for $\theta = +10°$ and $\theta = -10°$ are very close to each other. Compared with those for the normal incidence at 140 K, the results for the off-normal incidences show minor differences which are not significant when taking the error into account.

A representative set of experimental and calculated intensity-energy curves for the $\theta = +10°$ are shown in Figure 5-8. Obviously an excellent agreement between the experimental and calculated intensities has been obtained.
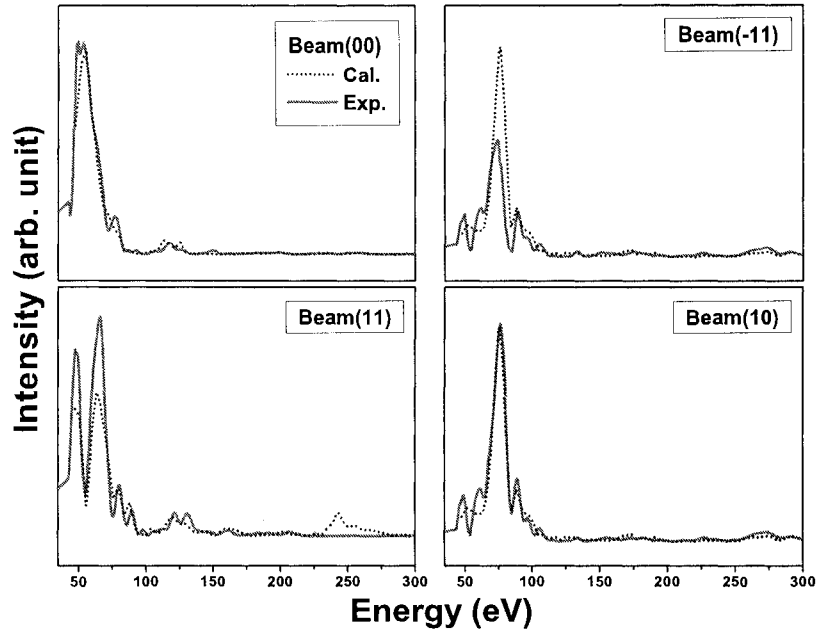
Figure 5-8: Comparison of experimental and calculated IV curves for some beams at 139 K and off-normal incidence on Bi(111) with polar angle $\theta = 10°$

5.2.4 Discussion and summary

Our results give a consistent picture of the surface geometric structure of Bi(111). The most important result is the fact that the relaxations are quite small, unlike the values assumed in the tight-binding fit to the electronic structure in Ref. [93]. Indeed, moderate relaxations would be expected for a system like Bi(111) that can be viewed, drastically simplified, as a stack of covalent bilayers bound by van der Waals-like bonds. It is even conceivable that the relaxation in d_{23} should be bigger than that in d_{12}. The argument is again that the much stronger bonds within a bilayer would be modified less upon a change in the environment.

Another interesting result is the reduced surface Debye temperature for the first two atomic layers. This finding is consistent with a very early study of Goodman and Somorjai [94]. Reduced surface Debye temperatures are a common phenomenon on many surfaces.

69

The actual numerical values of the surface Debye temperature are an important ingredient for the determination of the electron-phonon coupling strength from angle-resolved photoemission data [95, 96].

Finally, there are some interesting technical issues worth mentioning. The QTM algorithm introduced for the R factor minimization by Adams has been tested [37] for the surface structure determination of clean Al(110), Al(100)-$c(2\times2)$-Li and Al(111)-(2×2)-Na. The results obtained by this new procedure showed an excellent agreement with those from a simple grid-search procedure [36, 97]. Some advantages have been shown and discussed, including (i) the rapid convergence to the optimum values, (ii) the ability to define linear correlations between search parameters and perform parameter optimization within defined intervals (iii) the capability of optimizing both the structural and nonstructural parameters simultaneously. These characteristics have been confirmed by our calculations. Tests for some more complicated systems, such as surface alloy structures, are under way. An important feature in our optimization is the employment of a global scaling constant c for all beams, which makes the R factor retain the information of relative intensities from beam to beam.

5.3   The Bi(110) surface

From a chemical point of view, the creation of a surface requires the breaking of atomic bonds. Covalent bonding plays only a minor role in most metals. Thus the effect of bond-breaking is small and surface properties are similar to those of the bulk, although localized electronic surface states may be present. On semiconductors, creating a surface leaves so-called dangling bonds which should give rise to half-filled and therefore metallic bands. However, it turns out that on most semiconductor surfaces the atoms re-arrange their

positions such that the dangling bonds are removed and the surface is again a semiconductor and not a metal [98]. Semimetals such as bismuth lie in between these two cases. On the one hand, a semimetal is close to being a semiconductor since directional bonding is important and the valence and conduction bands are almost separated by a gap. On the other hand, there is a very small overlap between both bands such that the material is formally a metal. This delicate balance between being a metal and a semiconductor depends crucially on the atomic structure [65] and it can be expected to be severely disturbed at the surface.

The Bi(111) surface structure has been presented in the last section. One important difference between bulk terminated Bi(110) and Bi(111) is that the Bi(110) surface exhibits dangling bonds, while Bi(111) does not. In a pioneering study by Jona [80], oxygen adsorption experiments suggest that Bi(110) is noticeably more active than Bi(111). A qualitative analysis of LEED patterns in Jona's study shows an unreconstructed (1×1) Bi(110) surface structure. From the bulk structure Jona erroneously concluded that the unit cell (and hence the LEED pattern) should not be exactly rectangular but that the lattice vectors should include an angle slightly different from 90°. This is not correct, as will become apparent below. The unit cell is rectangular and almost square. A recent scanning tunneling microscopy study by Pascual et $al.$ [73], revealed images of the Bi(110) surface that are consistent with a near-square surface unit cell.

In contrast to most metal surfaces, Bi(110) has a very low symmetry - the only symmetry element being a mirror plane while it has no translational symmetry normal to the surface. This makes the LEED-IV analysis of this surface challenging. Along the [110] direction the Bi has a close stacking of atomic layers, i.e. the buckled bilayer as described below that requires the combined space method [18] to calculate diffraction matrices. The stacked layers have a registry that does not repeat itself, or in other words, the stacking sequence

has an infinite repeat distance due to its non-symmetrical translation parallel to the mirror plane. More importantly, the dangling bonds at the surface may complicate the surface electronic and geometrical structures, which makes this open surface quite similar to many semiconductors and binary compounds.

We report on a study of the surface structure of clean Bi(110) by quantitative LEED *IV* analysis. Experimental diffraction intensities taken at a sample temperature of 110 K under normal incidence have been analyzed by comparison to dynamical LEED calculations. Great care was taken to align the sample considering the low symmetry diffraction pattern. The main structural parameters that were optimized in the LEED-*IV* analysis include the first 4 interlayer spacings and the Debye temperatures for the first 2 surface layers. The experimental relaxations are in good agreement with those from first-principles calculations by our collaborators.

5.3.1   The bulk-truncated Bi(110) surface structure

The bulk truncated surface structure of Bi(110) is shown in Figure 5-9. Each atom has three nearest neighbors to which it is connected by quasi-covalent bonds. The side views show the stacked bilayers loosely bound by a single bond between every other atom in neighboring bilayers. Within one bilayer, each atom in one layer closely bonds with two nearest-neighbor atoms in the other layer forming a buckled structure. The covalent bonds have been drawn by solid lines and the dangling bonds at the surface layer by dashed lines. The bilayer-type structure gives rise to alternating interlayer distances. For the truncated bulk at 110 K we have: $d_{12}^{\mathrm{b}} = 0.208$ Å, $d_{23}^{\mathrm{b}} = 3.064$ Å, $d_{34}^{\mathrm{b}} = 0.208$ Å, $d_{45}^{\mathrm{b}} = 3.064$ Å, and so on. Interlayer spacings between the ith and jth bulk layers are indicated as d_{ij}^{b}. Noticeably, the Bi(110) surface has very low symmetry: the only symmetry element is a mirror plane
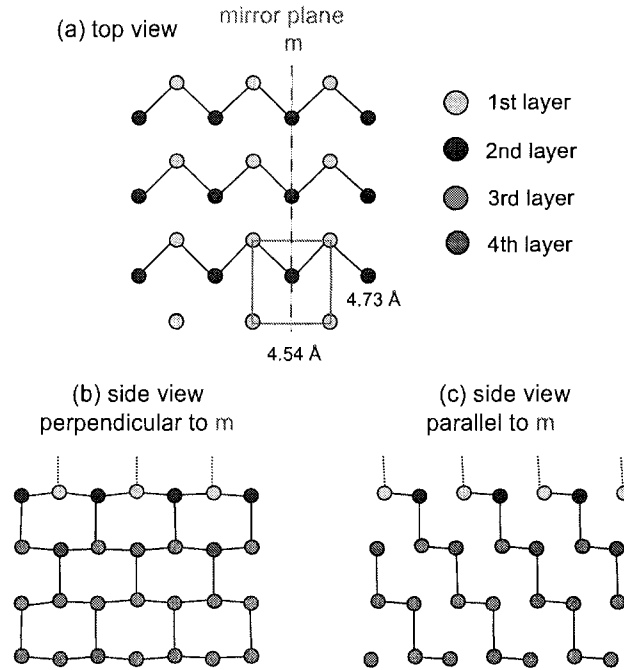
Figure 5-9: Truncated-bulk structure of Bi(110). The solid lines and dotted lines mark covalent bonds and dangling bonds, respectively. (a) Top view of the first two atomic layers. Each layer consists of a two-dimensional rectangular lattice and the lattice constants at 110 K are given. The mirror planes of the structure are also shown as dashed lines. (b) and (c) Side views of the first eight layers perpendicular and parallel to the mirror plane, respectively. The bilayer-like structure with alternating short and long interlayer spacings is evident.

as indicated in Figure 5-9. The lengths of unit vectors at 110 K are taken as 4.731 Å and 4.538 Å; see Refs. [86, 80, 83]. If the rhombohedral structure is treated as a pseudocubic structure as in Ref. [80], Bi(110) will be denoted as Bi(001). The pseudo-square character of the surface unit cell is evident: for a cubic Bi structure all the atoms in the first bilayer would have the same height, the unit cell would be rotated by about 45°, and contains only one atom.

5.3.2 Methods

Experiment

The experiment setup and cleaning procedure are the same as described in Sec. 5.2.2 for the Bi(111) surface. Especially, great care was taken to align the camera with respect to the electron gun and the Bi crystal for this low symmetry surface, as described below.

To obtain intensities of the diffracted beams as a function of electron energy, the following procedure was employed: A series of images was recorded within the energy range from 30 eV to 300 eV, while the energy was increased in steps of 1 eV after every recorded image. The integrated spot intensity of every single diffracted beam (h, k) was extracted from these images. The presence of only one mirror line symmetry for Bi(110) leads to technical challenges for the LEED experiment. These difficulties are illustrated in Figure 5-10 that shows two measured LEED patterns taken at different incident energies. The pseudo-square pattern of the reciprocal lattice and the missing left/right symmetry are clearly evident. The up/down symmetry is given by the mirror plane in the crystal (the horizontal plane in Figure 5-10). It is necessary to align the sample surface perpendicular to the incoming electron beam, and this is usually done by comparing the IV curves of the symmetry-equivalent beams. Here this procedure can only be applied for the up/down angle. In order to align the left/right angle we optimized the diffraction spot position on the LEED screen until they agreed with the kinematically calculated positions.

The alignment procedure is as follows. At a certain incident electron energy, we record the diffraction pattern. Knowing the electron energy, the sample and screen geometries and the lattice constant, we calculate the beams positions on the screen under normal incidence. The sample is aligned until a best overlap is reached between the observed pattern and the
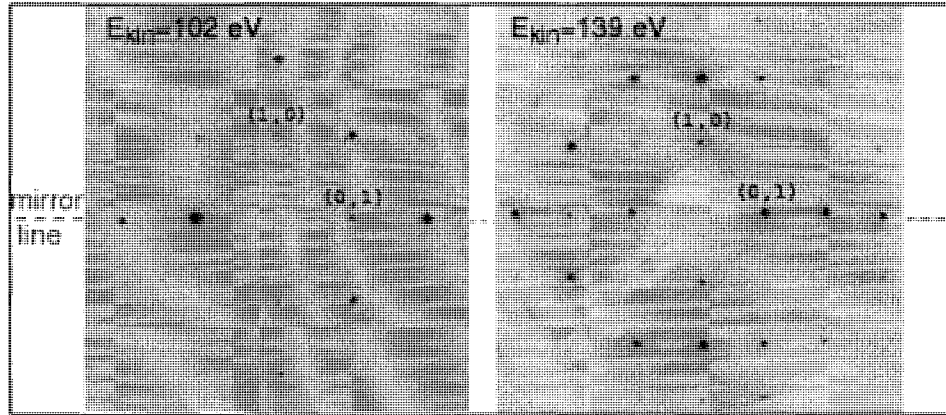
Figure 5-10: LEED patterns at two different electron beam energies for normal incidence on Bi(110) at 110 K. The (1,0) and (0,1) diffraction spots are marked.

calculated pattern. Figure 5-11 shows such a comparison at the energy of 62.2 eV. Some experimental diffraction spots have been saturated for a better visualization of all beams. The small circles are calculated beam spots. It is apparent that most of the spots overlap very well. In this way, we can do adjustments at different energies to guarantee a normal incidence in the entire energy range. We estimate that this approach leads to an error of less than 0.5° in the angle of incidence.

In the final data set, the intensities of the symmetry-equivalent beams are averaged.

Dynamical LEED calculations

The dynamical LEED intensity calculations were performed using the standard package SATLEED (Symmetrized Automated Tensor LEED) by Barbieri and Van Hove [41] within the renormalized forward scattering perturbation formalism. Atomic scattering phase shifts have been calculated using a muffin-tin potential model and the standard Barbieri and Van Hove phase shift package [41]. The bulk diffraction matrices for the closely spaced bilayers were calculated with the combined space method [18]. The same muffin-tin radius
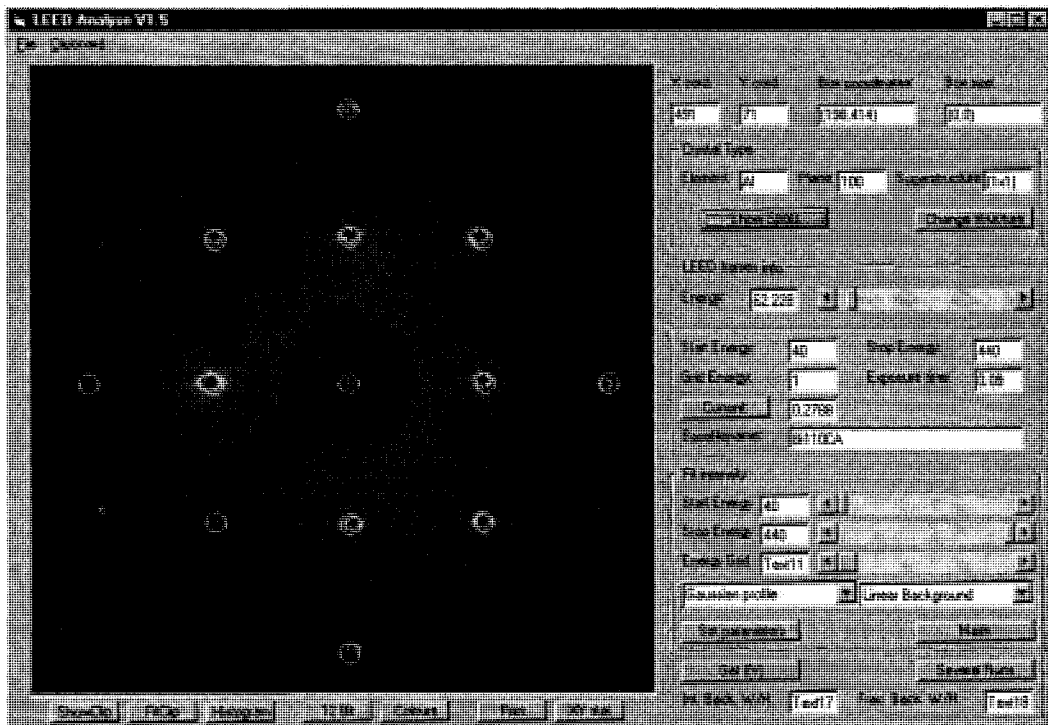
Figure 5-11: Comparison between experimental (bright spots) and kinematically calculated diffraction pattern (green circles) for Bi(110) at 62.2 eV.

(RMT) of 2.87 a.u. and phase shifts have been used as those for Bi(111). Phase shifts have been renormalized by the thermal effects of root-mean-square (rms) isotropic vibrational amplitudes. Up to 15 ($L = 14$) phase shifts are used. The muffin-tin constant V_0 is taken to be energy-independent and is optimized. V_{im}, the imaginary part of the inner potential, also referred to as damping potential or optical potential, is taken as 4 eV for the bulk and 4.2 eV for the first 2 overlayers. The slightly larger value at the surface was chosen to model the presence of dangling bonds, which increases the electron damping. The surface potential step of height V_0 is located half a long bulk interlayer spacing away from the topmost layer nuclei. The bulk Debye temperature is fixed at 119 K [99], while the Debye temperatures for the first 2 layers are optimized. Mean-square atomic vibrational amplitudes $\langle u^2 \rangle_T$ at temperature T for the Debye-Waller factor calculation are derived from Debye temperatures Θ_D according to Equation 5.2.

In the LEED intensity analysis, agreement between experimental and calculated LEED intensities is quantified by the widely used Pendry R factor, R_P, as defined in Equation 2.29. The uncertainties in the optimized structural parameters are estimated based on the Equation 2.30.

Ab initio calculations

Our collaborators [100] performed *ab initio* calculations of the surface crystal structure of Bi(110). The full-potential linearized augmented plane wave method in film-geometry [88, 89] as implemented in the FLEUR-code was used and the local density approximation [90] to the density functional theory was employed. Spin-orbit coupling was included in the self-consistent calculations [91]. The evaluation of the surface relaxation has been carried out for the symmetric 14-layer film, both, with the inclusion of the spin-orbit coupling

(SOC) term and without this term. Force calculations have been performed for the first four layers without spin-orbit coupling while relaxations have been carried out only for the first two interlayer spacings with the inclusion of SOC. In the latter evaluations we kept the interlayer spacings d_{34} and d_{45} equal to those obtained from the force calculation without SOC. The geometry was chosen such that both sides of the film were terminated with an intact bilayer. A wavefunction cutoff of 3.8 a.u.$^{-1}$ was chosen and the Brillouin zone was sampled with 32 k-points.

5.3.3   Results and discussion

LEED structure determination

The LEED pattern of Bi(110) has previously been discussed by Jona [80]. He defined a pseudo-cubic bulk unit cell and concluded that the unit cell (and hence the LEED pattern) should not be exactly rectangular but that the lattice vectors should include an angle slightly different from 90°. Our study does not confirm this conclusion. Our LEED patterns as presented in Figure 5-10 show an exact rectangular net from careful measurements of the diffraction spots positions and, indeed, such an exact rectangle can also be expected from a projection of the bulk reciprocal lattice onto the surface [70]. The measured ratio of the two reciprocal unit cell vectors is 0.96(2) in good agreement with the expected value of 0.959. Moreover, the observed patterns show no indication of any reconstruction of the Bi(110) surface, despite the existence of active dangling bonds at the surface. Apparently, Bi(110) is found to be very different from typical semiconductors surfaces, such as Si(100) and Ge(100) which both exhibit 2×1 reconstructions.

The structural and non-structural parameters were optimized for a Bi(110) surface terminated by an intact bilayer. A termination with a split bilayer was immediately excluded

due to lack of agreement with the experimental *IV* curves shown in Figures 5-12 and 5-13. 20 symmetry in-equivalent beams with a total energy range of 3591 eV have been analyzed to determine the following structural and non-structural parameters: the first four interlayer spacings d_{ij} $(j = i + 1; 1 \leq i \leq 4)$, the real part of the inner potential V_0, and Debye temperatures Θ_{D_1} and Θ_{D_2} for atoms in the first and second layers, respectively. The results of the structural analysis are summarized in Table 5.5. Note that the first and the third interlayer spacings correspond to the small separation (0.21 Å) between the two layers making up the bilayer in the bulk. Their seemingly dramatic relative relaxations are very small in absolute terms. Also, the forth layer appears to move above the third layer by 0.01 Å. However this very small value is clearly below our detection limit. Overall no significant relaxation for the Bi(110) surface is found. We have tried many possible displacement patterns allowed due to the low surface symmetry. However, we found no significant improvement in R_P when changing the relative distance between the two basis atoms in the first and second layers parallel to the mirror line. The Debye temperature for the first layer is found to be lower than that of the bulk, which is consistent with an early study of Goodman and Somorjai [94]. Reduced surface Debye temperatures are a common phenomenon reflecting the weaker bonding of surface atoms compared to the bulk [101]. The actual numerical values of the surface Debye temperature are an important ingredient for the determination of the electron-phonon coupling strength from angle-resolved photoemission data [95, 102, 96, 103]. Meanwhile the second layer shows a Debye temperature close to the bulk value.

The LEED-*IV* analysis gives a relatively high R_P factor of about 0.38 compared to typical values of 0.1 to 0.3 for clean unreconstructed metal surfaces. Many efforts have been made to find out the possible causes of this value. We simulated non-normal incidence

Table 5.5: Optimized parameter values for the surface structure of Bi(110) from LEED and *ab initio* calculations. Interlayer spacings between the ith and jth layer are indicated as d_{ij}. d_{ij}^{b} is the corresponding interlayer spacing of the truncated bulk at 110 K and $\Delta d_{ij} = d_{ij} - d_{ij}^{\mathrm{b}}$. V_0 is the real part of the inner potential. Θ_{D_1} and Θ_{D_2} are the Debye temperatures for the first and second layers, respectively.

Parameters	Experimental results by LEED			*ab initio* calculations
	Starting values	Optimized values	$\Delta d_{ij}/d_{ij}^{\mathrm{b}}$ (%)	$\Delta d_{ij}/d_{ij}^{\mathrm{b}}$ (%)
d_{12} (Å)	0.208	0.18 ± 0.048	-13 ± 23	-62
d_{23} (Å)	3.064	3.06 ± 0.043	-0.2 ± 1.4	$+0.3$
d_{34} (Å)	0.208	0.01 ± 0.040	-105 ± 19	-105
d_{45} (Å)	3.064	3.20 ± 0.046	$+4.3 \pm 1.5$	$+4.4$
V_0 (eV)	8.0	3.5 ± 1.50	$-$	$-$
Θ_{D_1} (K)	119	95^{+60}_{-25}	$-$	$-$
Θ_{D_2} (K)	119	116^{+80}_{-40}	$-$	$-$
R_P	$-$	0.38	$-$	$-$

conditions extensively in the LEED-*IV* calculations and found that an increase in the incident angle gave a dramatic rise in the R factor from its minimum at zero or normal incidence. This suggests that the sample is properly aligned and the relatively high value is not caused by deviations from normal incidence during the *IV* measurement. The influence of the muffin-tin radius on the structure has been studied and results show essentially the same geometry with a minimum R factor at the muffin-tin radius of 2.87 a.u.. We also tried the atomic potential derived from our *ab initio* calculations with no significance changes in the optimized structural parameters nor an improvement in the R factor. So it might be the structural complexity and low symmetry of the Bi(110) surface itself that complicates the LEED process. As seen on open semiconductor surfaces the presence of dangling bonds and the presence of voids in the open surface structure is a real challenge for the muffin-tin approximation of the crystal potential and could also contribute to the relatively high R_P for this surface. However, the low surface symmetry of Bi(110) gives rise to the large number of non-equivalent beams. Here we present an accumulative energy range of 3591 eV (20 beams) which is far broader than a typical one of about 1000 eV used in LEED studies. When an overall range of only 1071 eV (the first 6 beams) was analyzed in our work, the R factor decreased to 0.23 without changes in the optimized structural parameters. This value is comparable to LEED results for many semiconductors and metal oxide compounds with similar geometric and electronic structures. Interestingly, the reduction of R factor due to fewer beams indicates more intricate scatterings in the higher ordered beams. Furthermore, with horizontal surface atomic displacement in the mirror-plane allowed, a smaller R has been obtained but, considering that the displacement values are within error limit and no significant geometry change occurred, we are not including these displacements in the report. The agreement between this large experimental data set and the calculated intensity-energy

81

curves, as shown in Figures 5-12 and 5-13, give us confidence in the reliability of our results.

The error bars of the optimized parameters were analyzed based on the variation of the R factor around $R_{P\,\text{min}}$, $\Delta R_P = 0.036$ according to Equation 2.30. The dependence of R_P on a change of the interlayer spacings away from their optimized values is shown in the Figure 5-14. In this analysis, all other parameters were fixed at their optimized values. We can see that all the sensitivity curves take on a parabolic shape. The errors for the individual parameters are also listed in Table 5.5.

Comparison to first-principles calculations

The first-principle calculations performed for bulk Bi without the inclusion of spin-orbit interaction give bulk short and long interlayer spacings of 0.142 Å and 3.087 Å, respectively. Evaluations that include the SOC term lead to a very slight modification of approximately 0.01 Å of these results. As shown in Table 5.5, our scalar relativistic force calculations give the following values for the first 4 interlayer spacing relaxations at 0 K: $\Delta d_{12}/d_{12}^{\text{b}} = -62\%$, $\Delta d_{23}/d_{23}^{\text{b}} = +0.3\%$, $\Delta d_{34}/d_{34}^{\text{b}} = -105\%$, and $\Delta d_{45}/d_{45}^{\text{b}} = +4.4\%$. These results agree reasonably well with those obtained by the LEED-IV analysis at 110 K considering the fact that the absolute distance difference between the experimental and calculated first interlayer relaxations of -13% and -62% is only 0.06 Å. Both the experiment and theory lead to the contraction of the first interlayer spacing. For the second interlayer spacing the theory gives a small expansion while the experiment shows a small contraction of the spacing. However the theoretical result is within the experimental error bar. The absolute distance difference between the experimental and calculated second interlayer relaxations of 0.015 Å is even smaller than that for the first interlayer spacing. For the third and fourth interlayer spacings the theory and experiment are in excellent agreement. The first-principle calculations that
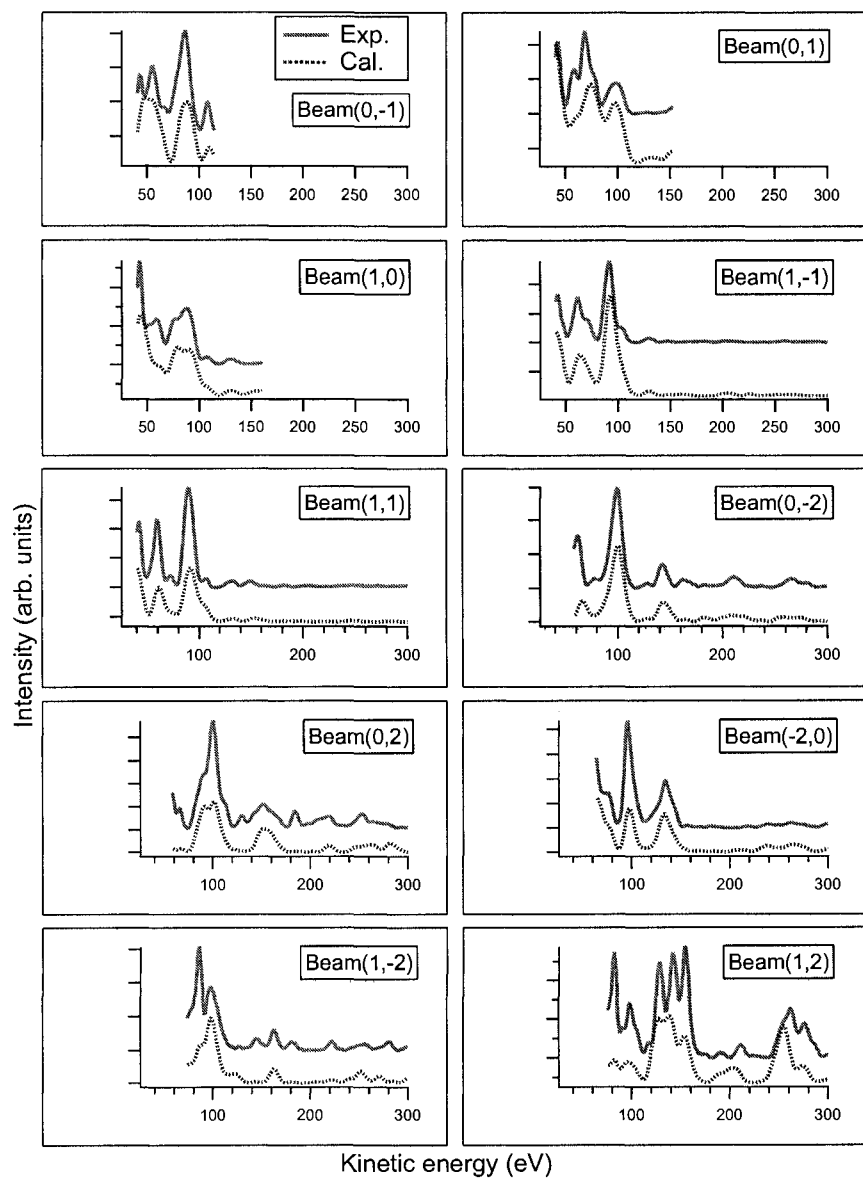
Figure 5-12: Comparison of 20 experimental and calculated *IV* curves for normal incidence on Bi(110) at 110 K. Solid lines show experimental data and dotted lines show calculated data which are shifted downward for comparison. To be continued in Figure 5-13.
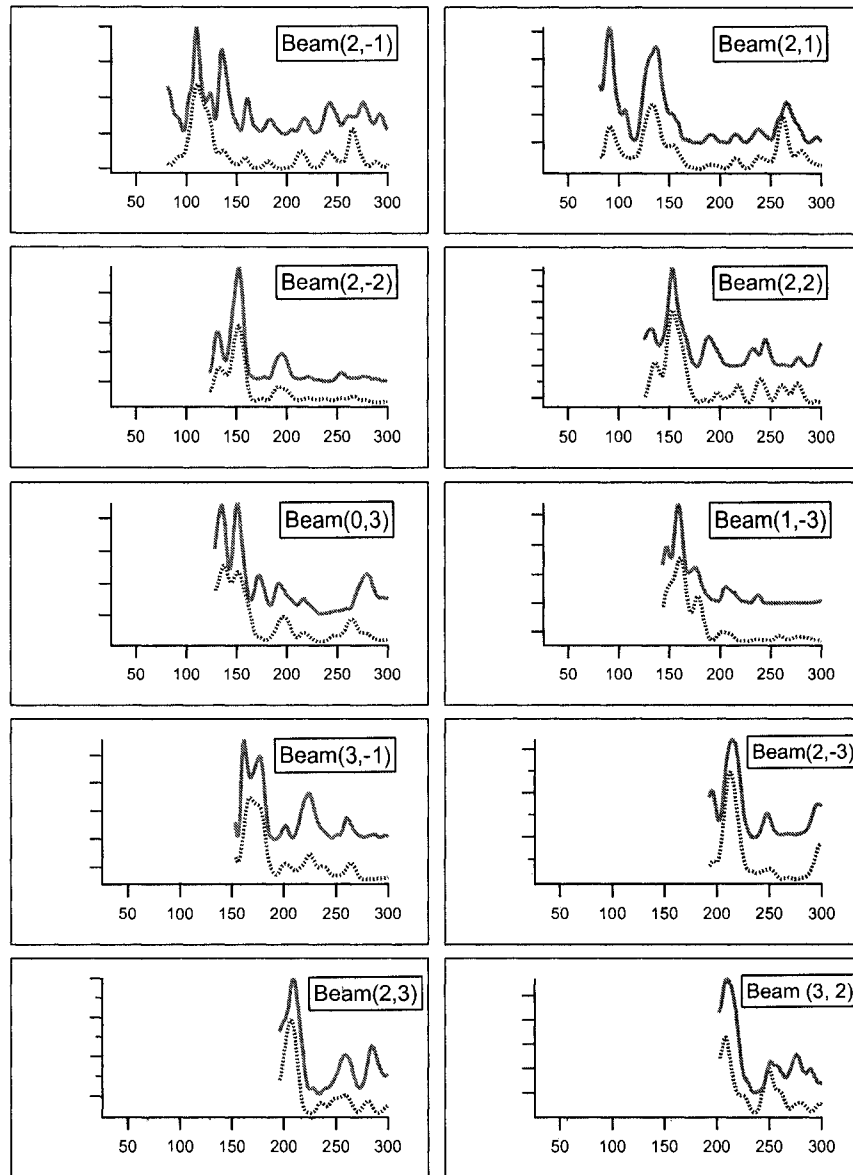
Figure 5-13: Continuation of Figure 5-12.
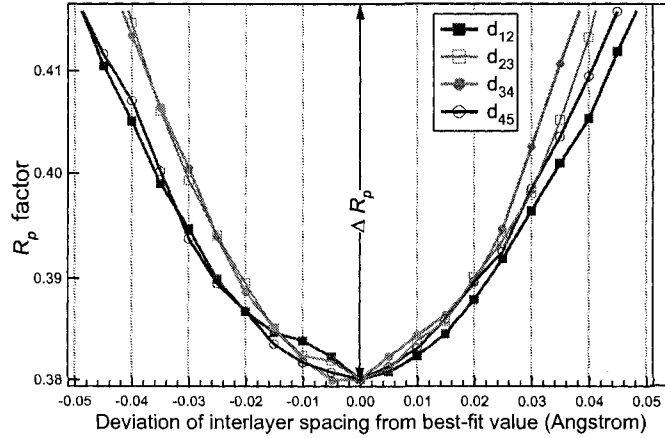
Figure 5-14: Error bar determination for the first 4 interlayer spacings based on $\Delta R_P = 0.036$ and Equation 2.30.

include the spin-orbit interaction term lead to $\Delta d_{12}/d_{12}^{b} = -43\%$ and $\Delta d_{23}/d_{23}^{b} = +0.4\%$ for the first and second interlayer spacings respectively. These values have been obtained by keeping the interlayer spacings $\Delta d_{34}/d_{34}^{b}$ and $\Delta d_{45}/d_{45}^{b}$ equal to those found in the scalar relativistic calculations. This shows that the influence of spin-orbit interaction on the relaxation is small and probably will not change the values of d_{34} and d_{45} significantly. Notice, that in the relaxed geometry a change of 6% or 0.01 Å in $\Delta d_{12}/d_{12}$ corresponds to an energy change of only 0.5 meV per surface atom which is certainly at the limit of our accuracy.

In our force calculations, we also optimized the position of the surface atoms in a plane parallel to the surface. By symmetry, this movement is then confined to the mirror plane shown in Figure 5-9 (a). We notice, that these relaxations are small and do not exceed 1.0% in the top four layers, consistent with the experimental findings.

85

5.3.4 Conclusions

Our results give a consistent picture of the very low-symmetry surface geometric structure of Bi(110) by LEED intensity analysis and first-principles calculations. Good agreement is reached between experimental LEED and theoretical *IV* curves. No structural reconstruction occurs despite the dangling bonds present at the surface. No significant absolute value of relaxation is found for the first 4 interlayer spacings. The reduced top-layer Debye temperature suggests essentially larger vibrational atomic amplitudes at the surface. Experimentally, the approach of sample alignment by calculating the diffraction spot positions on the LEED screen is very efficient and can be used for surfaces with low symmetry as well as for *in-situ* cleaved surfaces.

5.4 The Bi(001) surface

The Bi(001) surface is also found to be a better metal than the bulk. In contrast to the relatively localized surface states on Bi(110) and Bi(111), however, the surface states on Bi(001) penetrate very deeply into the bulk. It has been suggested that this could explain some apparent contradictions found for the electronic structures of clusters, nanowire and nanotubes [67].

So far there are very few publications on the Bi(001) surface. As far as we know, no quantitative atomic surface structure is available. This section presents surface geometric results by STM and LEED.

5.4.1 The bulk-truncated Bi(001) surface structure

The top view and side view of Bi(001) are depicted in Figure 5-15. The crystal can be viewed as built from quasi-hexagonal layers of Bi(001). In each layer an atom has two

neighbors at the same distance as on the Bi(111) surface (4.54 Å) and four next-nearest neighbors at a slightly larger distance (4.72 Å) [70]. The three nearest neighbors of any Bi atom in the bulk structure, however, do not lie in the same quasi-hexagonal layer but they connect these layers. The connections to the nearest neighbors are indicated as "bonds" in Figure 5-15. The side view shows that there are two different possible interlayer spacings. The termination of the surface is not known, but it seems likely that the shorter interlayer spacing prevails, not least because it requires only the breaking of one covalent bond per unit cell instead of two. The broken bonds at the surface are also indicated as dashed lines in Figure 5-15. It can be seen that the structure is close to an ABCABC. . . stacking sequence of the quasi-hexagonal layers, except that the fourth layer atoms are not quite in registry with the first layer atoms. They are actually shifted by a distance of 0.57 Å. The registries of the stacking layers from the surface to the bulk are in the following way: in the direction from one atom to its nearest neighbors (vertical direction in Figure 5-15 (a)), the atom position shifts by half 4.54 Å from one layer to the next, and in its perpendicular direction, atom shifts by an alternating distance of 5.953 and 5.241 Å. The symmetry of the surface is very low. The only symmetry element is a mirror plane which is also indicated in Figure 5-15 (a), in contrast to a higher symmetry of a threefold axis and three mirror planes in Bi(111). Consequently there are some important differences between Bi(001) and Bi(111): in order to form Bi(111) no covalent next-neighbor bonds have to be broken while one bond per unit cell has to be broken to form Bi(001).

The LEED pattern for the surface was found to be (1×1) [80, 67] but no quantitative LEED study has yet been performed. The energy-minimized geometric structure has been calculated for this surface by first-principles [100]. The first interlayer distance d_{12} contracts by $\Delta d_{12}/d_{12}^b = -3.0\%$, and the second interlayer spacing d_{23} expands by $\Delta d_{23}/d_{23}^b = +14\%$.

(a) Top view

mirror plane

4.72 Å

○ 1st layer
● 2nd layer
◉ 3rd layer
◕ 4th layer

(b) Side view (parallel to mirror plane)

1.74 Å
1.98 Å
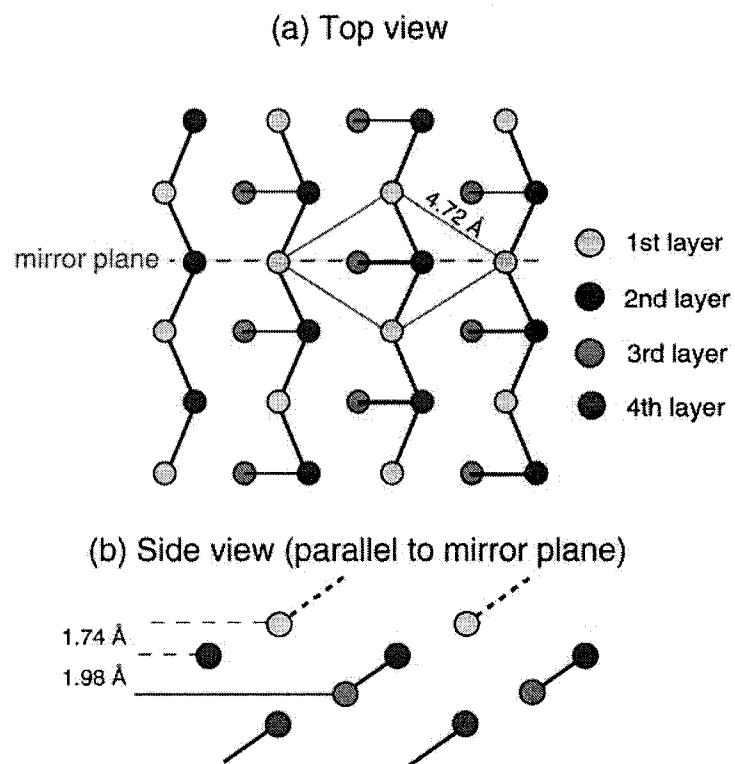
Figure 5-15: Truncated-bulk structure of Bi(001). The dark solid lines indicate covalent bonds between the atoms within the bilayers. (a) The top view of the first four atomic layers. The single mirror plane of the structure is shown as a dashed line. (b) The side view of the first four layers parallel to the mirror plane. Dashed lines on the first layer atoms indicate dangling bonds.

Similar to Bi(110), Bi(001) has another feature with respect to its symmetry. It would be possible to shift atoms of Bi(001) along the mirror line without breaking the translational symmetry parallel to the surface, retaining a (1×1) LEED pattern. Such displacements have been considered in the first-principles calculations but they have been found to be very small (below 0.1 Å) [100].

5.4.2 Surface morphology observation by STM

The surface atomic morphology is imaged with the commercial scanning tunneling microscopy STM 150 Aarhus (SPECS ®). The key STM components are schematically shown in Figure 5-16 [6]. The sample holder is held onto the sample stage by two clamps and they, as a whole, are electronically and thermally insulated from the STM cage by three quartz balls. The tip facing up to a sample is connected to the scanner tube and in turn to the approach motors. A Zener diode is used to adjust the experimental temperature by heating during cooling. A heavy metal block, containing the STM cage and supporting the sample holder, is hung by springs, which allows for an excellent vibration-isolation for the STM system. Peripherally, two ion sputtering guns are installed: one is for the sample cleaning and the other for the *in-situ* tip sputtering. For tunneling, the tip moves upward to the sample by automatically controlled piezo-electronic motors. The motion stops upon the detection of a tunneling current. The well documented details of this facility is referred to in Ref. [104].

To clean the Bi(001) surface, cycles of argon ion sputtering and annealing are carried out to remove surface contaminants and smooth the surface. Argon ions are accelerated with a voltage of 500 V at an ambient gas pressure of about 5×10^{-6} mbar for about 20 min and followed by about 45 min annealing at 120°C. All the STM images are taken at room

1 Sample
2 Sample holder
3 Clamps
4 Tip
5 Tip holder
6 Scanner tube
7 Approach motor rod
8 Motor mount
9 Approach motor
10 Quartz balls
11 Zener diode
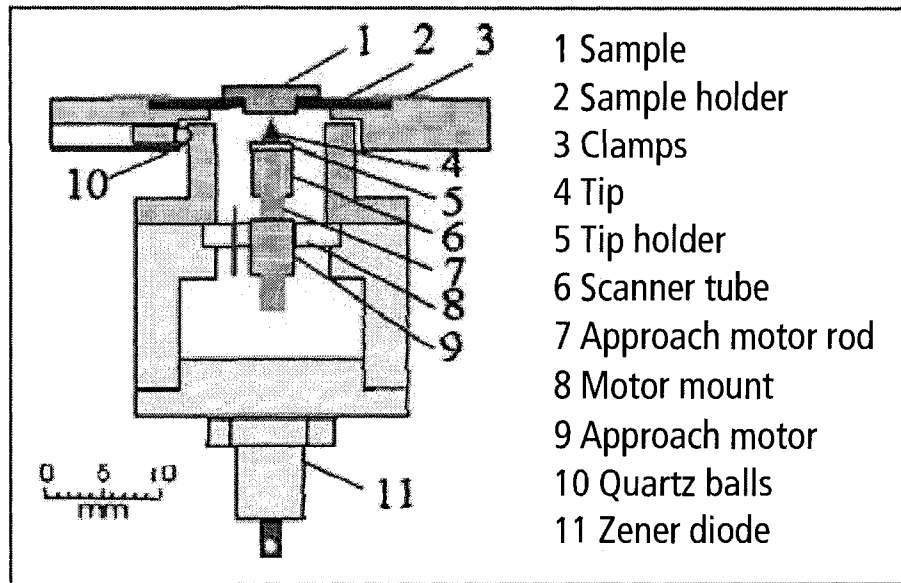
Figure 5-16: Schematics of the STM 150 Aarhus [6]. The sample is placed in a sample holder held down on the STM top by clamps. The top plate is thermally and electrically insulated from the STM body by three quartz balls. The tip is held by a macor holder glued to the top of the scanner tube. The scanner tube is glued to the rod which together with a segmented piezo tube forms a small motor used for coarse approach. The Zener diode is used to counterheat the STM body during cooling.

temperature and a UHV pressure of 1×10^{-10} mbar. All the measurements are calibrated with the known Au(788) surface step height and terrace width.

An atomic picture in Figure 5-17 (a) shows the Bi(001) lattice structure. The image size is 50×50 Å^2. Tunneling current $I_t = 0.260$ nA and tunneling voltage $I_V = 173.6$ mV. The lighter spots indicate protruding atoms. The small parallelogram is plotted to show the primitive unit cell. It agrees with the quasi-hexagonal surface lattice on Bi(001). A line scan across 11 atoms (10 interatomic spacings) is indicated in the upper panel (a). The atomic corrugation along this line is shown in the lower panel (b).

To get the surface morphology at a larger scale, larger areas are scanned. Figure 5-18 (a) shows a typical surface region (1000×1000 Å^2, $I_t = 0.190$ nA, and $I_V = 1250.0$ mV). Big terraces are seen with the width ranging from 100 to 700 Å which are longer than the electron coherence length. The steps edges are shown by the abrupt change in the contrast variation. A line scan across four steps and an interesting "hump" is shown in panel (a). The corresponding height along the line is plotted in the panel (b). We get a step height of about 3.68 Å which is close to the double layer height of 3.72 Å in the Bi(001) bulk. Therefore, only double layer step height exists on the surface. This indicates that all the terraces are geometrically equivalent and are felt the same by the incident electrons. In other words, the surface is a single domain with incoherent terraces. This surface morphology is confirmed by the LEED results in the next section. Meanwhile, one question arises naturally: is it a short or long termination on the surface? It is not easy to observe because of the sharp step edge of double layers. But it is possible to see the first interlayer spacing by removing parts of the first layer near the step with some delicate experimental procedures. This work is under progress.

One more interesting phenomenon spotted in the Figure 5-18 (a) is a "hump" nanostruc-

ture near the mark "B". It is believed to be a twin crystal similar to the twin microlayers observed by Edelman *et al.* [85] at the Bi(111) surface. Figure 5-18 (b) gives the hump height of about 1.97 Å. More studies can be done to find out how this structure forms and its surface effects.

5.4.3 Surface structure determination by LEED

The LEED experiment is performed on the LEED facility at the University of Aarhus. The LEED setup is shown in Figure 2-7. A base pressure of $\sim 10^{-11}$ torr in the chamber is obtained. The sample is loaded from the top window of the chamber. The cleaning procedure is the same as that used in STM study. The cleanliness of the surface is monitored by AES. No surface contamination is detected. The sample is aligned to get a normal incidence by matching the kinematically calculated pattern with the experimental pattern.

A series of LEED-*IV* spectra are recorded with a CCD camera for different temperatures of -160, -110, -78, -38, and 11 °C. The sample cooling is realized via a liquid nitrogen flow. The temperature can be controlled to $\pm 3°$C within 20 min. Figure 5-19 and 5-20 show the difference in some beam intensities at different temperatures. We can see for each beam, the temperature has a minor influence on the diffraction peaks but reduces the intensity as the temperature goes up. It is not surprising when considering the stronger electron wave damping due to the stronger atomic vibrations at a higher temperature.

A quantitative analysis of the experimental spectra for the sample temperature of -160°C is performed with the standard package of ATLMLEED by Barbieri and Van Hove [41]. The package is able to handle multiple angles of incidence and/or multiple surface structures coexisting on the surface. We use this package for the possibility of multiple domains present on the surface. Our results show that the short termination structure generates a best-fit
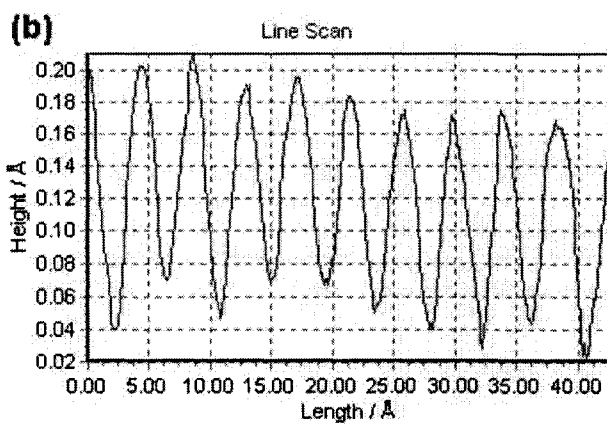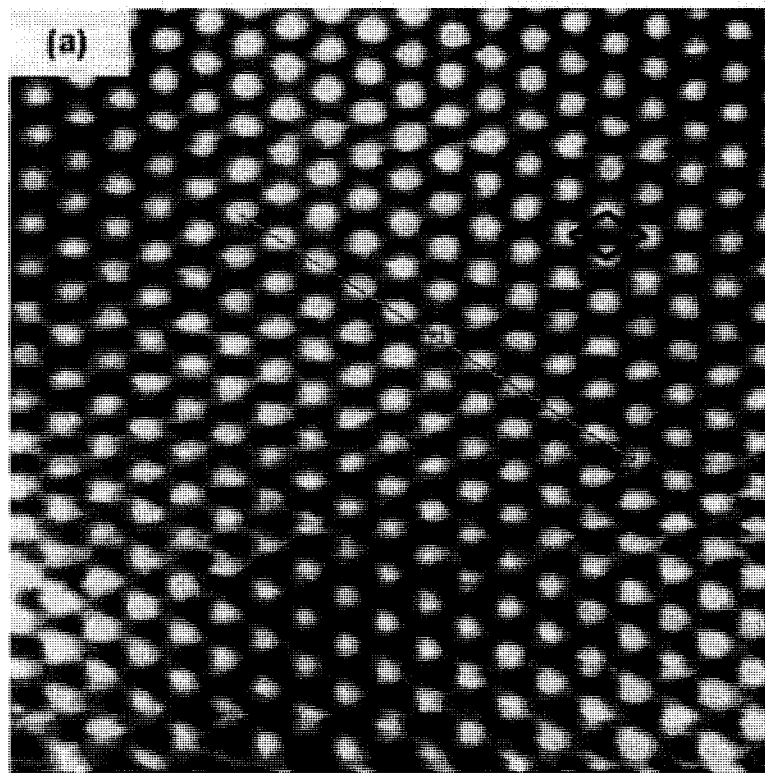
Figure 5-17: An atomically resolved STM image of the Bi(001) surface. (a) Size: 50×50 Å^2. Tunneling current: $I_t = 0.260$ nA. Tunneling voltage: $I_V = 173.6$ mV. The parallelogram indicates the primitive unit cell. (b) The atomic corrugation along the scanning line in (a).
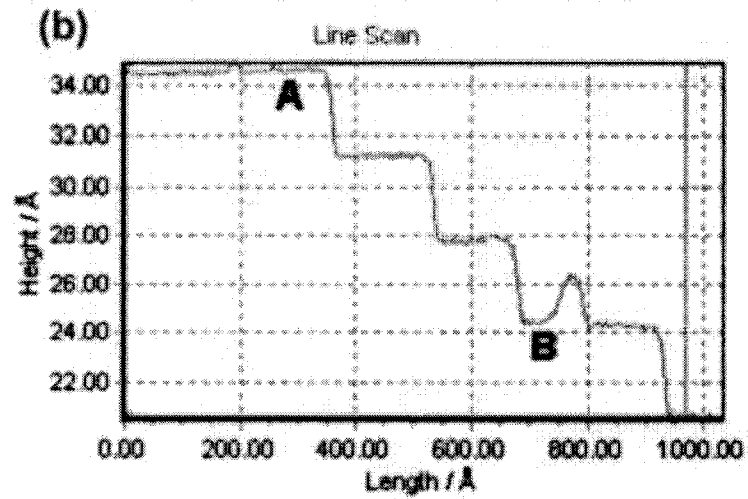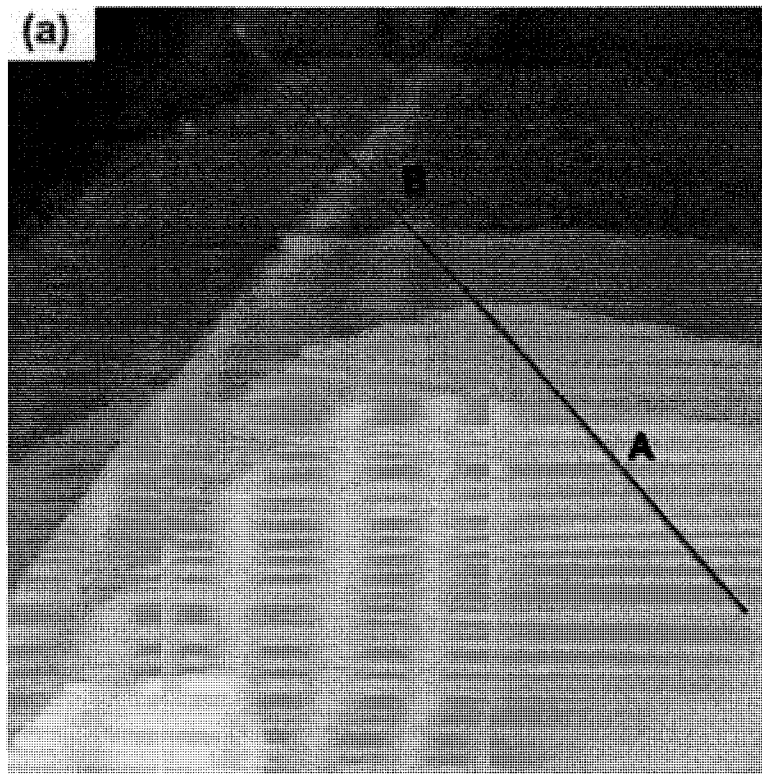
Figure 5-18: Bi(001) surface morphology by STM. (a) Picture size: 1000×1000 Å^2. Tunneling current: $I_t = 0.190$ nA. Tunneling voltage: $I_V = 1250.0$ mV. The scanning line across steps is indicated. The corresponding step heights and the "hump" height are shown in (b).
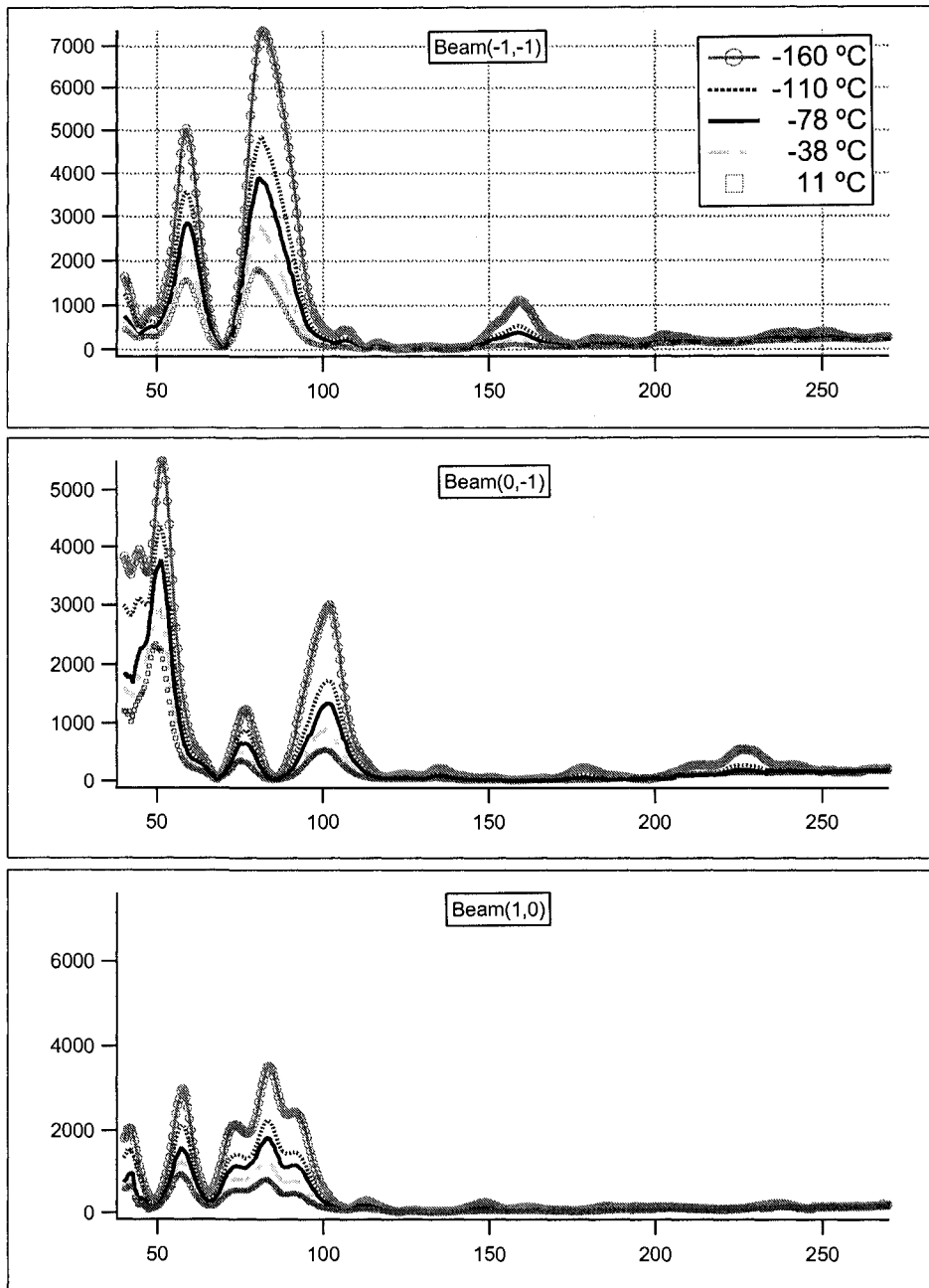
Figure 5-19: Diffraction intensities vs the sample temperature. To be continued.
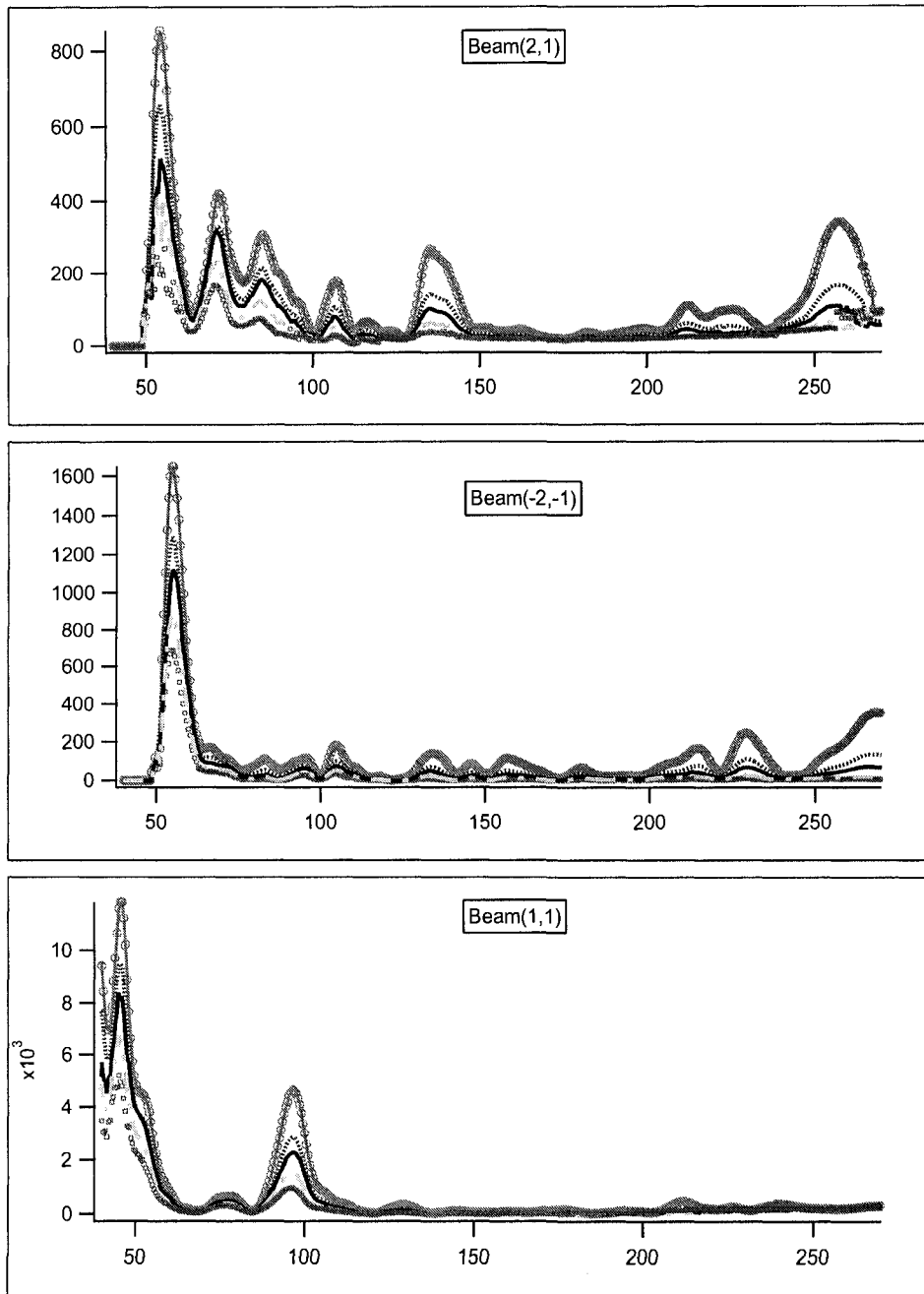
Figure 5-20: Continuation of Figure 5-19.

between experimental and calculated data. Other possible models have been tried but they gave a worse level of agreement. They include the long spacing termination and coexistence of two possible domains. So far, we have only optimized structural parameters and the optimum interlayer spacings are listed in Table 5.6. The first and third interlayers contract by -5.5% and -7.7%, respectively. The second and the fourth interlayers expand by +11.0% and +3.4%. The interlayer relaxations obtained by *ab initio* calculations are also given in this table; they show a good agreement with the LEED results. One more parameter optimized is the atomic displacement along the mirror plane. We get displacements of 0.259, 0.172, 0.101 and -0.010 Å for the atoms in the first four layers, respectively. The sensitivity of the R factor to these displacements and the optimization of non-structural parameters are to be studied. The comparison between experimental and calculated IVs is shown in Figure 5-21, and almost all of the peaks' positions match and it shows an overall good agreement. The R_p factor of 0.34 for the agreement between the experimental and calculated IV curves is still a bit high. It is understandable when considering the low symmetry of the Bi(001) system and the complexity of the structure itself. It, however, can be improved when other parameters are optimized. The calculated IV curves for the long termination structure are also shown in Figure 5-21 and the fit is much worse with a R factor is 0.61. So the long termination surface can be ruled out.

5.4.4 Summary and outlook

To summarize, the STM observation shows wide terraces separated with double layers steps resulting in a single domain on the Bi(001) terrace. LEED simulations confirm the existence of a single domain with the short termination. Interlayer spacings obtained by LEED agree well with those by the *ab initio* calculations. In STM, we try peeling off the first layer in
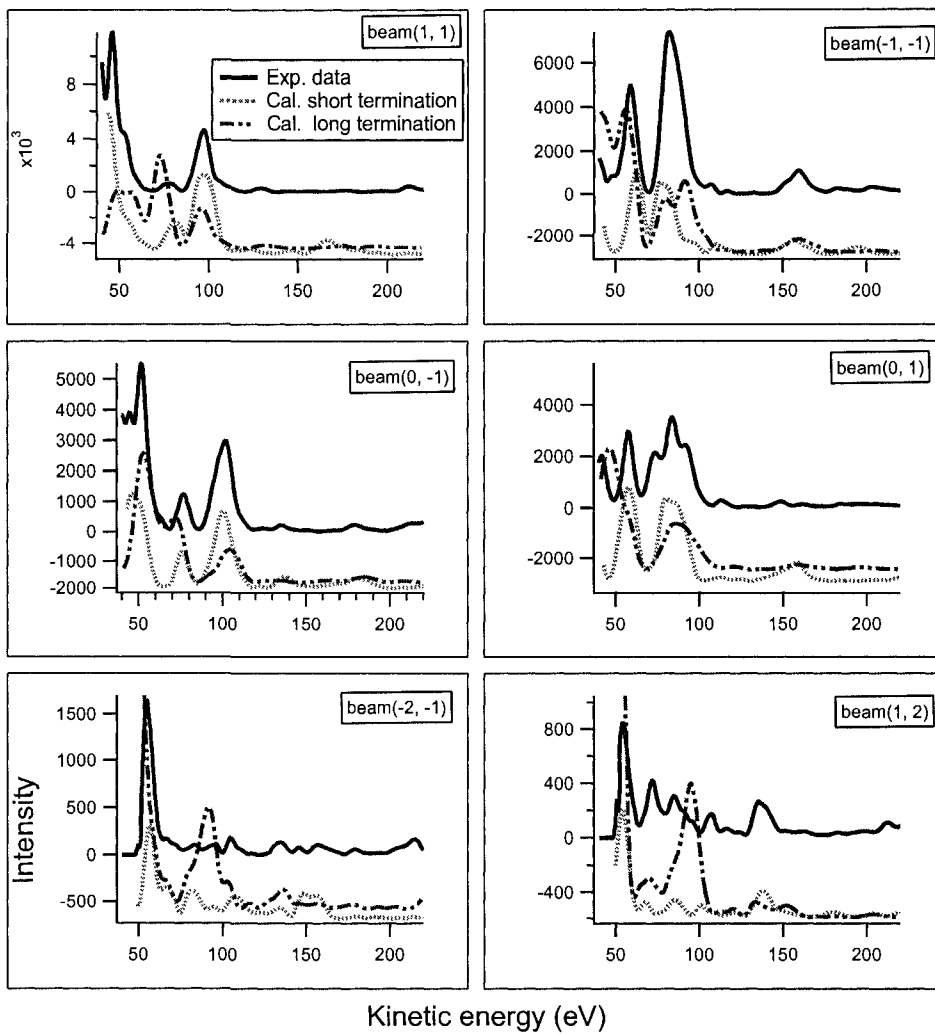
Figure 5-21: Comparison between experimental (solid) and two sets of calculated *IV* curves for Bi(001) at -160°C: short termination (dotted) and long termination (dash-dotted) structures. Vertical shifts of the calculated data are just for a better visual comparison.

Table 5.6: *Optimized parameter values for the surface structure of Bi(001) from LEED and ab initio calculations. Interlayer spacings between the ith and jth layer are indicated as d_{ij}. d_{ij}^{b} is the corresponding interlayer spacing of the truncated bulk at -160°C and $\Delta d_{ij} = d_{ij} - d_{ij}^{b}$. V_0 is the real part of the inner potential.*

| Parameters | Experimental results by LEED | | | ab initio calculations |
	Starting values	Optimized values	$\Delta d_{ij}/d_{ij}^{b}$ (%)	$\Delta d_{ij}/d_{ij}^{b}$ (%)
d_{12} (Å)	1.744	1.648	-5.5	-3.0
d_{23} (Å)	1.981	2.199	+11.0	+14.0
d_{34} (Å)	1.744	1.609	-7.7	—
d_{45} (Å)	1.981	2.054	+3.4	—
V_0 (eV)	4.0	1.8	—	—
R_P	—	0.34	—	—

order to measure the first interlayer distance directly. Optimization of a complete set of parameters in LEED is in progress.

CHAPTER 6

PdCu surface alloy on Cu(001)

6.1 Introduction

6.1.1 Surface alloys

A phenomenon that has been fully recognized recently and spurred much interest is the surface alloy formation – an intermixing of bulk surface atoms with foreign adatoms in the outermost layer or in a few outermost layers resulting in a stable ultra-thin alloy films on a substrate [105, 106, 107]. Surface alloys even form between elements which are immiscible in the bulk such as Na and K deposited on Al(111) and (001), Au on Ni(110), Ag on Pt(111), and Sb on Ag(111) [108, 109, 110, 111, 112]. Apart from the compositional change, the ultrathin metal-on-metal films could adopt unusual alloy structures with no bulk analogue. They tend to have different physical and chemical properties from its constituent elements. The available experimental data about the structure of bimetallic surface alloys was reviewed by Bardi [106]. Different topics on recent surface studies were compiled in a book volume [107]. Quite complex alloying, ordering and segregation behaviors may be observed as a function of surface stoichiometry. Pratically, the most relevant technical applications of surface alloys are heterogeneous catalysis, where a large number of catalysis are multimetallic and synergistic effects due to the atomic-level interaction of multiple active metal species at the surface are believed to be significant [105]. Bimetal-

lic surface chemistry plays a crucial role in other technologically important areas such as magneto-optical films, microelectronics fabrication, electrochemistry, corrosion passivation, and structural materials. Well-defined bimetallic surfaces have offered for the first time an ability to correlate surface chemical reactivity with atomic-scale surface structure. Such structure/function relationships must ultimately form the basis for any predictive ability in tailor-making bimetallic surfaces with desirable reactive properties. Understanding the electronic, magnetic, and catalytic properties of these "surface alloys" remains a major challenge in surface physics. One reason for this is that many surface alloy phases are metastable, with the equilibrium phase being a dilute random bulk alloy. Metastability can make it difficult to create reproducible, homogeneous alloy films. Additionally, many surface alloys are structurally inhomogeneous at the nanometer scale. In order to understand quantitatively how film properties are related to structure and ultimately to atomic bonding, structural and compositional heterogeneity must be characterized. Despite much development of techniques sensitive to the composition and structure of the topmost few atomic layers has contributed to the rapid increase in knowledge about the properties of multi-metallic surfaces, it is highly demanded for a technique to fulfill the heterogeneity measurement with high temporal and spatial resolution.

Here we describe in detail a novel quantitative analysis of electron diffraction that allows us to determine the local 3D composition and structure of an alloy surface with nanometer-scale spatial resolution. In traditional low-energy electron diffraction (LEED) experiments, diffraction patterns are acquired from a large illuminated area. Quantitative analysis of the diffracted intensity versus electron energy (LEED-IV) can be used to determine the average composition and structure. We perform quantitative LEED-IV analysis on a LEEM image which allows us to quantitatively determine the alloy film composition and structure with

8.5 nm lateral spatial resolution. Specifically, we use LEED-*IV* to analyze specularly-reflected electrons that are incident normal to the surface. From the energy-dependence of their reflectivity we determine local alloy composition and structure.

6.1.2 PdCu surface alloy on Cu(001)

We have applied our technique to the well-known Pd/Cu(001) surface alloy system, one of the most studied metal-on-metal growth systems. In the last two decades, the PdCu surface alloy on a Cu(001) substrate has been extensively studied due to its scientific and practical significance. This system possesses novel properties including material selectivity [113], catalytic effect [114], eletromigration damage resistance [115, 116], and structural stability [117]. The PdCu surface alloy undergoes temperature-dependent phase transitions. When sub-monolayer coverages of Pd are deposited onto a Cu(001) surface held at temperatures below 173 K, the Pd atoms remain on the surface with a 1×1 periodicity [117]. However, if the temperature is raised to room temperature, the Pd atoms exchange with Cu atoms in the first layer, forming a $c(2 \times 2)$ checker-board layer. This *overlayer* alloy phase has been widely studied both experimentally [118, 119, 120, 121, 122, 123, 124, 125, 126, 127] and theoretically [128, 129, 123, 125, 130, 131, 132, 133, 134]. Other examples which also exhibit the $c(2\times2)$ top layer alloy are Au on Cu(100) [135, 136, 137, 138, 139], Cu on W(100) [140], Mn on Cu(100) [141, 142], Mn on Ni(100) [143, 142], Mn on Pd(100) [144], Na on Al(100) [145], Ag on W(100) [146], Au on W(100) [146], Cu on Mo(100) [147], Ag on Mo(100) [147], and Zr on Pt(100) [148]. In a very early study, Smith *et al.* [118] observed $c(2 \times 2)$ low energy electron diffraction (LEED) patterns during adsorption of Pd onto a Cu(001) substrate. Subsequently, Graham [119] suggested the formation of a surface alloy in qualitative LEED and angle-resolved ultraviolet photoelectron spectroscopy (ARPES) stud-

ies. This speculation was later confirmed by Franco Jona's group [120, 149]. By performing quantitative LEED analysis, they experimentally resolved a well-ordered $c(2 \times 2)$ toplayer surface alloy structure at room temperature and ruled out a $c(2 \times 2)$ overlayer of only Pd atoms. The $c(2 \times 2)$ overlayer sttucture was observed by Murray et al. with STM [150, 124]. The vibrational mode of the $c(2 \times 2)$ surface alloy was studied by Hannon [125] by using electron-energy loss spectroscopy (EELS). Their results support a favorable NN bonding model between Pd and Cu atoms. Theoretically, first-principles electronic structure calculations by Kudrnovský et al. [128] successfully predicted the formation of this overlayer alloy. Molecular dynamics simulations by Black et al. [129] also supported this model. Studies with embedded atom method (EAM) [123, 130] and Bozzolo-Ferrante-Smith (BFS) method[131] further justified the overlayer alloying structure. Among the considerable investigations on this system, much work have been devoted to determining if an amount of Pd is incorporated in the underlayer. Interestingly, EAM simulations by Pope et al. [123] suggested a more favorable overlayer alloy than the underlay alloy and ab initio calculations by AlShamaileh et al. [151] showed no preference for an underlayer versus overlayer alloy. But from a thermodynamical point of view, a Cu-rich overlayer is favorable due to the its lower surface energy (1.85 Jm^{-2}) than Pd (2.05 Jm^{-2}) [152], and the underlayer coordination provides more favorable PdCu NN bonds. This gives rise to the question whether the overlayer alloy is thermally metastable.

As observed in many annealing property experiments, an intriguing transition takes place from *overlayer* alloy to *underlayer* alloy. This phase change was first observed by Graham et al. [153] through low energy ion scattering spectroscopy (LEISS) which implies a nearly pure Cu outermost layer upon annealing at 440 K. In a subsequent study using positron-annihilation-induced Auger spectroscopy (PAES), Koymen et al. [117] found a fast

transition within a couple of minutes at 423 K. Later work by Anderson *et al.* [154] reported this phenomenon at a sample temperature of 353 K by using Auger electron spectroscopy (AES), Rutherford backscattering (RBS) spectroscopy, LEED, work function measurements and the desorption of probe molecules (CO), where a complete transition took about 1 hr due to the lower temperature applied. With an annealing temperature of 550 K, Barnes *et al.* [2] observed an irreversible phase transition from surface layer alloy to the second layer alloy. They also examined the geometry of the annealed structure by using quantitative LEED analyses and derived the activation energy of 1.13 eV for Pd site switching from the outermost layer to subsurface (second layer). This value is bigger than the activation energy of 0.88 eV [122] for Pd alloying into the top layer at Cu(001) surface, but it is smaller than the bulk alloy interdiffusion energy of 2.1 eV [155]. One implication of this overlayer-underlay transition is that configurations with more nearest-neighbor (NN) Pd-Cu bonds are preferable. The stability of the sub-surface alloy compared to the first layer alloy was supported by calculation of vibrational properties of this alloy [156, 133], first-principles calculations [128], and empirical modeling [125].

The sequence of temperature-dependent surface phases described above is shown schematically in Figure 6-1.

6.1.3 Formation of surface alloy

Surface diffusion is an important process in film and crystal growth, chemical reaction, heterogeneous catalysis and semiconductor industry [157]. The process involves the motion of adatoms, clusters, vacancies and other microscopic surface structures. To obtain the knowledge of diffusion kinetics and mechanism is the main objective in surface alloy formation study. Diffusion rate is dictated by many factors such as diffusion potential barrier,
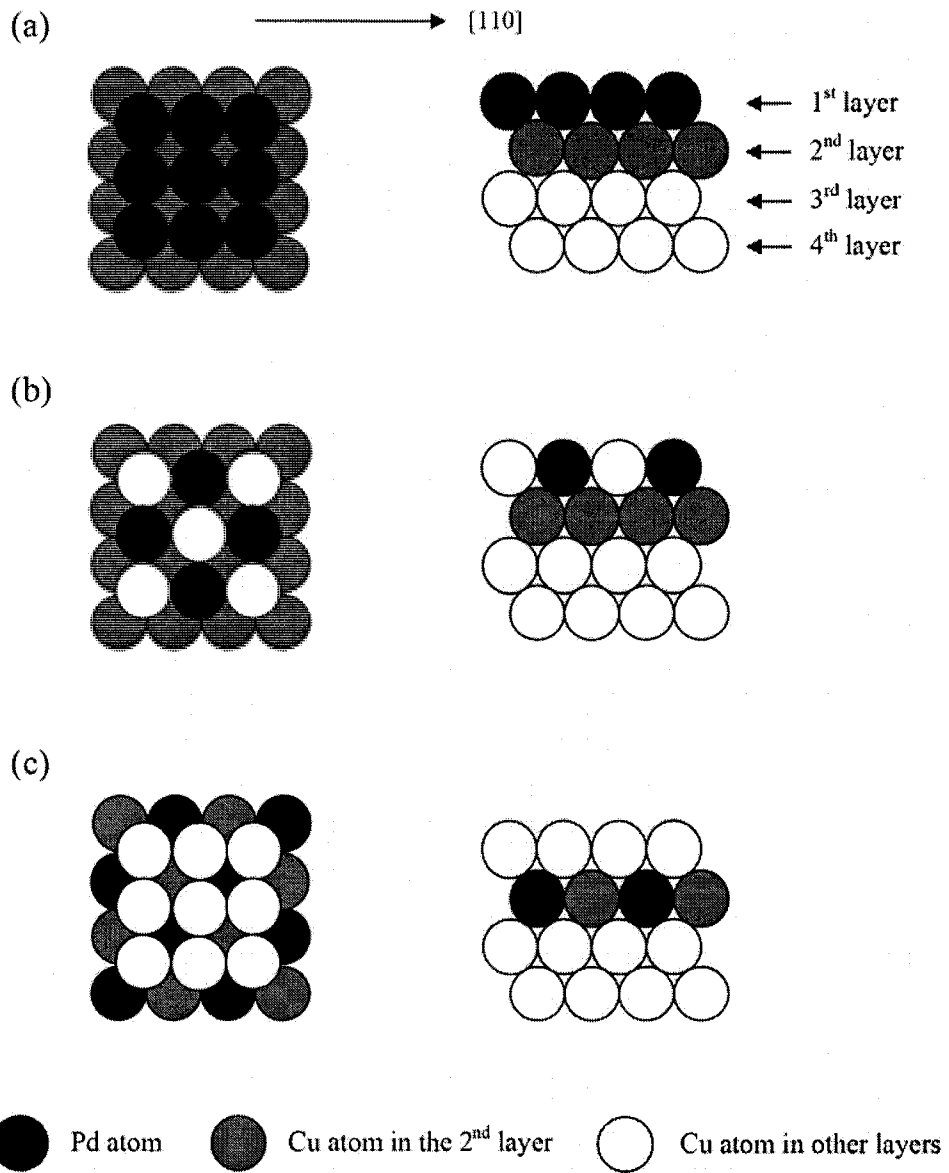
Figure 6-1: The top view (left column) and side view (right column) of CuPd surface structures on Cu(001) at different temperatures. (a) $p(1 \times 1)$ Pd overlayer below 173 K, (b) $c(2 \times 2)$ overlayer at room temperature, and (c) $c(2 \times 2)$ underlayer above about 423 K.

adatom mobility, and chemical potential gradient. These factors are in turn governed by the adatom-surface bonding strength, the substrate lattice, the morphology of the surface, and the thermal status.

Atomic diffusion at surfaces is a microscopic and complicated process. Some diffusion is treated as random walk due to the absence of dynamical theory discovered as the deterministic driving-force. High temporally and spatially resolved analytical technique is needed to elucidate the surface diffusion processes. The most used ones are FIM (field ion microscopy) and STM (scanning tunneling microscopy). By observing the displacement of surface structures, it is possible to obtain useful information regarding the manner in which the relevant species diffuse – both mechanistic and rate-related information. Diffusion processes can be simulated with kinetic Monte Carlo methods. Diffusion increases entropy, decreases Gibbs free energy, and therefore is thermodynamically favorable. So the diffusion can be studied with thermodynamic approaches. Most observed and studied adatom diffusion mechanisms include surface jumping (or hopping), atomic exchange (Fig. 6-2 (a)), and vacancy diffusion (Fig. 6-2 (b)) [158]. Recently, experimental and theoretical work has found a variety of new diffusion schemes which consist of long jumps, rebound jumps, cross-channel diffusion, and long-range atomic exchange; the readers are referred to a review by Antczak [159].

When it comes to the multilayer surface alloying, the atomic diffusion in the solid becomes more and more prominent in the deep layers. The main mechanisms for diffusion in bulk are cataloged as follows [160, 161]. (1) Interstitial diffusion. It is the case when one atom migrates to one interstitial cite by pushing apart its two NN atoms. This diffusion mostly happens to small size atoms which do not cause a too strong distortion of the host atoms they push. For our model system composed of Pd and Cu atoms, this probability of this diffusion mechanism is slim because the difference in their atom sizes is not so big
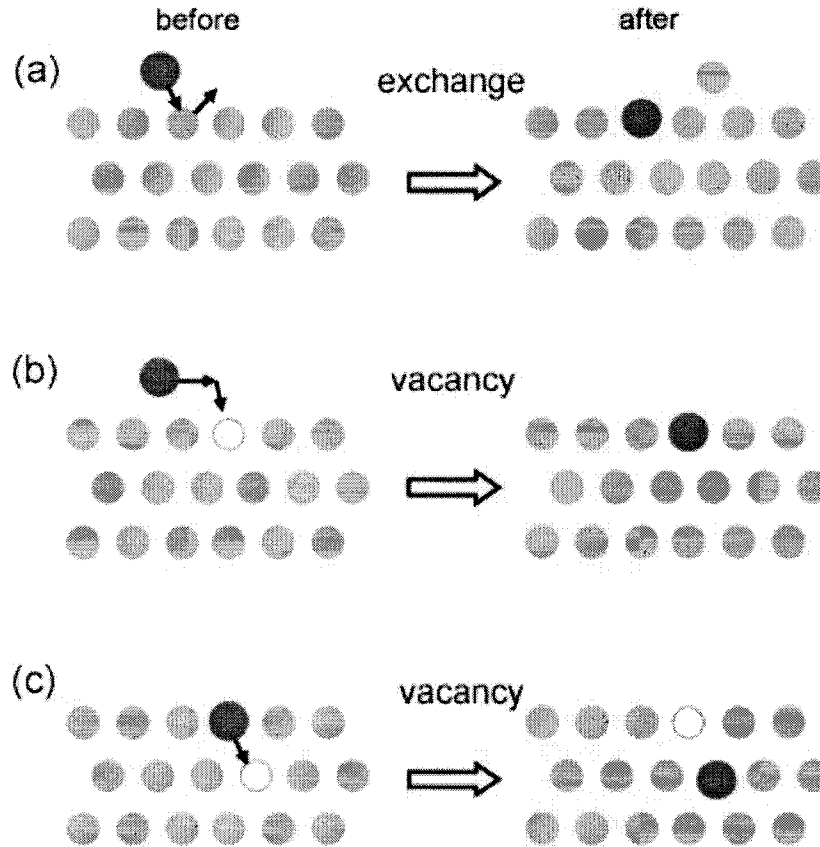
Figure 6-2: Some possible mechanisms for Pd atom diffusion. (a) top layer alloying via exchange, (b) top layer alloying via vacancy, and (c) 2nd layer alloy via vacancy. Red ball stands for the adatom, blue ball for bulk atom, and hollow circle for the vacancy site.

(atomic radius 1.28 Å for Cu and 1.37 Å for Pd). (2) Substitutional diffusion. This is the situation when two NN atoms directly interchange their cites. If this is imagined to happen by rotation of the two atoms, considerable distortions of neighboring atoms must be involved. A 'ring rotation' could contribute to this mechanism. Due to much distortions of many atoms, it is believed that the probability of this mechanism is also low. (3) Vacancy mechanism. This process is shown in Fig. 6-2 (c). In a perfect crystal, the introduction of a single vacancy increases entropy by increasing the number of configurations. At this

point the formation of a vacancy is favorable. Nevertheless, vacancies are defects and the associated defect energy (enthalpy of formation) opposes their formation. A compromise is reached whereby there is an equilibrium concentration of vacancies. The existence of vacancies will enhance the atomic diffusion in the bulk. An atom is readily jumping into its neighboring vacancy site, and thus the diffusion is contingent upon the number of point vacancies. Since the prevalence of point vacancies increases in accordance with the Arrhenius equation, the rate of crystal solid state diffusion increases with temperature. (4) Interstitialcy mechanism. This diffusion occurs when an atom pushes one of its NN atoms into an interstitial position and occupies the lattice site preciously occupied by the displaced atom. If a series of atoms are pushed and took place fast, an equivalent 'long jump' occurs.

In order to better understand the formation and stability of the temperature-dependent PdCu surface alloy structures, the energetics of PdCu overlayer and underlayer alloying have been studied by extensive electronic calculations and atomistic simulations and by some experimental measurements. Up to room temperature, Pd atoms directly migrate into the first layer forming a well-ordered $c(2\times2)$ structure and up to about 423 K Pd in the first layer is activated to jump into the 2nd layer. In these thermally-induced diffusion processes, adatom-mediated diffusion and vacancy-mediated diffusion are two main possible mechanisms. The former one means direct exchange of Pd adatom with Cu atom. This mechanism has been proved in some self-diffusion and interdiffusion systems; examples are W on Ir(110) [162], self-diffusion on Pt(001) [163], and a Co/Cu monolayer on Ru(0001) [164]. The vacancy-mediated mechanism involves vacancy formation and adatom/vacancy diffusion. It has been experimentally confirmed in some metal or metal-alloy systems such as Mn on Cu(100) [165, 166], self-diffusion on Cu(001) [167, 168], In on Cu(001) [169], Pd on Cu(001) [170, 1], and Pd on Cu(111) [171].

Grant *et al.* [170] studied the diffusion of Pd in the Pd/Cu(001) top layer alloy via atom-tracking STM. It was found that the motion of individual Pd atom landing on the surface diffuses by a vacancy-exchange mechanism. Their *ab initio* calculations and Monte Carlo simulations confirmed this process. The kinetics and mechanism of an irreversible thermally-induced overlayer-to-underlayer transition in the PdCu c(2×2) structure was investigated by LEED [2]. The activation energy for Pd site switching from the outermost layer to sub-surface (second layer) sites has been estimated to be 1.13±0.12 eV. In the sudy of the kinetics of the surface alloys formation, the following questions arise: why Pd atoms migrate from the 1st layer to the 2nd layer irreversibly? Why Pd in the 2nd layer is well-ordered and does not migrate into the 3rd layer? These questions can be answered by evaluate the atomic energetics in the system. Pope *et al.* [122] roughly estimated the diffusion energies based on the NN interactions model for clean metals. Eremeev *et al.* [1] employed the embedded-atom method (EAM) to calculate the elementary diffusive steps energies with a preferable vacancy-mediated diffusion mechanism. Specifically, the diffusion activation energy Q is calculated as the sum of vacancy formation energy E_f and adatom migration energy E_m. Table. 6.1 lists their results together with those from Refs. [170] and [2]. Corresponding to the three columns are the following three cases: (1) diffusion of a single Pd atom to be incorporated into the first layer of the Cu(001) surface, (2) diffusion of Pd atom in the top layer Cu(001)-c(2×2)-Pd completely ordered alloy system, and (3) diffusion of the Cu(001)-c(2×2)-Pd ordered alloy in the second layer and available diffusion paths for the migration of Pd atoms. E_f^i represents the copper-site vacancy formation energy in the ith-layer. E_m^{ij} denotes the migration energy of an Pd atom in the ith-layer to a vacancy site in the jth-layer. Q^{ij} is the activation energy for one Pd-vacancy exchange given as the

following:

$$Q^{ij} = E_f^j + E_m^{ij}. \qquad (6.1)$$

In case (1), the vacancy formation energy in the 2nd layer, $E_f^2 (= 1.24$ eV$)$, is much larger than the 1st layer vacancy formation energy $E_f^1 (= 0.49$ eV$)$. As a result, the activation energy $Q^{12} (= 1.51$ eV$)$ is significantly larger than that in the surface layer – $Q^{11} (= 1.51$ eV$)$. This fact accounts for the preference of the surface planar diffusion to form a top layer alloy. In case (2), both Q^{11} and Q^{12} are smaller that those for case (1). This indicates that the diffusion barriers for both in-plane and inter-plane diffusion decrease with increasing Pd coverage. The decrease in Q^{12} confirms the experimental results that diffusion of Pd into the 2nd layer begins at coverage close to 0.5 ML and not at a low coveraes [117, 150, 125]. In case (3), the activation energies from the 2nd layer to the 1st and 3rd layer are both high: $Q^{21} = 1.60$ eV and $Q^{23} = 1.79$ eV. It is suggestive of a stable 2nd layer alloy structure. Notably the vacancy formation energy in the 3rd layer is as large as 1.19 eV, close to that in the case of a clean Cu(001) surface (1.26 eV) [1] and measured value for the bulk Cu (1.27±0.05 eV) [172]. This 2nd layer alloy stability will be confirmed by our Monte Carlo simulations in this chapter. As we are going to show, the heterogeneous Pd/Cu intermixing happens in the first 3 top layers; by highly temporally- and laterally-resolved LEEM-*IV* technique, this multilayer alloying is found due to a step-mediated mechanism (step over-growth mechanism).

6.1.4   LEEM-*IV* study on the PdCu surface alloy

Here, we focus on the underlayer alloy and investigate its structural and compositional development during deposition. When Pd incorporates into the surface, the ejected Cu atoms either migrate to steps or coalesce to form new islands. Even when the incident Pd

Table 6.1: Elementary diffusion steps energies for PdCu alloying on the Cu(001) substrate. The copper-site vacancy formation energy E_f^i, palladium atom migration and diffusion activation energies E_m^{ij} and Q^{ij}, respectively, are given in eV for Cu(001), surface and sub-surface Cu(001)-$c(2\times2)$-Pd alloys. After Eremeev *et al.* [1]

Single Pd		1st layer alloy		2st layer alloy	
E_f^1	0.49	E_f^1	0.30	E_f^1	0.40
	0.474^a				
E_m^{11}	0.45	E_m^{11}	0.12	E_m^{21}	1.20
	0.466^a				
Q^{11}	0.94	Q^{11}	0.42	Q^{21}	1.60
	0.94^a				
	0.88 ± 0.03^b				
E_f^2	1.24	E_f^2	1.14	E_f^2	0.88
E_m^{12}	0.27	E_m^{12}	0.07	E_m^{22}	0.80
Q^{12}	1.51	Q^{12}	1.21	Q^{22}	1.68
			1.13 ± 0.12^c		
				E_f^3	1.19
				E_m^{23}	0.60
				Q^{23}	1.79

Superscript i denotes the copper-site vacancy formation in layer i and ij indicates migration of a Pd atom from layer i to the j-layer vacancy.
^{a} Ref. [170], *ab initio* calculation.
^{b} Ref. [170], exp.
^{c} Ref. [2], exp.

flux is low (2.5 ML/hr), significant island nucleation can occur, leading to a highly non-uniform surface. In order to limit island nucleation, we deposited Pd at 473 K and at a very low rate (about 1 ML/hr). Under these deposition conditions, we observed significantly reduced island nucleation. Submonolayer Pd is deposited on Cu(001) with a deposition rate of about 1 ML/hr at 473 K. Specular *IV* (intensity vs. voltage) curves are extracted from LEEM images and analyzed with a dynamical LEED theory (LEED-*IV*). The average *t*-matrix (ATA) method [173, 174] is used for the random alloy lattice *t*-matrix calculation. Temporal evolution of the composition on both the uniform terrace and the heterogeneous near-step areas is investigated with a resolution of ~ 8.5 nm. Studies on the uniform terrace (i.e. far from steps) show a second layer $c(2 \times 2)$ intermixing alloy capped by a nearly pure Cu top layer. The Pd concentration far from steps grows more slowly than linear, despite a constant Pd flux of about 0.9 ML/hr. Line scan studies across a step show a step-induced heterogeneous structure. Monte Carlo simulations are carried out to determine the laterally equilibrated structure in the first two layers. Results from careful tests on clean Cu(001) surfaces and Cu(001)-$c(2 \times 2)$-Pd underlayer alloys are compared with previous reports and excellent agreement is obtained [175]. LEEM image intensity analysis proves to be effective for this model system, and generally applicable to surface alloy systems.

The chapter is structured as follows. Experimental and computational methods are presented in Sec. 6.2. Tests of the LEEM-*IV* method on simple Cu(001) and Cu(001)-$c(2 \times 2)$-Pd surfaces are demonstrated in Sec. 6.3. The applications of this technique in time-resolved alloy profile measurements and in heterogeneous thin film growth are described in Sec. 6.4. Then, we present the Monte Carlo simulation results in Sec. 6.5 and a detailed analysis of the errors in the concentration profile measurements in Sec. 6.6. Finally, Sec. 6.7 concludes this paper with a summary.

6.2 Methods

6.2.1 Experiment

In our experiments we use LEEM technique to image the growth of the CuPd surface alloy *in situ* during Pd deposition onto Cu(001) using a commercial Knudsen cell. In LEEM, an image is formed from low-energy electrons (10~100 eV) reflected from the surface. In the imaging conditions we employed, both the incident and reflected beams are normal to the surface, as in conventional LEED. We place an aperture in the optical path so that only electrons in the specular beam (the (00) LEED beam) contribute to the image. Thus the LEEM image intensity measures the spatial variation of the (00) beam at a particular energy. By recording images at different beam energies, the dependence of the intensity on the beam energy (the LEED-*IV* curve) can be recorded for any point on the surface. In this way we measure the time evolution of the Pd concentration of the film with a spatial resolution of 8.5 nm and a time resolution of about 3 min. When the aperture is removed, we can record *IV* curves for different beams by imaging the diffraction plane, as in conventional LEED.

It is well known that reduced surface mass transport can give rise to island nucleation that makes the surface alloy phase inhomogeneous and rough [127, 124]. In order to reduce island nucleation, and produce a structure closer to equilibrium, we deposit Pd at a very slow rate (2.5 ML/hr) with the Cu(001) substrate held at 473 K. A LEEM image recorded using 13.1 eV electrons after the deposition of about 0.6 ML Pd is shown in Figure 6-3. Its most striking feature is the spatial variation of the contrast. The steps and island edges appear brighter than regions on the terrace. Small islands are uniformly bright. This image shows that the alloy film is inhomogeneous even when the flux is low and the deposition
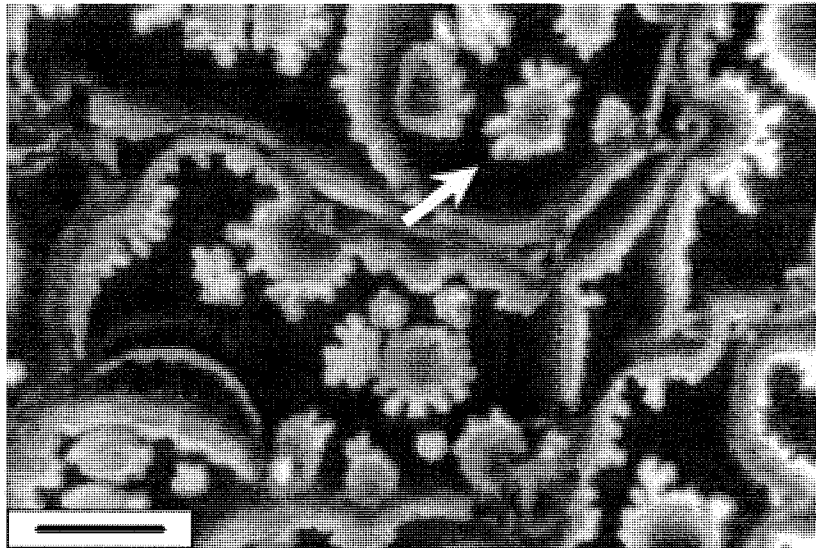
Figure 6-3: 13.1 eV LEEM image after deposition of $\approx$ 0.6 ML Pd on Cu(001) at 473 K. The image shows dendritic islands (one indicated by an arrow) and significant contrast variation near steps. Scale bar, 1 μm.

is carried out at elevated temperature. The inhomogeneity is clearly associated with the presence of atomic steps. A recent LEED analysis of a similarly-grown film suggests that the Pd is located primarily in the second layer, in a $c(2\times2)$ structure, while the surface consists almost entirely of Cu [2].

If the deposition is carried out with an even lower flux, island nucleation is further suppressed. A sequence of LEEM images recorded during a deposition with a flux of 1.0 ML/hr is shown in Figure 6-4. The images in column (a) are recorded using 13.5 eV electrons, and those in column (b) with 20.1 eV electrons. As more Pd is deposited, ejected Cu atoms diffuse to the steps, causing them to move. Far from the steps, the image intensity is uniform. However, at the upper side of the step the image intensity is spatially inhomogeneous.

The areas of interest are schematically shown in the Figure 6-5. They include (1) a local homogeneous area of clean Cu(001), (2) temporal evolution of concentration at homogeneous terrace during deposition, (3) line scan across a step, and (4) an inhomogeneous area containing a step. All studies on these areas are to be individually presented later in this chapter.

6.2.2 Quantitative analysis of LEEM intensity data

In LEED-IV analysis, IV curves are calculated for a trial structure and compared with experiment. The parameters of the trial structure, in this case the structure and alloy composition in the first three surface layers, are varied to give the best agreement with the measured IV curve. We use dynamical LEED-IV analysis to determine near-surface structure and composition from electron reflectivity data acquired using LEEM. To calculate the IV curves we used computer codes from Adams [38, 39, 37] which were developed from the programs of Pendry [17], Van Hove and Tong [18]. The codes simultaneously optimize both structural and non-structural parameters, and have been tested extensively for Al(110), Al(100)-$c(2\times2)$-Li, Al(111)-(2×2)-Na [37], and Bi(111) [81]. Up to 13 phase shifts [41] ($L = 12$) are used for the atomic t-matrix calculation. The average t-matrix approximation method is used for the random alloy lattice. For this CuPd binary alloy, an effective t-matrix $\bar{t}$ is calculated as $\bar{t} = xt_{Pd} + (1 - x)t_{Cu}$, where x is the Pd concentration and, t_{Pd} and t_{Cu} are individual t-matrices for pure Pd and Cu systems. A χ^2-based R_2 factor is employed to measure the agreement level between the experimental and theoretical data [37]. Here we show that this approach gives accurate results for both the clean Cu(001) surface as well as for the Pd/Cu(001) structures analyzed previously with conventional LEED-IV.

As mentioned in Section 3.4, some key differences between LEEM and conventional
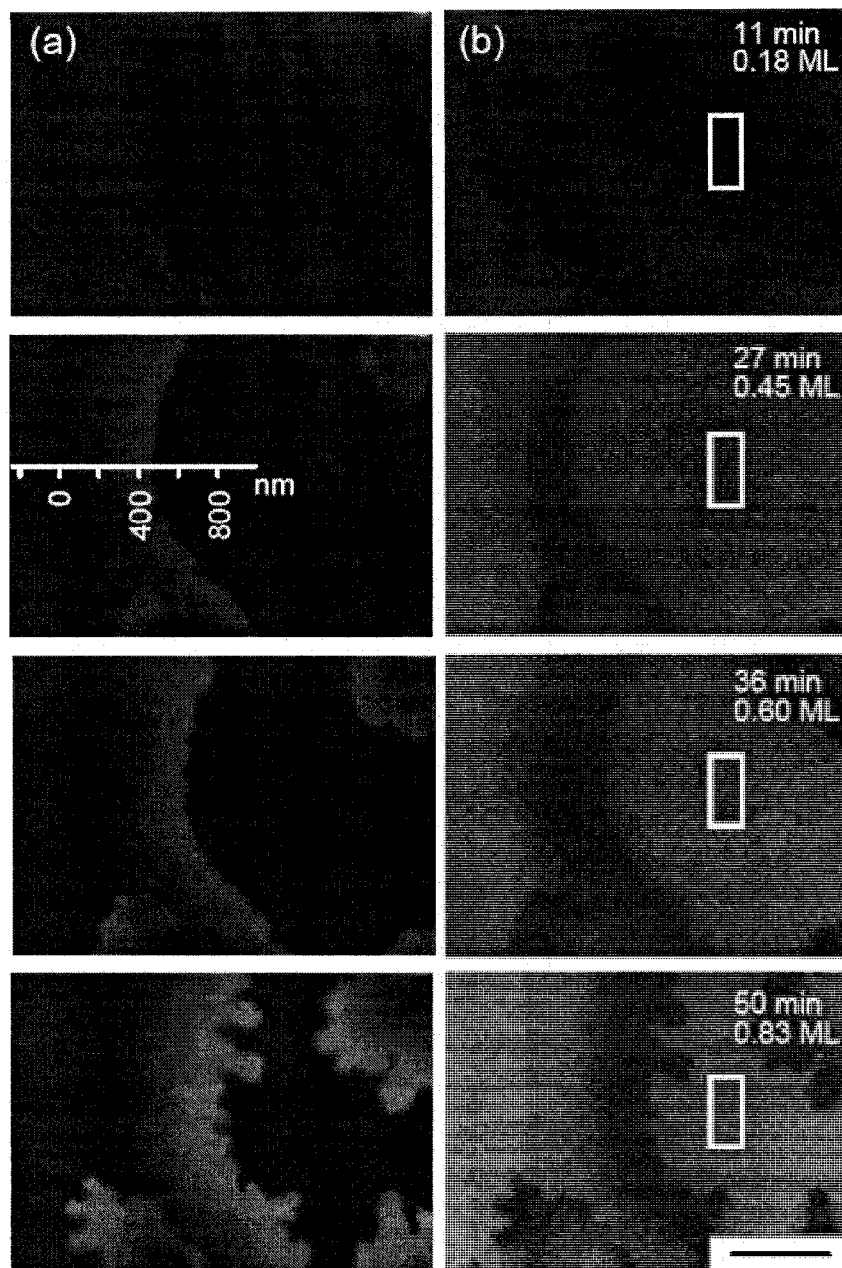
Figure 6-4: Sequence of LEEM images recorded during the deposition of Pd on Cu(001) at 473 K. The electron beam energy is 13.5 eV for the images in column (a) and 20.5 eV for the images in column (b). The images are labeled by the elapsed deposition time and the total Pd coverage. The marked line in column (a) is used for the near-step heterogeneous structure study. The rectangular area in column (b) is used for the uniform structure study on the terrace. Scale bar, 500 nm.

(1) Clean Cu(001)

(2) Temporal resolution: terrace of the alloy

(3) Spatial resolution: line scan across a step

(4) 3D resolution: circular area containing a step

Monatomic step
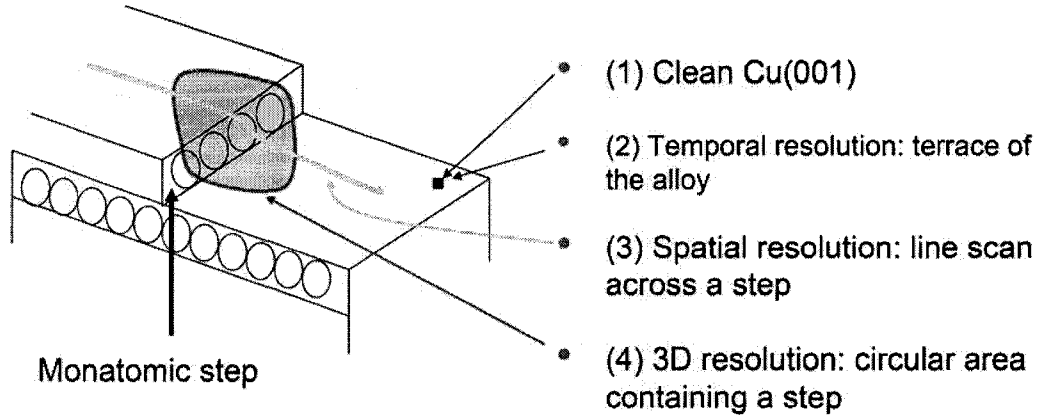
Figure 6-5: Schematic drawing of four areas of interest studied: (1) a local small area of clean Cu(001), (2) temporal evolution of concentration at terrace during deposition, (3) line scan across a step, and (4) an area containing a step.

LEED-IV are of particular concern in our analysis: (1) the relatively low electron kinetic energy in LEEM compared to LEED, and (2) the limited electron kinetic energy range in our LEEM experiments. Besides, the inelastic background should be properly treated.

In the LEEM-IV analysis, the inelastic damping potential (i.e. the imaginary part of the inner potential V_{im}) is taken to be energy-dependent. Among various proposed models, $V_{im}(E) = V_{damp}\, E^{1/3}$ is found to give the best agreement between the measured and calculated IV curves for clean Cu(001). Demuth *et al.* [176] used this exponential form for low-index surfaces of Ni for energies in the range 10 to 220 eV. In addition, Noonan and Davis [177, 178] used this form for both Cu(110) and Cu(001). We optimized the constant pre-factor V_{damp} as an independent non-structural parameter in our calculations; see Table 6.2.

For the real part of the inner potential $V_0(E)$ we used the form shown in Equation 3.1. This correction to the real part of the inner potential resolved a controversial claim of an

117

in-plane contraction reported in a recent LEED-*IV* study on Cu(001) [179]. We include an overall additive constant (ΔV_0) to Equation 3.1 as an independent non-structural parameter in our optimization; see Table 6.2. These energy-dependent inner potential models are the most suitable approximation we can use for our system and they proved to describe the surface alloy very well.

LEEM images contain a contribution from inelastically scattered and secondary electrons. This contribution can be measured directly by integrating the background intensity near the (00) diffraction spot in diffraction mode. The inelastically scattered electrons are dispersed out of the optical path by the LEEM prism, so their contribution to the image intensity decreases rapidly with increasing beam energy. We find that the background in our images is approximately proportional to $\exp(-E/30)$, where E is the electron kinetic energy in eV.

6.3 Test of the LEEM-*IV* technique

6.3.1 LEED analysis of clean Cu(001)

We tested our treatment of low-energy electrons by analyzing LEEM data recorded in "diffraction mode". In this mode we record spatially-averaged diffraction patterns, just as in conventional LEED. A typical diffraction image from clean Cu(001) terrace indicated in Figure 6-5 (1) is shown in Figure 6-6. The *IV* curves of three symmetry in-equivalent beams (00), (10), and (11) from clean Cu(001) measured in this way are shown in Figure 6-7. The Debye temperature of the bulk is fixed at 315 K, while the vibrational amplitudes for the first two layers are optimized.

A direct comparison of the computed and measured *IV* curves is given in Figure 6-7.
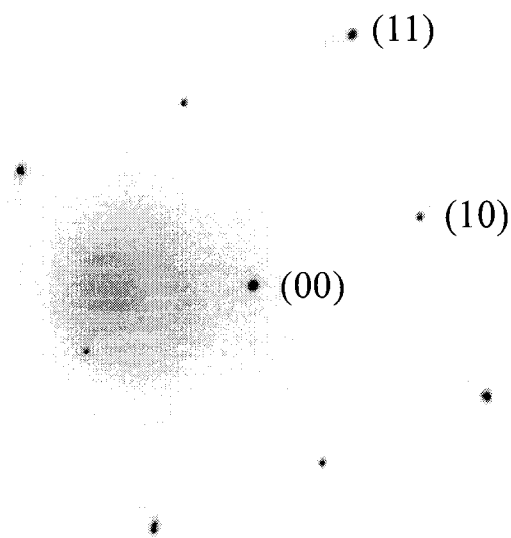
Figure 6-6: Diffraction pattern for clean Cu(001) at 46.2 eV measured in the LEEM. The diffuse intensity in the left of the image is due to secondary electrons, which are not filtered out of the image.
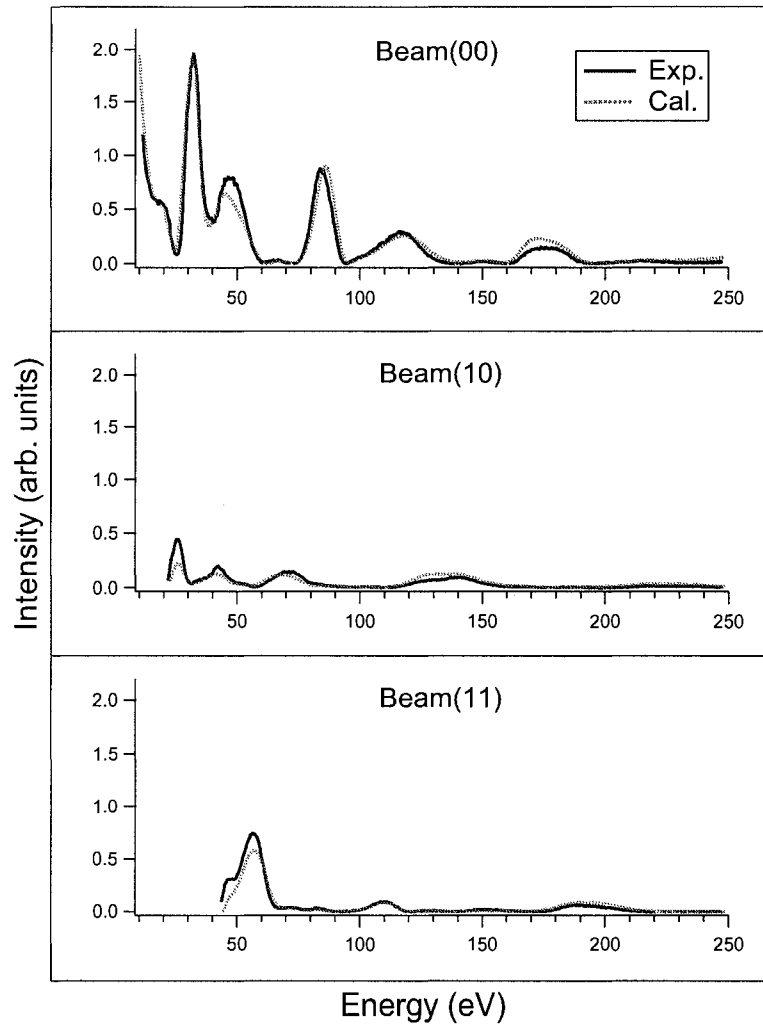
Figure 6-7: Measured (solid) and best-fit calculated (dotted) *IV* curves for clean Cu(001) at 473 K. The same scaling factor is used for all three beams.

The agreement is excellent. The inclusion of an energy-dependent V_0 greatly improves the agreement in the peak positions. The energy-dependent V_{im} is essential in reproducing the relative peak intensities, especially at low energies. The best-fit structural parameters for clean Cu(001) are summarized in Table 6.2. The error bars in the clean surface analysis are based on an increase of 4% in the R_2 factor [37]. We find a contraction of 1.6% in the first interlayer spacing and an expansion of 1.0% in the second in contrast to the bulk interlayer spacing of 1.811 Å. The Debye temperatures for the first two top layers are found to be lower than the bulk, characteristic of larger atomic vibrational amplitudes at the surface. The results agree very well with previous investigations by LEED-*IV* [178], spin-polarized LEED[180] and medium-energy ion scattering [181].

6.3.2   LEEM Analysis of clean Cu(001)

Next we compare the *IV*-spectra of the (00) beam extracted in both LEED and LEEM modes, and perform a structural analysis solely based on the latter. The measured LEEM image intensity (solid curve) from clean Cu(001) at 313 K, as a function of electron kinetic energy, is shown in Figure 6-8 together with the *IV* curve measured in diffraction mode (dash-dotted curve). The inelastic background, described above, has been subtracted from the solid curve. The agreement is very good, demonstrating the equivalence of measuring the (00) peak intensity in either LEEM or LEED mode.

We have performed a structural analysis using only data from the (00) beam up to 250 eV. We find good agreement between the computed (dashed curve) and measured *IV* curves. Specifically, we find $d_{12} = -1.6 \pm 0.9\%$, $d_{23} = +1.5 \pm 2.0\%$, with an R_2 factor of 0.051. These results agree well with previous investigations summarized in Table 6.2. It shows that the (00) *IV* curve contains enough information, even over a limited energy

Parameters	starting values	optimized values	$\Delta d/d^{\mathrm{b}}$ (%)				Θ_D (K)
			This work	Ref. [178]	Ref. [180]	Ref. [181]	
d_{12} (Å)	1.811	1.78 ± 0.016	-1.6 ± 0.9	-1.0 ± 0.4	-1.2	-2.4	-
d_{23} (Å)	1.811	1.83 ± 0.033	$+1.0 \pm 1.8$	$+1.7 \pm 0.6$	$+0.9$	$+0.9$	-
u_1 (Å)	0.182	0.27 ± 0.020	-	-	-	-	213^{+17}_{-15}
u_2 (Å)	0.182	0.19 ± 0.017	-	-	-	-	300^{+30}_{-25}
V_{damp}	0.80	0.92 ± 0.07	-	-	-	-	-
ΔV_0 (eV)	0.00	1.02 ± 0.31	-	-	-	-	-
c	198.7	121.3 ± 22.2	-	-	-	-	-
R factor	0.647	0.038	-	-	-	-	-

Table 6.2: Optimum parameter values for Cu(001) at 473 K. Interlayer spacings between the ith and jth layers are denoted as d_{ij}. Root-mean-square vibrational amplitudes for atoms in the ith layer are denoted as u_i. V_{damp} is the pre-factor of the imaginary part of the inner potential. ΔV_0 is the overall shift of the real part of the inner potential to Equation 3.1. c is the global scaling constant from beam to beam. d^{b} is the corresponding interlayer spacing of the truncated bulk at 473 K. Θ_D is the Debye temperature calculated from u_i.
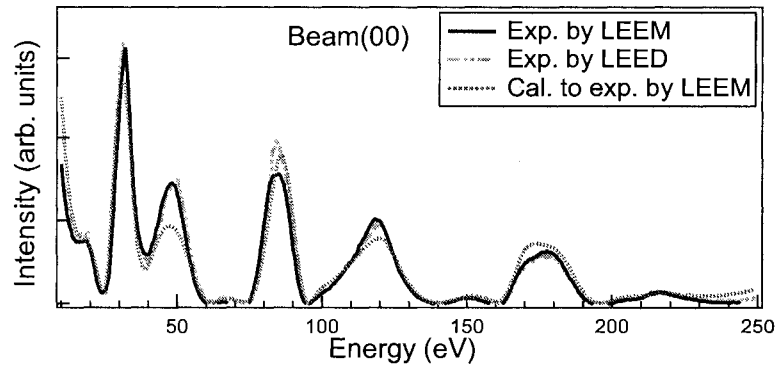
Figure 6-8: Comparison between the (00) beam intensity measured in LEEM (solid), LEED (dash-dotted) and the best-fit (dotted) to the LEEM curve.

range, to perform an accurate structural analysis.

6.3.3   LEEM Analysis of Cu(001)-$c(2 \times 2)$-Pd

The analysis of clean Cu(001) shows that data from the (00) beam is sufficient to determine the surface structural parameters, i.e. the interlayer spacings. We tested our ability to determine layer-resolved Pd concentrations by analyzing a known alloy structure: the Pd/Cu(100) alloy phase prepared by depositing 0.6 ML of Pd on Cu(001) at 473 K. Again, in our analysis we include only data from the (00) beam over an energy range $10 \sim 100$ eV. To reduce noise, we average the image intensity over the boxed region indicated in Figure 6-4. It is clear from the images that the intensity (and structure) is homogeneous far from the step. This same procedure cannot be used near the step, where the intensity is spatially inhomogeneous. The basic structure of this phase is determined using conventional LEED-*IV* by Barnes *et al.* [2] who deposited Pd at room temperature until the (1/2, 1/2) beam intensity reached a maximum, followed by annealing at 550 K. According to the early work by Pope *et al.* [121] the maximum (1/2, 1/2) beam intensity occurs at a Pd coverage of 0.55 ± 0.10 ML. Barnes showed that upon annealing, almost all of the Pd migrates to the 2nd layer in a $c(2 \times 2)$ alloy structure.

Our LEEM intensity data for this phase is shown as the 0.60 ML curve (solid) in Figure 6-9(a). In our analysis, each of the three topmost layers is divided into two $c(2 \times 2)$ checkerboard sublattices. The ATA method is used to calculate random alloy t-matrices for each sublattice. Independently optimized compositional parameters are θ_{11} and θ_{12}, θ_{21} and θ_{22}, θ_{31} and θ_{32}, representing the Cu concentration (in ML) in each of the two sublattices of the 1st, the 2nd, and the 3rd layer, respectively. Note that we make no assumption about the total amount of Pd in the film. All of these parameters are allowed to vary within an

interval of 0 to 1 ML at a step of 0.001 ML during optimization. The Pd concentration in the ith layer, c_i, is given by: $c_i = 1 - (\theta_{i1} + \theta_{i2})/2$, $(i = 1, 2, 3)$. A value of 0.86 for V_{damp} is used for this structure. Debye temperatures for all layers are fixed at the bulk value, i.e. 315 K for Cu and 275 K for Pd. We did not optimize the Debye temperature but simply tested different values and found no significant structural changes. The best-fit values of the main parameters are shown in Table 6.3, which are in excellent agreement with those found by Barnes *et al.* [2] Specifically, we find that the Pd resides entirely in one sublattice in the 2nd layer. This is in agreement with the checkerboard model. The bulk interlayer spacings used in this work and Ref. [2] are 1.811 and 1.805 Å, respectively. z_2 and z_4 are the ripplings of the sublattices in the 2nd layer and the 4th layer, respectively. The value of rippling in the 2nd layer indicates a small upward shift of the Cu sublattice normal to the surface due to size difference between Cu and Pd atoms. In our work, z_4 is not optimized while in Ref. [2] a significant rippling of 0.2 Å in z_4 was reported. However, *ab initio* modeling [151] does not support substantial rippling in the 4th layer. A comparison between the measured and computed *IV* spectra is shown in Figure 6-9(a).

In conclusion, excellent agreement between experimental and calculated (00) beam *IV* curves has been obtained for both clean Cu(001) as well as for a known Pd/Cu(001) underlayer alloy structure. The structural parameters derived from our analysis agree well with those determined using conventional LEED. Notably in the underlayer alloy case, we get consistent results even without a large buckling in the 4th layer. These results give us confidence that our analysis is capable of determining surface structural and compositional parameters for Pd/Cu(001) structures with high accuracy.

Parameters	This work	Ref. [2]
d_{12} (Å)	1.85	1.86
d_{23} (Å)	1.85	1.85
θ_{11} (ML)	1.00	-
θ_{12} (ML)	0.89	-
c_1 (ML)	*0.06*	fixed at *0*
θ_{21} (ML)	1.00	-
θ_{22} (ML)	0.04	-
c_2 (ML)	*0.48*	fixed at *0.5*
θ_{31} (ML)	0.97	-
θ_{32} (ML)	1.00	-
c_3 (ML)	*0.02*	fixed at *0*
z_2 (Å)	0.05	0.07
z_4 (Å)	fixed at 0	0.2
R factor	0.009	0.28 (R_p)

Table 6.3: Comparison of results for this work with that of Barnes *et al.* [2] for the Cu(001)-$c(2\times2)$-Pd alloy. d_{12} and d_{23} are the 1st and the 2nd interlayer spacing, respectively. θ_{11} and θ_{12}, θ_{21} and θ_{22}, θ_{31} and θ_{32}, representing the Cu concentration in each of the two sublattices of the 1st, the 2nd, the 3rd layer, respectively. c_1, c_2 and c_3, the Pd concentration for the three top-most layers, $c_i = 1 - (\theta_{i1} + \theta_{i2})/2$, $(i = 1, 2, 3)$. z_2 and z_4 are the rippling of sublattices in the 2nd layer and the 4th layer, respectively.

6.4 Applications

6.4.1 Temporal evolution of Pd concentrations on terrace

First, we apply this technique to resolve the PdCu film growth during deposition on the terrace, as shown in Figure 6-5 (2). Figure 6-4 shows a sequence of LEEM images recorded during deposition of Pd with a flux of 1.0 ML/hr. The images in column (a) and (b) are recorded at 13.5 eV and 20.1 eV beam energies, respectively. There is an atomic step running vertically near the center of the images. As Pd is deposited, the step moves to the right due to the attachment of ejected Cu atoms. As growth proceeds the contrast variation in the image increases. The step profile is initially smooth, but becomes wavy as the amount of Pd in the surface region increases. Quantitative analysis of the image intensity, described below, shows that the image appears bright at 20.5 eV when significant amounts of Pd reside in the second layer. At 13.5 eV, the image appears bright when the amount of Pd in the third layer is large. Thus the images in column (a) show qualitatively how the amount of Pd in the third layer evolves with time while those in column (b) show how the second layer evolves. The images show directly that the Pd concentration is uniform on the terrace, but is highly inhomogeneous at the upper side of atomic steps. The evolution of the alloy composition can be determined quantitatively by analyzing the full IV curves at each point on the surface with a resolution of ~ 8.5 nm. We do this by acquiring images while the electron beam energy is swept from 10 to 100 eV. The heterogeneous structure has been found to be induced by step flow [182] and will be further described in the next section.

Here we describe the analysis of the uniform areas on the terrace far from steps. IV curves from the terrace at four different Pd coverages, i.e. deposition times, are shown in Figure 6-9(a). The IV data are obtained by averaging over a local rectangular homogeneous

126
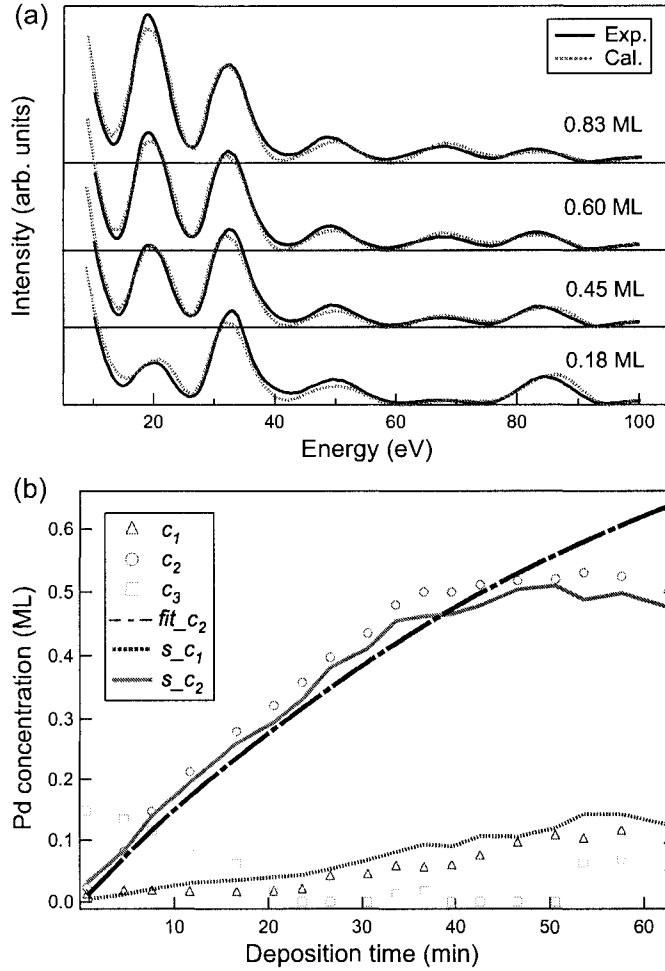
Figure 6-9: Analysis of the Pd concentration on the terrace (averaged over the white rectangle in Figure 6-4). (a) Measured (solid) and computed (dotted) image intensity as a function of electron beam energy at four different Pd coverages. (b) Corresponding time evolution of the Pd concentrations c_i ($i = 1, 2, 3$) for the first three surface layers. Fit_c_2 is the fitting curve of c_2 according to Equation 6.2 with a flux of 0.9 ML/hr. s_c_1 and s_c_2 are simulated uptake curves for c_1 and c_2.

region indicated in Figure 6-4. The most obvious change in the IV curve with increasing

Pd coverage is the growth of the peak around 20 eV. The evolution of the composition of

the film can be determined by comparing the measured IV curves to electron scattering

calculations as in conventional LEED. Using the procedure outlined in the preceding section,

we determine the Pd concentration in each of the first three surface layers. We recorded IV

curves at 3 minute intervals, thus we can determine the evolution of the Pd coverage with

3 minute time resolution. The results of this analysis are shown in Figure 6-9(b), where the

Pd concentrations in the surface (c_1), second (c_2), and third (c_3) layers, far from steps, are

shown as a function of time. The analysis shows that c_2 grows monotonically with time,

while c_1 and c_3 are both small, and essentially constant. The small value of c_3 suggests that

direct migration of Pd from the second layer to the third is slow, even at 473 K. If the Pd

atoms were evenly distributed on the terrace during growth the total Pd concentration, c_1

$+ c_2 + c_3$, would grow linearly with time, which it does not. It appears that while the Pd

concentration on the terrace is laterally equilibrated (i.e. uniform image intensity), some of

the incident Pd flux is lost from the terrace. Previously, we showed that some Pd from the

terrace is irreversibly buried by the advancing step [182]. Here we show that the same step

flow model describes how the concentration of Pd on the terrace develops with time. We

assume there is a constant flux, F, of Pd incident onto the surface. Under our deposition

conditions at an elevated temperature (473 K), Pd deposited onto the surface migrates

preferentially to the second layer. For simplicity we assume that all of the deposited Pd

initially goes to the second layer and that migration to other layers does not occur ($c_1 =$

$c_3 = 0$). We further assume that surface mass transport is fast, and that consequently the

Pd concentration in the second layer, c_2, is spatially uniform. As the step advances during

growth, Pd in the second layer in front of the advancing step is converted into third layer

Pd trailing the step. In this simplified scenario, the time evolution of c_2 far from a step, is given by

$$c_2 = 1 - e^{-Ft}. \qquad (6.2)$$

The derivation of this equation is as follows. Suppose the 2nd layer Pd concentration at time t is c_2 and the terrace width is L. Assume all the ejected Cu atoms will be rapidly attached to the step edge. After an infinitesimal time dt, the step moves a distance of $LFdt$ which buries the terrace and converts the 2nd layer Pd into the 3rd layer. So the lost Pd from the 2nd layer is $c*LFdt$. During the period of time dt, all incorporated Pd amount is Fdt. Consequently, the resulting increase in 2nd layer Pd concentration (dc_2) is

$$dc_2 = Fdt - c_2 * (LFdt)/L. \qquad (6.3)$$

Combined with the initial condition $c_2 = 0$ at $t = 0$, the solution of Equation 6.3 is given in Equation 6.2. The dash-dotted curve in Figure 6-9(b) shows a fit to Equation 6.2 corresponding to $F = 0.9$ ML/hr. The fit agrees reasonably well with the LEED analysis, suggesting that the sub-linear growth in the total Pd coverage with time is consistent with burying of Pd by the advancing step. Because the small increase in c_1 with time is ignored, fitting to c_2 alone underestimates the true flux. If it is assumed that both c_1 and c_2 are buried by the step, i.e. if one overestimates the amount of Pd lost to step overgrowth, a value of $F = 1.1$ ML/hr is obtained. In the following we assume $F = 1.0$ ML/hr, a value consistent with the observed step motion during growth.

6.4.2 Step over-growth of surface alloy

Secondly, we use the technique to investigate the heterogeneity along the line scan shown in the Figure 6-5. A series of LEEM images recorded during Pd growth is shown in Figure 6-4. Each image is labeled by the deposition time and total Pd coverage. During the growth we

periodically ramped the energy from 10 to 100 eV. From this data we construct IV curves for each point in the image with a time resolution of about 3 minutes. For each IV curve we can perform a full dynamical LEED analysis to determine the local structural parameters and layer-resolved Pd concentration (i.e. in each individual image pixel). This data allows us to determine how the three-dimensional Pd concentration evolves with time. It is clear that the image contrast is heterogeneous at the upper side of the step. In Figure 6-10 we show how the Pd concentration evolves along the line indicated in Figure 6-4. The four panels show the Pd concentrations (along the same line) at four different deposition times.

The most striking feature of the concentration profiles is the asymmetry in the third-layer Pd concentration, c_3. In front of the advancing step (i.e. at large x) c_3 is essentially zero. However, at the trailing side of the step, c_3 is large at the step position, but decays monotonically away from it (i.e. towards $x = 0$). With time, the amount of Pd at the step edge grows.

The presence of third-layer Pd exclusively at the upper side of the step suggests a possible mechanism driving the heterogeneity: alloying via step overgrowth. The principle is illustrated schematically in Figure 6-11. The figure shows a side view of the surface near a step at three times $t_1 < t_2 < t_3$ during Pd deposition at 473 K. We label the Pd concentrations in the first three surface layers c_1, c_2, and c_3. Motivated by the experimental results, we assume that there is no Pd in the first layer ($c_1 = 0$) and that Pd in the second layer (c_2) is spatially uniform (due to rapid surface diffusion). Furthermore, we assume that there is no direct migration of Pd to the third layer ($c_3 = 0$ far from the steps). As more Pd is deposited, the concentration of Pd in the second layer increases and the step moves to the right due to the attachment of ejected Cu atoms. Part of the surface is overgrown by the advancing step, effectively transferring Pd from the second layer (in front of the step)
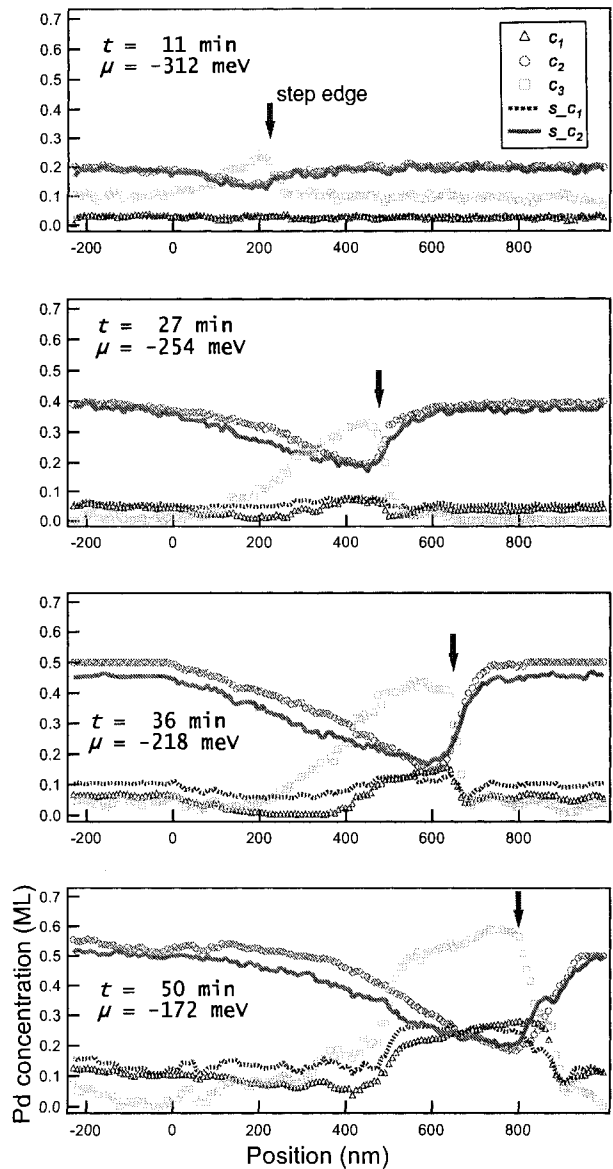
Figure 6-10: Measured Pd concentration profiles across an advancing step and equilibrated concentration distributions in the first two layers from Monte Carlo simulations. c_i ($i = 1, 2, 3$) are measured data for the ith layer. s_c_i ($i = 1, 2$) are the simulated profiles. Each panel corresponds to one deposition time. The chemical potential μ is shown and $\epsilon = -25$ meV. The arrows point to the step edge position.
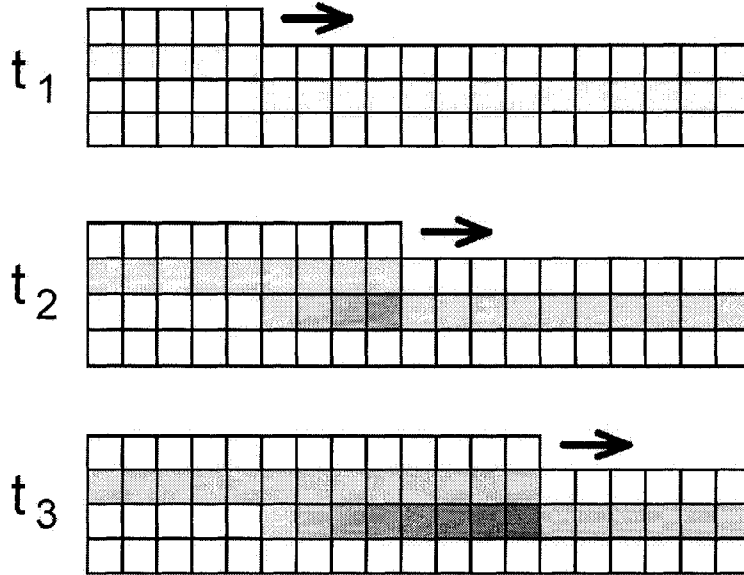
Figure 6-11: A schematic illustrating how heterogeneity arises during step-flow overgrowth. Side views of the Cu surface are shown at three times ($t_1 < t_2 < t_3$) during the deposition of Pd. The denser color indicates higher Pd concentration. Step flow overgrowth converts mobile Pd in the second layer into fixed Pd in the third layer.

to the third layer (behind the step). The mobility of Pd in the third layer is presumably much lower than that of Pd in the second layer because the environment is "bulklike". The activation energy for vacancy-mediated diffusion in bulk copper is 2.06 eV [172], while that for vacancy-mediated self-diffusion at the (001) surface is only 0.80 eV [168]. Pd transferred to the third layer is virtually immobile at 473 K. In the simplest scenario, the amount of Pd buried by the step is equal to the instantaneous concentration in the second layer, leading to a characteristic profile for c_3 in the overgrown region.

We now describe how the alloy compositions measured near a step validate the step-overgrowth model. Three key signatures of the overgrowth model are (1) the asymmetry in the third-layer Pd concentration near a step, (2) the characteristic profile of the third-layer Pd in the overgrown region, and (3) the correlation between third-layer Pd behind the step

and the second-layer Pd in front of the step. Each of these predictions can be rigorously tested by analyzing the Pd concentration near the step. IV curves from four points along a line crossing a step are shown in Figure 6-12. The most significant differences between the curves occur for energies below 30 eV. In the overgrown region, the intensity of the peak near 20 eV is lower, and a low energy shoulder is present at about 13 eV. We find very good agreement between the calculated and measured IV curves at all points on the surface. The variation in c_1, c_2, and c_3 along a line crossing a step is shown Figure 6-10. Take the case of $t = 27$ min for example, the analysis shows that most of the Pd is located in the second layer, in agreement with previous LEED studies [2]. Away from the step, the concentrations are spatially uniform, with $c_2 \approx 0.4$ and c_1 and c_3 about zero. Near the step, c_3 is large on the upper side of the step but drops dramatically to zero at the step position. The value of c_3 at the upper side of the step is equal to that of c_2 on the lower side of the step. This correlation strongly suggests that Pd in the third layer arrives there via the stepovergrowth process. The time evolution of c_3 further confirms this picture. The variation in c_3 near the step is shown in Figure 6-13 for three different times of 27, 36 and 50 min during Pd deposition. It is clear that the amount of Pd buried by the step increases monotonically with time as the step moves. If the buried Pd is immobile, the profile of c_3 in the overgrown region should not change with time. For example, the three curves shown in Figure 6-13 should agree for x < 500 nm, which they do. This suggests that diffusion into or out of the third layer is slow at 473 K. The data in Figure 6-10 suggest that the Pd instantaneously buried by the step is equal to the value of c_2 on the terrace. That is, the spatial profile of the buried Pd is related to the time profile of the Pd in the second layer. In other words, $c_3(x(t)) = c_2(t)$, where $x(t)$ is the step position. We have measured both $x(t)$ and $c(t)$ (far from the steps), which allows us to test this prediction. The dark thicker line in Figure 6-13

133

shows the profile predicted by the stepovergrowth model. The agreement is quite good, showing that the spatial profile of the buried Pd $c(x)$ is directly related to the distribution of mobile Pd on the terrace $c_2(t)$. The direct comparison of the measured and predicted alloy composition profiles confirms the basic picture of compositional heterogeneity driven by step overgrowth.

We have shown that step overgrowth converts mobile, second-layer Pd into immobile Pd in the third layer. We now show how correlations between the amount of Pd in neighboring layers gives insight into the bonding and stability of the alloy film. As discussed above, the profile for c_3 in Figure 6-10 is determined by the step-overgrowth mechanism. Contrary to the assumptions of the simplified step-overgrowth model (Figure 6-11), c_2 is not spatially uniform. Far from the step, c_2 is constant, but near the step it decreases to half that value. One possibility is that surface diffusion is inhibited (e.g., when c_3 is large) and that c_2 is not equilibrated laterally. An alternative scenario is that the c_2 is equilibrated and that the variation in c_2 with c_3 is due to a repulsive Pd-Pd interaction. In this case, the correlation between c_2 and c_3 can be used to infer the strength of this interaction. For example, if there were no interaction between Pd atoms, then c_2 would be spatially uniform, and there would be no correlation with c_3. Alternatively, if Pd atoms strongly repel, then c_2 will be small when c_3 is large, and vice versa. Consider a highly simplified model in which the internal energy of the film is proportional to the number of Cu-Pd nearest-neighbor (NN) bonds. This model is motivated by the stability of the c(2×2) structure, in which all of the Pd NNs are Cu, and is supported by first-principles calculations [128] as well as empirical modeling [125]. The theoretical analysis of the bonding shows that Cu-Pd NN bonds are favored over both Cu-Cu and Pd-Pd bonds. In the following Sec. 6.5, we perform Monte Carlo simulations on the model to determine if the measured correlation between c_2 and c_3

is consistent with a fully equilibrated second layer.

6.4.3   3D mapping of surface structure and composition

Lastly, we apply the LEEM-*IV* analysis in a circular area on the surface shown in Figure 6-5 (4). Over 17,665 pixels in a circle of diameter 1.25 μm have been analyzed with the spatial resolution of 8.5 nm. The results are shown in Figure 6-14 for the concentration of Pd in each of the first three layers of the surface after the deposition of 0.45 ML of Pd at 473 K. The analysis shows that the top layer is almost entirely Cu, while most of the deposited Pd is located in the second layer. Near the step, there are significant variations in the Pd concentration. There is a substantial amount of Pd in the third layer on the upper side of the step, while on the lower side there is virtually none in the third layer. A sharp step edge is evident in the images. Therefore, it has been demonstrated, for the first time, to be able to measure the 3D mapping of concentration profile at such a high lateral resolution as 8.5 nm.

6.5   Monte Carlo simulations

In the simple model outlined above, we assumed that all of the deposited Pd migrates to the second layer, and that the Pd from the terrace eventually becomes buried by the advancing step. In previous work, we described a more realistic model based on the energetics of Pd-Cu bonding. As we show below, this model can be used to predict the time evolution of the Pd concentration profiles, in each layer, both on the terrace and in the heterogeneous regions near the step.

The central premise of the model is that Cu-Pd nearest-neighbor bonds are favored. This idea is motivated by the stability of the $c(2 \times 2)$ structure, which contains only Cu-Pd

135
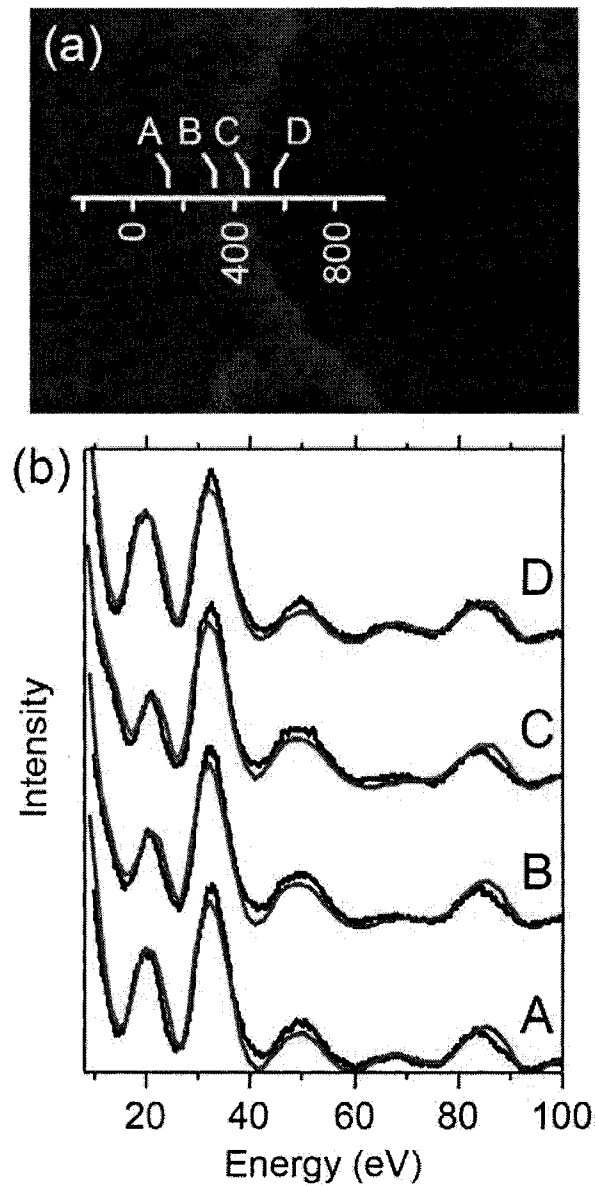
Figure 6-12: Measured and calculated IV curves near an atomic step. (a) 13.5 eV LEEM image recorded after the deposition of 0.45 ML of Pd at 473 K. Distances, x, along the line scan indicated are given in nm. At the start of Pd deposition, the step is located at $x = 0$. (b) Measured (black) and computed (red) IV curves for the four points indicated in (a).
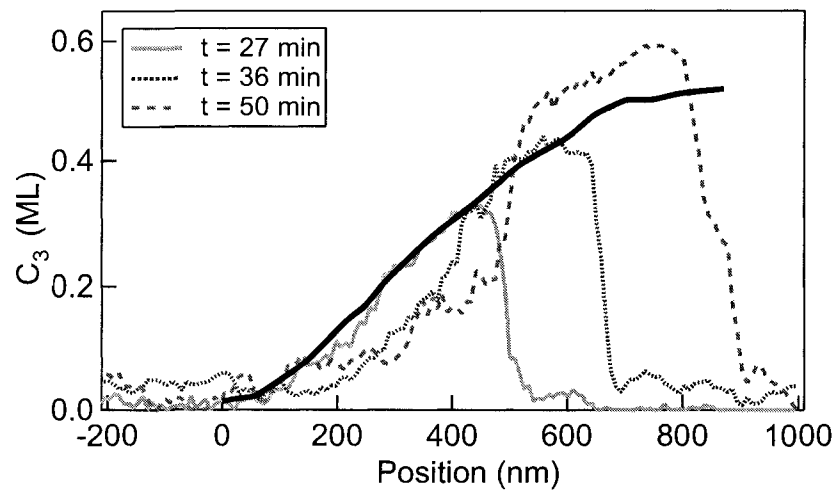
Figure 6-13: Pd concentration along the line indicated in Figure 6-4 (a). Third layer Pd concentration measured at three different deposition times of 27, 36, 50 min during deposition. During growth the step advances to the right. The darker thicker curve is the 2nd layer Pd concentration on terrace.
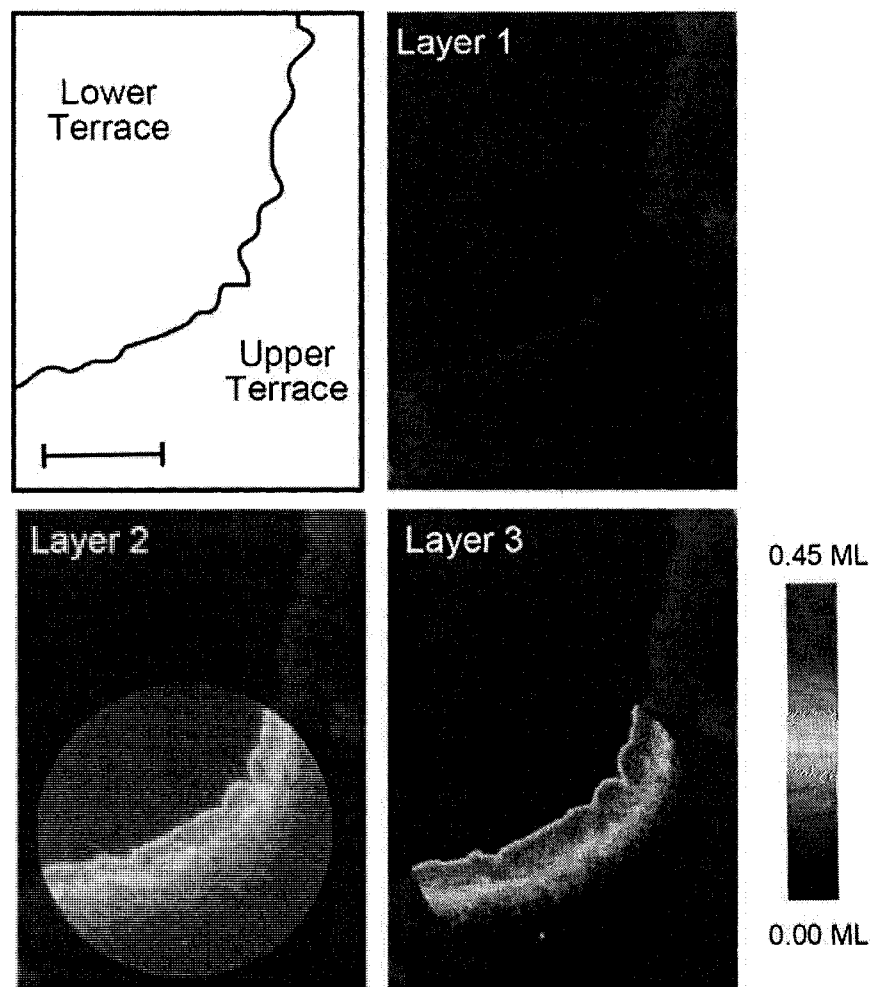
Figure 6-14: Three-dimensional map of the Pd concentration near a surface step. The images are constructed from the analysis of 17,665 individual pixels and show the concentrations in the first three surface layers after deposition of 0.45 ML of Pd (27 min.) at 473 K. The spatial resolution is 8.5 nm. The maps are superimposed on the corresponding LEEM image at 13.1 eV. Scale bar, 500 nm.

NN bonds, and is supported by first-principles calculations [128], empirical modeling [125], as well as embedded-atom method calculations [133], which showed that Cu-Pd NN bonds are favored over both Cu-Cu and Pd-Pd bonds. In the Monte Carlo simulations, the internal energy of the film is equal to ϵN, where ϵ is the energy of one Cu-Pd NN bond, and N is the number of such bonds. ϵ is negative, so the system adopts a structure that favors Cu-Pd nearest neighbors. The simulations are carried out on four-layer slabs with 20×20 atoms in each layer with periodic boundary conditions. The atoms in both the third and fourth layers are fixed. The Metropolis algorithm [62] is used to determine the equilibrium distribution of Pd atoms in the film. The equilibration process is carried out until the average quantities show no change. For all the simulations, typically the average energy reaches equilibrium after 500 attempted Cu/Pd swaps per free atom (i.e. 4×10^5 total trial moves). Equilibrium quantities, e.g. system energy and Pd concentrations, are computed by averaging over an additional 8×10^4 trial moves once the energy is equilibrated.

In the Monte Carlo simulations of the temporal evolution of the concentrations on the terrace, we compute the values of c_1 and c_2 as a function of total coverage, while c_3 is fixed at the measured value. That is, we compute how a given total coverage on the terrace, $c_1 + c_2$, is partitioned between the first and second layers, while the Pd coverage in the third layer is fixed. This is a constant-NVT simulation in which we treat the system as a canonical ensemble [183]. A trial move in this simulation involves atom-identity exchange within the first two layers. Simulated results are shown in Figure 6-9(b). s_c_1 and s_c_2 are simulated Pd concentration uptake curves for the first and the second layer. The agreement with experimental data is good, showing that the simple model quantitatively predicts both the spatial and temporal evolution of the alloy composition. In this simulation, ϵ is obtained as -25 meV. An example of a simulated equilibrium structure is shown in Figure 6-15 for
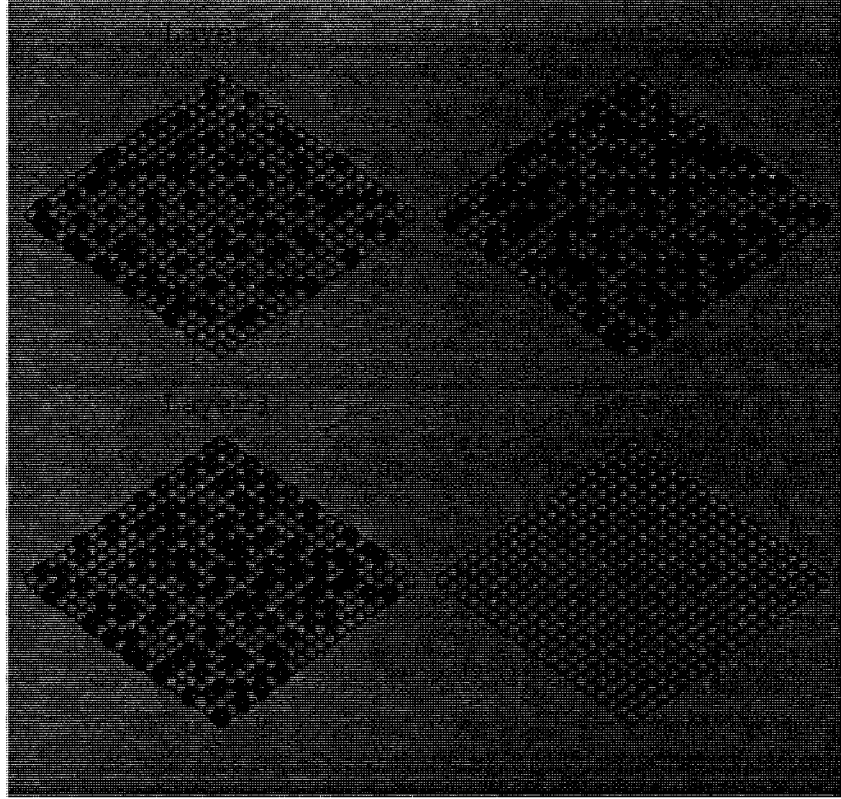
Figure 6-15: The computed equilibrium structure of an alloy with $c_1 + c_2 = 0.58$, $c_3 = 0.33$, and $\epsilon = -25$ meV. Cu atoms are shown as lighter balls, Pd atoms as darker balls.

$c_1 + c_2 = 0.58$ and $c_3 = 0.33$.

For the heterogeneous surface region near a step, we performed Monte Carlo simulations to predict the equilibrium distribution of Pd within a grand-canonical ensemble frame, a so-called constant-μVT simulation. The Pd concentration in the first two layers is determined by the chemical potential, $\Delta\mu = \mu_{Pd} - \mu_{Cu}$, where μ_{Pd} and μ_{Cu} is the chemical potential of Pd and Cu, respectively. A trial move in this simulation consists of swapping an atom from one of the first two layers of the slab with an atom from a reservoir in which the Pd chemical potential is μ (the Cu chemical potential is 0), while the third layer concentration is fixed at the experimental value. These rules effectively allow Pd to migrate between the first and

second layers of the film, but not to penetrate further into the bulk. When the physical properties of this surface slab are stable, which indicates that it is in equilibrium with the reservoir, we get average total first two-layer concentrations of $c_1 + c_2$ and simultaneously the partition of c_1 and c_2 as functions of varying c_3 and μ. By matching simulated and experimental total concentrations of $c_1 + c_2$, we get μ for each point along the scan line and c_1 and c_2 as well. Simulation results are shown as s_c_1 and s_c_2 in Figure 6-10, which agree well with the measured profiles considering this is a highly simplified model. The chemical potentials obtained for 11, 27, 36 and 50 min are -312 ± 0.4, -254 ± 0.9, -218 ± 2.1 and -172 ± 1.2 meV, respectively, and $\epsilon = -25$ meV throughout. The small deviation in chemical potentials along each scan line demonstrates that the first two layers are laterally well equilibrated and the second layer heterogeneity is caused by the heterogeneity in the third layer. The same conclusion can be reached by calculating the Helmholtz free energy from a thermodynamic integration over temperature [183], and subsequently the chemical potential by the derivative of the free energy with respect to the number of Pd atoms. Both fundamentally different methods result in almost the same chemical potential values shown in Figure 6-16. Thus we have shown that during growth, the Pd concentration in the first two surface layers is laterally equilibrated. A remarkably simple model of the energetics can therefore predict the concentration profiles over the entire surface.

6.6   Error analysis in LEEM intensity calculations

We have investigated the reliability of our results by analyzing how the agreement between the measured and computed IV curves change when c_1, c_2, and c_3 are varied. Statistical R-factor methods used in conventional LEED-IV are not applicable because of the limited energy range of the data. Instead, we focus on the residual, $|\Delta I(E)|^2$, defined as the square
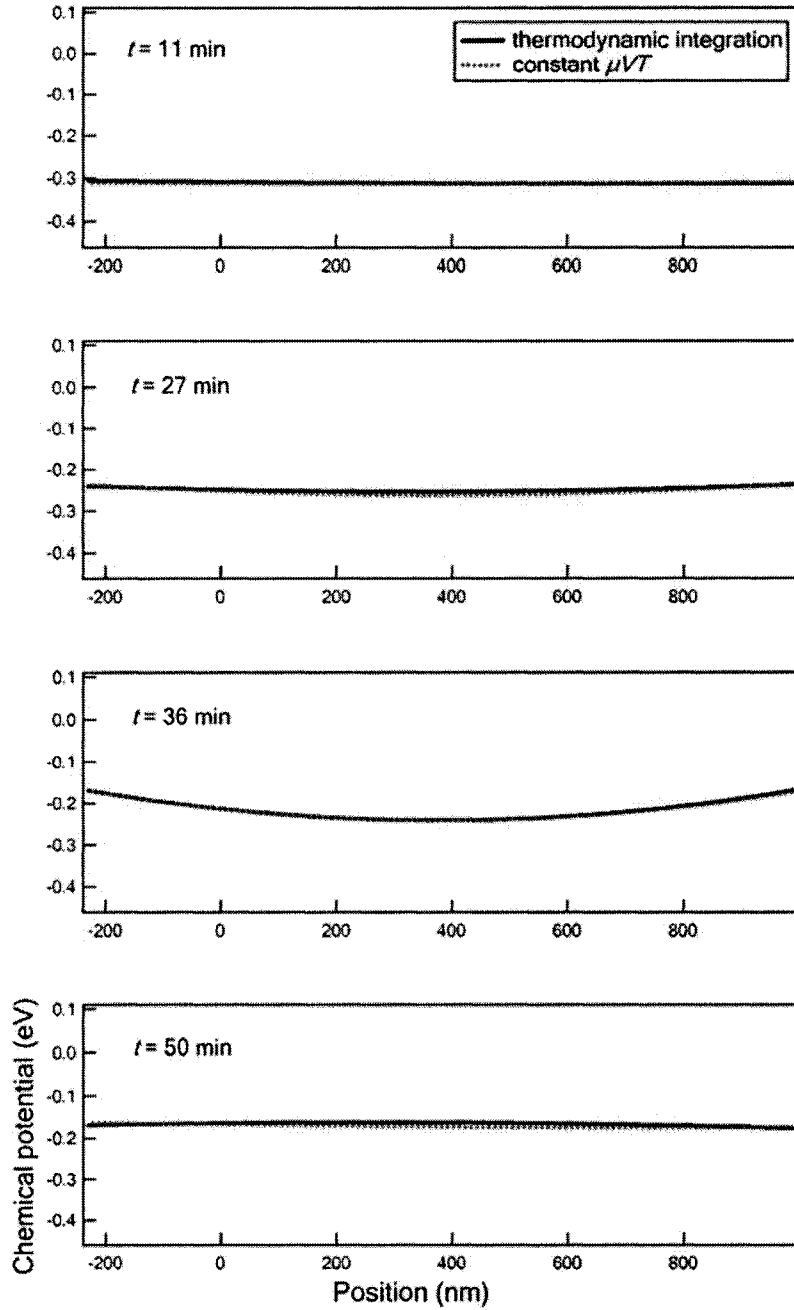
Figure 6-16: Chemical potentials for four different deposition times are obtained by two independent methods of constant-μVT simulation (dotted curves) and thermodynamic integration (solid curves).

difference between the computed and measured *IV* curves at energy E. We determine the error bars in the concentrations by varying c_1, c_2, and c_3 until the agreement between the measured and calculated *IV* curves becomes noticeably worse (examples are shown in Figure 6-17). Our definition of 'noticeably worse' corresponds to an increase in the R_2 factor of about 0.015. Using this procedure, we find that the errors in c_2 and c_3 are larger than that in c_1. Contour plots in Figure 6-17 show how the R_2 factor depends on c_2 and c_3 for three different Pd configurations, i.e. at three different points, A, B and C, on the line across a step shown in Figure 6-4 column (a). To get a more general assessment of the errors, we choose these three typical points with different ratios c_2/c_3. These three points A, B and C correspond to three positions in the line scans: 315 nm at $t = 27$ min, 660 and 315 nm at $t = 50$ min, respectively.

Three *IV* curves are shown at the bottom of each panel: the experimental (darker solid curve), best-fit computed (dotted curve), and one curve (gray solid curve) calculated at a value of c_3 that produced significantly worse agreement with the measured curve (i.e. with a larger R_2 factor). The agreement can be assessed visually by comparing the residual, $|\Delta I(E)|^2$, for the best-fit data (dotted) and worse-fit curves (solid) shown at the top of each panel. The residual for the worse-fit curve is clearly larger than that of the best-fit curve. The contour plots on the right show the dependence of the R_2 factor on c_2 and c_3 near the optimized values. The solid square marks the best-fit values of c_2 and c_3, while the solid circle indicates those of the worse-fit curve. The increment in the R_2-factor contours is 0.005. From the elongated shape of the contours, it is clear that the error in c_3 is larger than the error in c_2. The error bars for c_2 and c_3 derived using this procedure are given in Table 6.4, together with the best-fit values. Corresponding R_2 values are also listed. Following this procedure we find error bars of about $\pm$ 0.10 ML for c_2 and $\pm$ 0.15 ML for
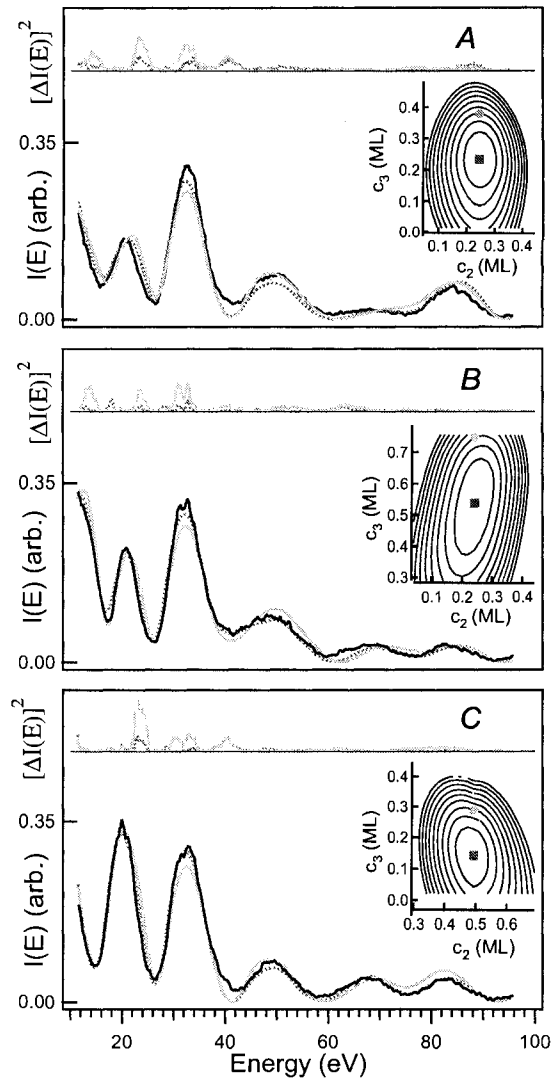
Figure 6-17: Determination of errors in c_2 and c_3. IV-curves at three positions on the line across a step (A, B, and C) are shown at the bottom of each panel. The measured curve is shown as a dark solid line, the best-fit curve is shown as dotted, and a computed curve with a worse fit is shown as a gray solid line. The residual $|\Delta I(E)|^2$ is shown on the top of each panel. The dotted ones are for best-fit data and solid curves for worse-fit data. The contour plots in the upper right corner of each panel show R_2 as a function of c_2 and c_3. The solid square indicates the values of c_2 and c_3 for the best-fit point and the solid circle marks the values for the worse fit. The increment in the R_2 contours is 0.005.

Point	Best-fit values		
	c_2 (ML)	c_3 (ML)	R_2 factor
A	0.25 ± 0.10	0.23 ± 0.15	$0.025 + 0.015$
B	0.24 ± 0.10	0.54 ± 0.21	$0.008 + 0.015$
C	0.49 ± 0.09	0.14 ± 0.15	$0.010 + 0.015$

Table 6.4: c_2, c_3 and R_2 factor with error bars at three points on the surface near a step.

c_3.

6.7 Summary and conclusions

A new technique to measure surface structure and chemical composition, with high temporal and spatial resolution, is developed by analyzing LEEM image intensities. Serving as a model system, the surface alloy of submonolayer Pd on Cu(001) substrate is prepared at 473 K. Structural and compositional information for the first three topmost layers are obtained by dynamical intensity analysis on a clean Cu(001) surface, a uniform PdCu surface alloy terrace far from the step and heterogeneous areas near steps at different deposition times. Tests on clean Cu(001) and Cu(001)-$c(2 \times 2)$-Pd present excellent agreement with previously reported results that show that the reduced dataset in LEEM-IV presents no limitation to the sensitivity of this technique. Temporal evolution of ultrathin film gives a deposition flux of about 0.9 ML/hr, close to the experimental growth rate of 1 ML/hr. Step-flow is found to be the origin of heterogeneity around steps. Monte Carlo simulations show a well equilibrated surface structure and reproduce the measured concentration profile. Most

importantly, this new technique has the unique capability to determine surface structural information with high lateral resolution of 8.5 nm. It is potentially applicable to many relevant surfaces to investigate the surface processes at nanometer scale.

CHAPTER 7

Summary and conclusions

In summary, this thesis reports on surface structure and composition determination by low-energy electron diffraction (LEED), low-energy electron microscopy (LEEM), and Monte Carlo simulations. LEED and LEEM techniques are used to measure the electron diffraction spectra and dynamical multiple scattering analysis is performed to optimize the surface structural and non-structural parameters via comparing experimental and calculated data. The results are summarized below for four surface systems studied.

The (111), (110) and (001) surfaces of the semimetal Bi are investigated with LEED. All of their atomic geometry are determined by the intensity analysis. The unreconstructed (1×1) structure is found for all three surfaces. The surface interlayer relaxations determined by LEED agree with those by first-principles calculations. The surface Debye temperatures for both Bi(111) and Bi(110) are found to be lower than that of the Bi bulk. The STM observation on the Bi(001) surface shows that bilayer steps dominate on the surface and no single layer steps exist.

LEEM-*IV* study on Pd ultra thin films on the substrate Cu(001) includes the temporal evolution of Pd concentrations on the uniform Cu(001) terrace and heterogeneous areas around advancing steps. It is found that, at the initial deposition stages, Pd atoms reside in the second layer at the sample temperature of 473 K, and the Pd concentration increases exponentially with time. The heterogeneous structure and composition near steps

are found to be a result of step overgrowth. In this study, we have successfully developed the LEEM-*IV* technique to achieve a nanometer scale resolution of the surface structure and composition. Specifically, we have demonstrated a 3D profile of Pd concentrations in the 3 topmost layers at the resolution of 8.5 nm. This technique is potentially useful in relevant surface technologies.

Studies on the Si(001) surface and 6H-SiC(0001) surface are presented in Appendix A and B, respectively.

The reconstructed 2×1 geometry in the Si(001) surface has been refined by a single domain electron diffraction with the LEEM facility. This single domain diffraction eliminates uncertainties about the size ratio of possible multiple domains and simplifies the calculations. This dataset is potentially a more reliable and definite determination of this surface structure. The results give a tilted asymmetric dimer structure.

The 6H-SiC(0001) surface phase transition and the surface phase structures have been investigated. LEEM diffraction data from a large single domain are analyzed for 3×3, 1×1 and $\sqrt{3}\times\sqrt{3}$ phases. Results obtained so far show good agreement between experimental and theoretical data. All the surface structures turn out to have an "A" bi-layer bulk termination. It is found that the amount of Si at the surface decreases with increasing temperature. Adatom-trimer-adlayer model for the 3×3 surface does not give a satisfactory result and more work needs to be done to resolve this structure. A mixed Si-vacancy top-site overlayer on 1×1 surface is found. A $\sqrt{3}\times\sqrt{3}$ overlayer at the T4 registry on the substrate surface generates a best fit between experimental and calculated data.

Appendix A

Si(001)-(2×1) surface

A.1 Introduction

Si is one of the most important materials used in the modern semiconductor industry. The performance of electronic devices based on the Si surfaces is definitely influenced by these surfaces. The knowledge of atomic structures of these surfaces is of fundamental significance in order to understand the surfaces or interfaces properties. One of these surfaces, Si(001)-(2×1), has drawn lasting research interest since the late 1970s for its structure determination. Numerous studies supported a 2×1 dimer structure on the surface which reduces the number of dangling bonds per surface atom from two in the bulk-terminated surface to one in the reconstructed structure [184, 185, 186, 187, 188, 189, 190, 191]. Many studies indicated that the dimer is asymmetric and buckled [184, 188, 192, 193, 190, 194]. The dimer structure will be shown in the Section A.3.2. Although many measurements and possible models have been tried in the LEED experiments [195, 196, 197, 198, 199, 200, 201], the results obtained so far are not very satisfactory, since the agreement between experimental and calculated LEED *IV* curves is not very convincing. One issue of concern is the availability of high quality samples. The other issue is whether the real surface structure is correctly modeled. The dimer structure is, however, still conceived as being dynamically or statically asymmetric [189, 202]. More powerful and effective measuring techniques are

149

needed to unravel the real structure.

This work is aimed at resolving this surface geometry by using the low energy electron microscopy (LEEM) technique. The LEEM is switched to the LEED mode by removing the aperture in the back-focal plane of the objective lens. A small size electron beam is incident upon a single domain of the Si(001)-(2×1) surface. The single domain diffraction will simplify the dynamical LEED calculations, and more importantly, it will give a more reliable determination of the surface structure by eliminating the uncertainty about the ratio of multiple domain sizes. The results presented here should be regarded as "a work in progress" and the results are not finalized.

A.2   Methods

The LEEM is used to record the electron diffraction *IV* curves. One of the LEEM's advantages over the conventional LEED technique is that the LEEM provides a possibility of illuminating a local surface area, or a single domain. In our experiment, a controlled small size of electron beam is incident upon a single domain of Si(001)-(2×1). This working mode is sometimes called microdiffraction mode. The *IV* spectra can be extracted from a series of diffraction patterns recorded at different incident electron energies. All the measurements are done at the sample temperature of 373 K. This technique has been utilized to refine the surface structure of a single domain of Ru(0001) [203].

Dynamical LEED intensity simulations are performed for trial surface structures. By comparing the calculated and measured spectra, the best-fit trial structure is taken as the true structure. A full-dynamical LEED program is used for the LEED intensity analysis [204, 205, 206, 207, 208]. The quality of the fit of calculated to experimental data is evaluated by the reliability factors R_P. In all calculations, a 2D lattice constant of 3.84

Table A.1: The values of the real part V_0 and the imaginary part V_i of the inner potential against the kinetic energy E of the incident electrons.

E (eV)	25.00	30.00	35.00	40.00	45.00	50.00	55.00	60.00	65.00	70.00	75.00
V_0 (eV)	-10.08	-10.08	-10.08	-9.82	-9.33	-8.90	-8.53	-8.20	-7.91	-7.64	-7.40
V_i (eV)	2.09	2.44	2.77	3.06	3.31	3.51	3.66	3.69	3.72	3.74	3.76
80.00	85.00	90.00	95.00	100.00	105.00	110.00	115.00	120.00	125.00	130.00	135.00
-7.18	-6.97	-6.79	-6.61	-6.45	-6.30	-6.16	-6.03	-5.90	-5.79	-5.68	-5.57
3.77	3.78	3.79	3.80	3.80	3.80	3.80	3.80	3.80	3.79	3.79	3.78

Å is used and a Debye temperature of 640 K is used for the bulk layers. The following factors are checked: the depth of the relaxation, the influence of phase shifts, and the influence of coherent and incoherent domain mixing. The complex inner potential is assumed to be energy dependent from the Rundgren's phase shift program [209] . The real part is $V_0 = max(0.26 - 69.69/\sqrt{E + 7.84}, -10.08)$ eV, where E is the kinetic energy of the incident electrons. The imaginary part V_i is numerically calculated from mean free path measurements and it varies from 2.09 to 3.78 eV as the electron energy increases from 25 to 135 eV [210, 209, 208]. The values of the inner potentials are given in Table A.1.

A.3   Results and discussion

Previous studies on the Si(001) surface show a coexistence of (2×1) and (1×2) domains which are rotated by 90° from each other. In our experiments, fractional-order beams only appear along one integral-order beam axis – (1, 0) beam axis, but not on its perpendicular axis – (0, 1) beam axis. A schematic LEED pattern is shown in Figure A-1. There is (1/2, 0) beam but no (0, 1/2) beam. This suggests that only a single domain on the Si(001) surface is analyzed. One more feature is the 2 mirror-plane symmetry of the diffration pattern, which is suggestive of symmetric dimerizing or averaged asymmetric dimerizing at the surface.

(0, 1)

(0, 0) (1/2, 0) (1, 0)
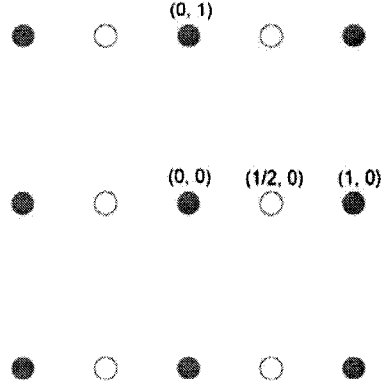
Figure A-1: A schematic LEED pattern for the single domain Si(001)-(2×1). Solid spots represent the integral-order beams and hollow spots the fractional-order beams. Beams (0, 0), (1, 0), (0, 1) and (1/2, 0) are labeled. Note that that is no (0, 1/2) beam.

A.3.1 Comparison with LEED data

We compare the single-domain LEEM *IV* curves with the latest reported LEED data from the Institute of Crystallography at the University of Munich (ICM) [200]. Figure A-2 shows all the LEEM beams and some beams in the ICM dataset. Because of the unavailability of the (0, 0) beam in the ICM dataset, this beam is not compared. Beams under comparison include the integral-order beams (1, 0), (0, 1), (1, 1), (0, 2), (2, 0) and the fractional-order beams (1/2, 0), (1/2, 1), (3/2, 0), (3/2, 1). Note that the beams (1, 0) and (0, 1) are averaged and compared with the beam (1, 0) in the ICM dataset, and the same for beams (2, 0) and (0, 2). For a better visualization of comparison, the LEEM intensities are all multiplied by a factor of 3.

For a surface with coexistent Si(001)-(1×2) and Si(001)-(2×1) domains, the diffraction pattern from the (1×2) domain is just a rotation of the diffraction pattern from the (2×1) domain by 90°. The rotation makes beams (1, 0) and (0, 1) equivalent in intensities, and it is the same for (2, 0) and (0, 2). This is the situation happening in the conventional
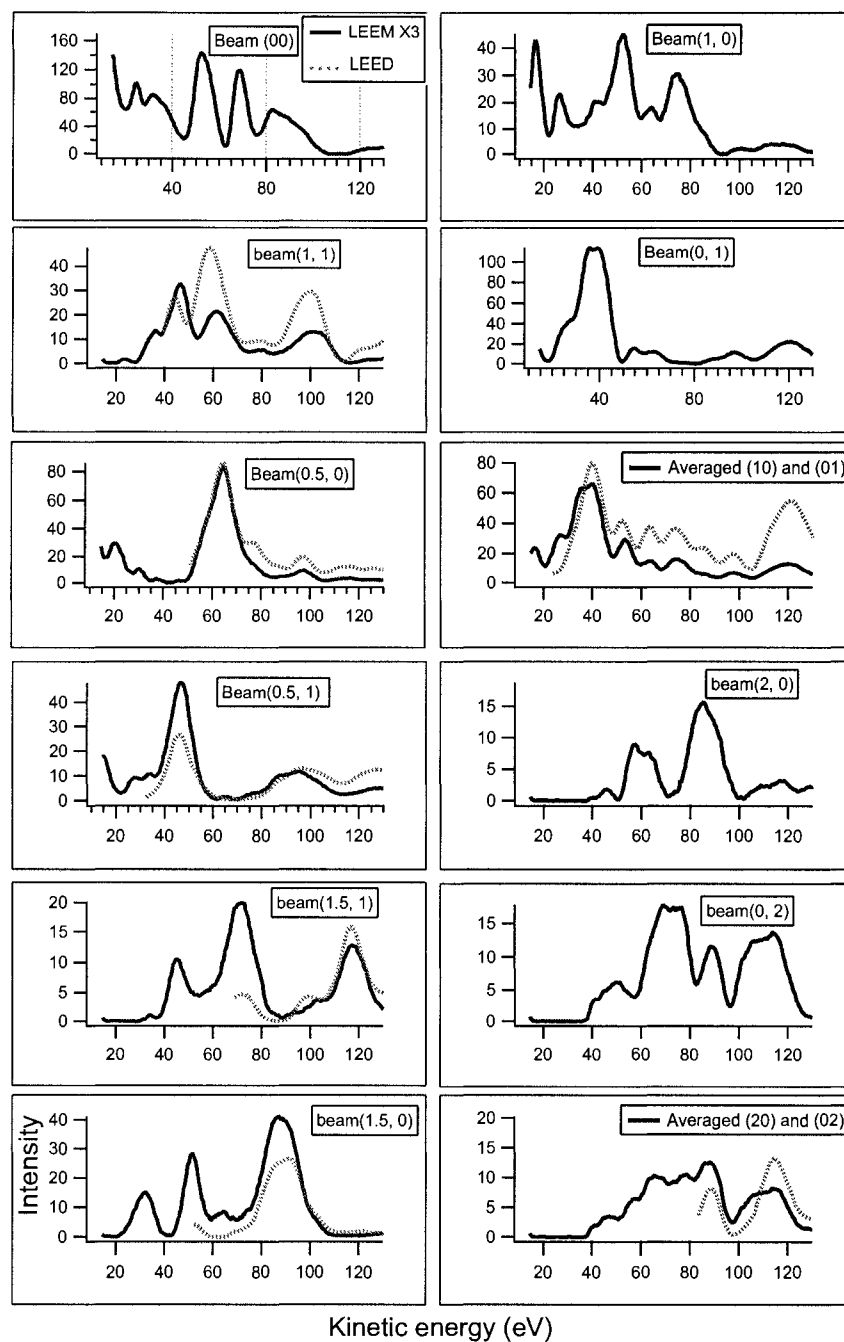
Figure A-2: Comparison of the LEEM experimental data (solid) with the ICM data (dotted). Beam (0, 0) is not compared due to its unavailability in the ICM dataset. Averaged beams (1, 0) and (2, 0) in the ICM dataset are compared with averaged (1, 0) and (0, 1), and averaged (2, 0) and (0, 2) in the LEEM dataset, respectively.

153

LEED technique where the diffracted intensities are contributed from a large surface area containing both domains. Consequently, these equivalent beams are averaged for data analysis. It is noteworthy that each of these beams is contributed by both domains, but the equivalence between the beams (1/2, 0) and (0, 1/2) are different. The beams (1/2, 0) and (0, 1/2) are due to different individual domains and the equivalence in intensities relies only on the same domain sizes. In the ICM LEED dataset, beam (1, 0) is an average of beams (1, 0) and (0, 1), and beam (2, 0) an average of beams (2, 0) and (0, 2). The following gives a summary in comparison.

All the compared beams show an overall moderate match between the ICM data and the LEEM data. But there are some differences listed below.

- LEEM has the specular beam (0, 0) which is a dominant beam in intensity while ICM dataset has no (0, 0) beam.

- LEEM IVs have more spectra sturctures at low energies while the ICM dataset has more structures at high energies.

- Due to the single domain diffraction in LEEM, the (1, 0) and (0, 1), (2, 0) and (0, 2) beams are apparently different. But in the ICM data, they are equivalent and averaged, respectively.

- Some curves show different relative peak intensities between the LEEM and ICM data. One example is the peaks in the beam (1, 1). In the LEEM data, the peak at around 60 eV is weaker than that at around 45 eV, but in the ICM dataset, it is the reverse.

Based on the above comparison, we can see evident differences between the LEEM and ICM data although overall the curves are similar to each other. LEEM IVs do offer some

spectra structures which ICM does not have. With these characteristics, the LEEM data potentially promise a definite and more reliable determination of the surface structure.

A.3.2 Calculation results and discussions

The Si bulk has a well-known diamond structure. One conventional unit cell is shown in Figure A-3 (a). The lattice vector length of 5.43 Å and the Si-Si bond length of 2.35 Å are indicated. The top view of the bulk-terminated (001) surface is shown in Figure A-3 (b). The numbers in (b) indicate the atom height in the four topmost layers. The value is a fraction of the lattice vector length in the [001] direction.

In the dynamical LEED analysis, different energy ranges have been tried for isotropic and anisotropic atomic vibrations, respectively. The corresponding R_p factors are listed in Table A.2. The agreement is significantly worse for the low energy range below 40 eV than for the high energy range. This may be for the following reasons: (a) at low energies the mean free path increases and this is not correctly included in the theory, (b) the form of the inner potential is probably incorrect at low energies, and (c) the phase shifts are not appropriately calculated. In the potential calculation the Slater-approximation is used for the exchange and correlation term, which is good for high energies, but not for energies near the Fermi level. Also inelastic interactions, such as plasmon excitations and resonance effects, may be important but are not explicitly considered in the theory. In LEED calculations usually energies above 30 - 50 eV are used; we therefore use energies above 30 eV for the time being. The results show a significantly better R factor for the higher energy range, and this is also visible in the plot of the IV curves. The structural results, however, are nearly the same.

For the isotropic simulations, the optimized surface atomic geometry is shown in Fig-
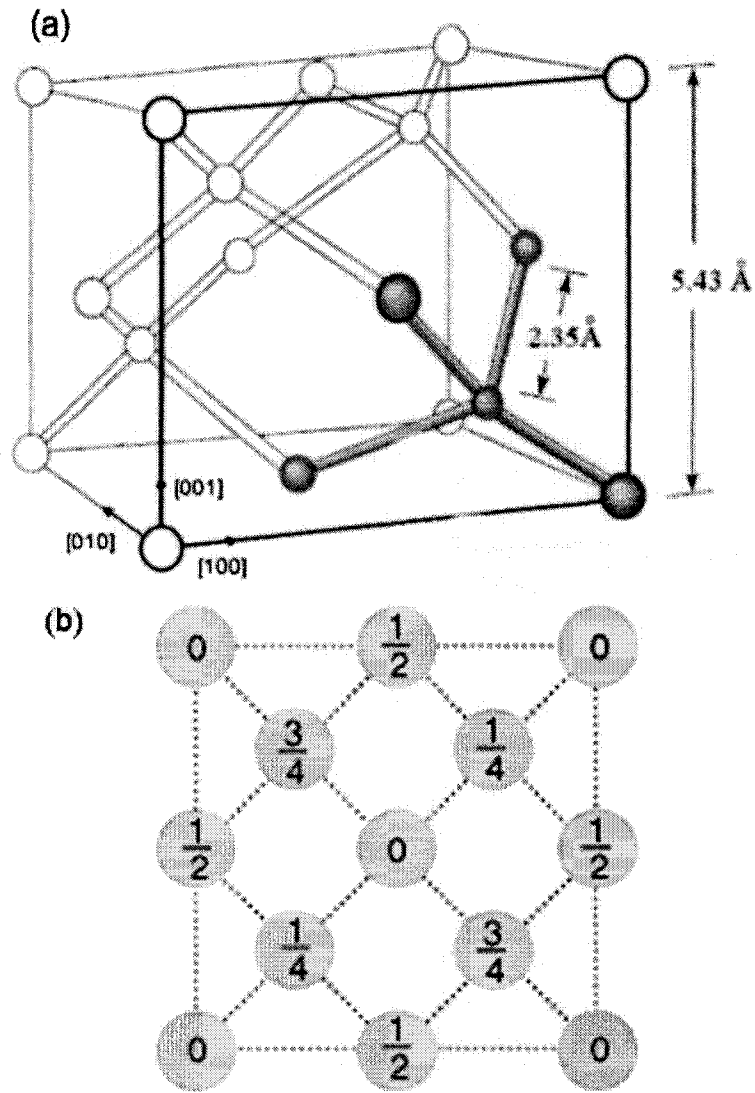
Figure A-3: Si crystal structure. (a) One conventional unit cell of the Si crystal. (b) The top view along the [001] direction. The numbers indicate the atom height in the four topmost layers. The value is a fraction of the lattice vector length in the [001] direction.

Table A.2: R_P values for isotropic and anisotropic vibrations in two different energy ranges.

	R_P, 10~130.5 eV	R_P, 30~130.5 eV
isotropic vibrations	0.40	0.33
anisotropic vibrations	0.39	0.27

ure A-4. It is a top view of the (001) surface and a side view from the $[1\bar{1}0]$ perspective. The positions of the atoms in the first five layers are optimized. Each layer is divided into two (2×1) sublattices, so there are ten sublattices. Ten atoms in these ten sublattice unit cells are labelled by the numbers 1 through 10; see Figure A-4. The x, y, and z axes are set in the [110], $[1\bar{1}0]$ and [001] directions, respectively. The optimized coordinates are given in Table A.3. From Figure A-4, we see that the atoms 1 and 2 displace much in the [110] direction resulting in a dimer structure. The difference in the vertical shifts between atoms 1 and 2 leads to a tilting bond between them. The bond length is about 2.2 Å, a bit shorter than the NN Si distance of 2.35 Å in the Si bulk. The dimer height is about 0.6~0.7 Å. The atoms in the third and fourth layers underneath the dimer are shifted into the crystal by about 0.3~0.35 Å. These are the main features which will remain though the error bars are certainly large at the moment. The experimental and calculated IV curves are compared in Figure A-5. It shows a good overall agreement with most peaks' positions and intensities matched between the experimental and calculated results.

However, some significant features of the experimental data cannot be fitted, i.e. the height of the peak of the (0, 0) beam at 55 eV, the position of the peak of the (1, 1) beam at 45 eV, and the height of the peaks of the (0, 2) beam. The reason for the misfit is not clear.

One possible cause may be a flip of the dimers, instead of a thermal vibration, as proposed by total energy calculations. Such a flip would correspond to a coherent superposition of domains with asymmetric dimers. This has been checked as well, but did not lead to an improvement.

The results shown above are obtained with incoherent superposition of asymmetric dimers. A coherent superposition would mean that the domains are coherently flipping,
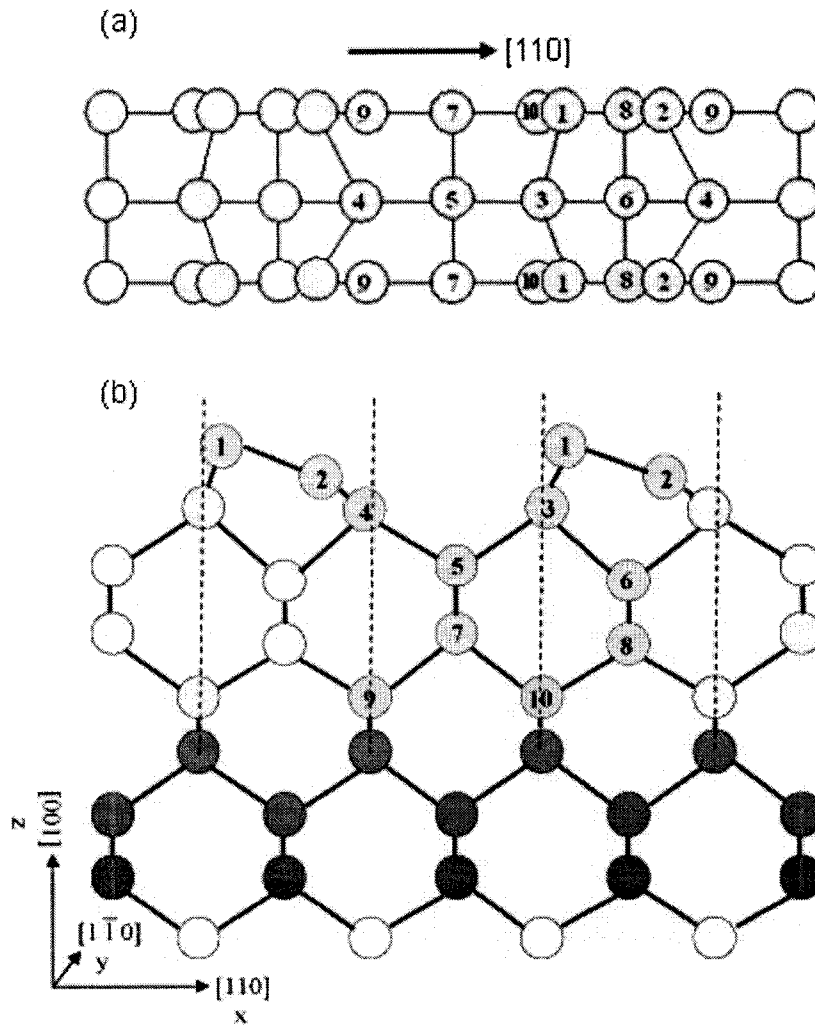
Figure A-4: The dimer structure on Si(001). Each of the five topmost layers is divided into two (2×1) sublattices, so there are ten sublattices. Ten atoms in all ten sublattice unit cells are labelled by the numbers 1 through 10. The x, y, z axes are chosen in the [110], [1$\bar{1}$0] and [001] directions, respectively. The displacements of the atoms 1 and 2 in the [110] direction leads to a dimer bond, and the vertical displacements of them leads to a tilting bond. The solid lines indicate the Si-Si bonds. (a) The top view. (b) The side view from the [1$\bar{1}$0] direction.
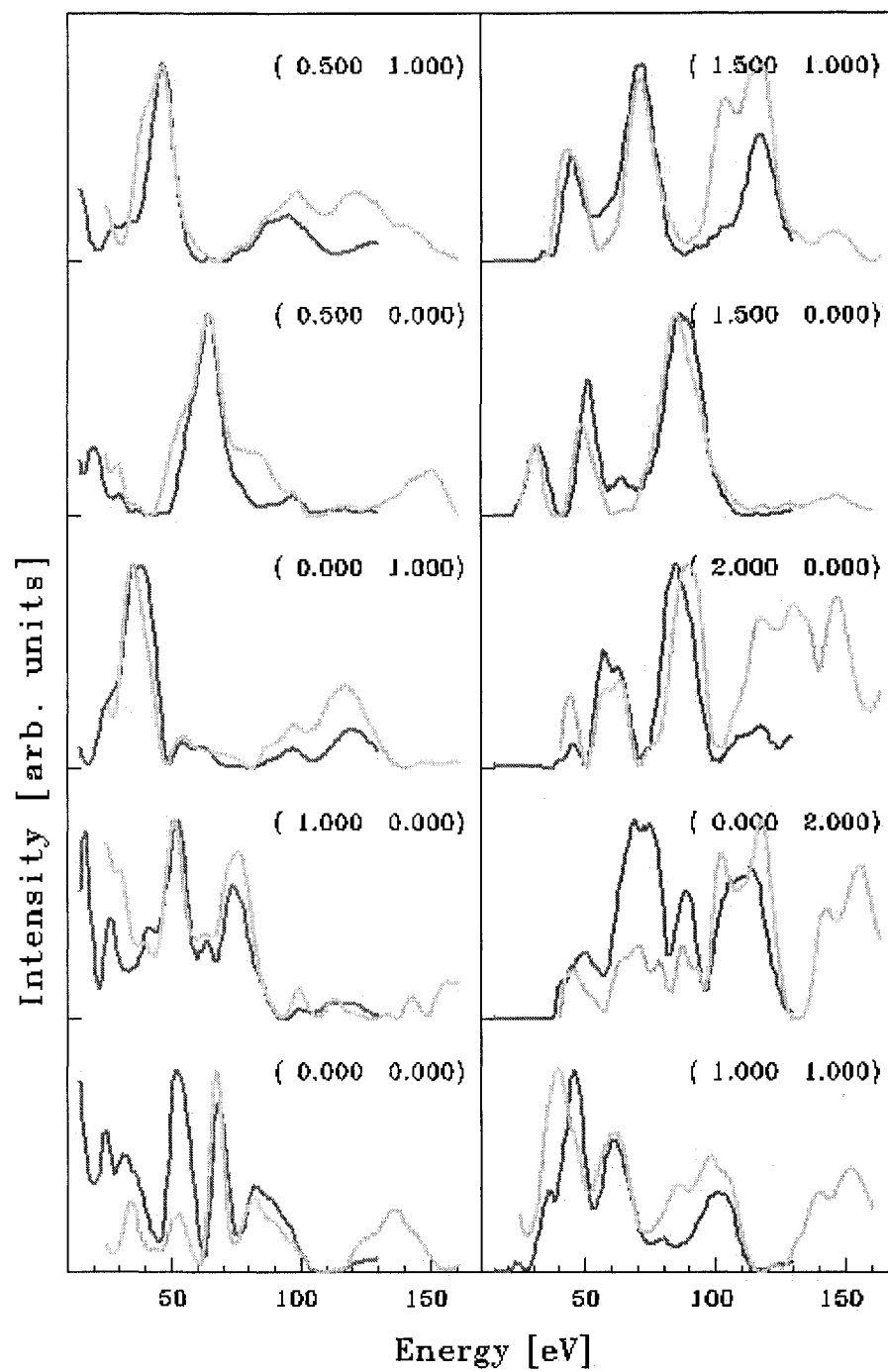
Figure A-5: Comparison of the experimental *IV* curves with those from isotropic vibrations calculations. Experimental data are shown in gray (green in color) and calculated in dark (pink in color). Energy range: 30~130 eV. $R_P = 0.33$.

Table A.3: Optimized coordinates of ten atoms in the topmost ten sublattice unit cells.

Atom No.	x (Å)	y (Å)	z (Å)
1	2.727	1.920	0.000
2	-2.886	1.920	0.695
3	2.059	0.000	1.419
4	-2.122	0.000	1.461
5	0.038	0.000	2.648
6	-3.814	0.000	3.026
7	0.022	1.920	4.061
8	-3.801	1.920	4.341
9	1.868	1.920	5.514
10	-1.871	1.920	5.587

which is not realistic either. A further possibility is the assumption of a single domain with randomly distributed asymmetric domains. These calculations will be tried.

For the anisotropic vibration simulations, more layers are required to be optimized to get a better agreement. Considering the error bars, the results need more evaluation right now to determine their reliability although the agreement is better than the isotropic simulations.

The optical potential has some influence on the height of the peaks at low energies. Different optical potentials are worth trying to see the influence of this parameter.

A.4 Summary

The Si(001)-(2×1) surface structure has been refined with a single domain electron diffraction by LEEM. The results show aysmmetric dimers. Current results are still under way to be finalized.

APPENDIX B

6H-SiC(0001) surface phases

B.1 Introduction

Silicon carbide (SiC) is known for its remarkable properties such as a wide band gap, high thermal conductivity, high thermal stability, and extreme hardness [211]. Structurally, the SiC compound is interesting for its various polytypes. All polytypes differ in the stacking sequence of the Si-C bi-layer structure. The most studied polytypes are 3C-SiC, 2H-SiC, 4H-SiC, and 6H-SiC. The initial numbers denote the numbers of bi-layers in their corresponding primitive unit cells and C, H means cubic, hexagonal structures, respectively. With A, B, C standing for three Si-C bi-layers which register in the same way the three repeated stacking layers in an fcc crystal do, the repeated stacking units for the above four crystals are correspondingly ABC, AB, ABCB, and ABCACB. Note that the two neighboring atomic planes between two consecutive bi-layers have the same registry.

Since different polytypes have different band gap widths, it is possible to engineer the stacking sequence to get a desirable band gap. However, it is unknown what guides the stacking sequence and what is the role of the surface in the crystal growth. The surface structure information available so far is not adequate for controlling the stacking sequence. Moreover, SiC has become very interesting recently as an ideal platform to grow heterogeneous catalysts and a single graphite sheet [212]. The knowledge of the surface structures

is definitely crucial to understand the surface processes governing the thin films' growth.

In this work, we particularly focus on the 6H-SiC(0001) surface. This bulk-terminated surface structure is shown in Figure B-1. The bulk can be built with repeated stacking of the ABCACB unit. Each layer has a 2D hexagonal structure. This Si-terminated surface exhibits different surface structures at different annealing temperatures [213]. Around 800°C, it is an unreconstructed (1×1) bulk-like structure. Annealed at 900°C, the surface becomes a (3×3) reconstructed structure. At 1050°C, the (3×3) superlattice forms. Up to 1300°C, the LEED diffraction shows a $(6\sqrt{3} \times 6\sqrt{3})$ pattern. At 1400°C, the (1× 1) graphite ultra thin films are obtained on the surface. Our goal is to resolve the surface structural and compositional evolution during the phase transition, and ultimately, unravel the growth mechanism of graphene on this surface. The following sections present some results obtained so far.

B.2 Surface phase transitions

The phase transition of the 6H-SiC(0001) surface upon heat treatment has been observed by LEEM. Bright and dark fields imaging demonstrates a direct *in situ* observation of the surface phase evolution, transitions in a sequence of 1×1, 3×3, 1×1, $\sqrt{3}\times\sqrt{3}$, $6\sqrt{3}\times6\sqrt{3}$ and the graphene phase due to gradually increased temperature. With an introduction of a small amount of disilane $((Si_2H_6)$ into the UHV chamber at the annealing temperature of 850°C, a 3×3 LEED pattern is displayed. As the temperature is escalated to 900°C, a 1×1 LEED pattern appears. The 1×1 pattern becomes a 3×3 pattern upon decreasing temperature and a $\sqrt{3}\times\sqrt{3}$ pattern upon increasing temperature to 1050°C. Therefore, the 3×3 to 1×1 transition is reversible. The sharp LEED patterns for these three phases are shown in Figure B-2.
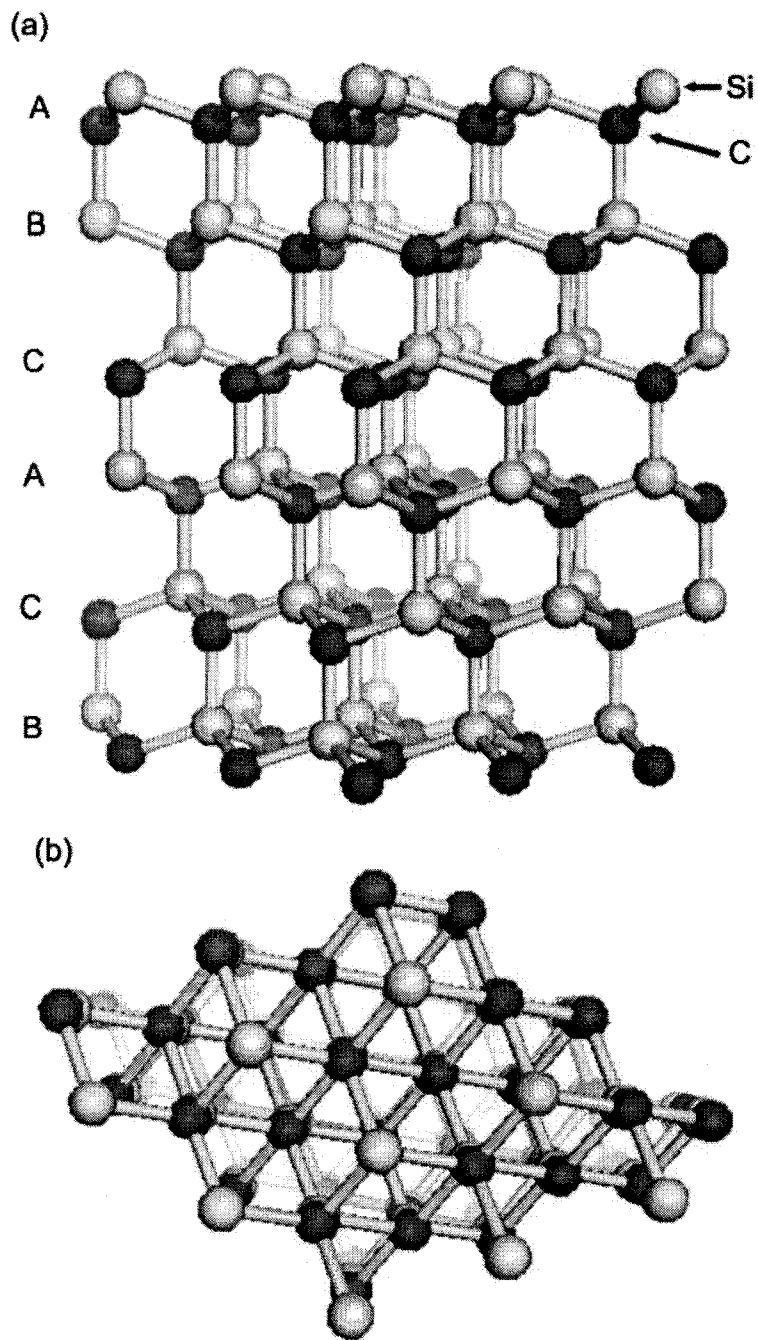
Figure B-1: Bulk-terminated 6H-SiC(0001) surface. (a) The side view. The bi-layer stacking

sequence is ABCACB in one unit cell. (b) The top view. It is a hexagonal 2D lattice in each layer.

(a) 3x3 LEED pattern

(b) 1x1 LEED pattern
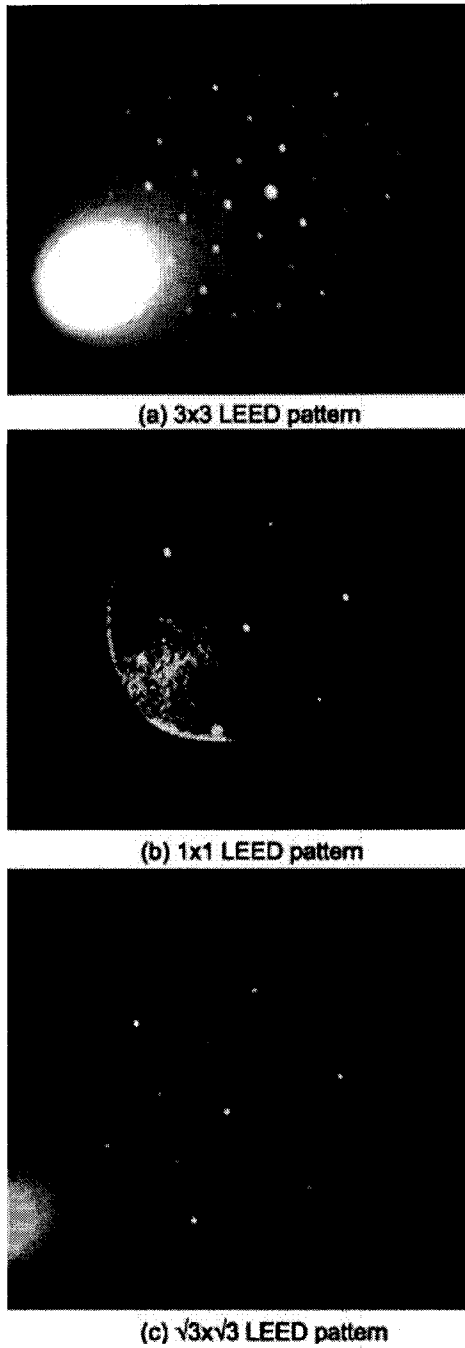
(c) √3x√3 LEED pattern

Figure B-2: LEED patterns for the 6H-SiC(0001) surfaces at different annealing temperatures. The bright background is due to the deflected inelastically scattered electrons. It is deducted in the intensity extraction. (a) The LEED pattern at $E_k = 50$ eV for the 3×3 reconstruction at 850°C. (b) The LEED pattern at $E_k = 37$ eV for the 1×1 structure at 900°C. (c) The LEED pattern at E_k = 50 eV for the $\sqrt{3} \times \sqrt{3}$ reconstruction at 1050°C.
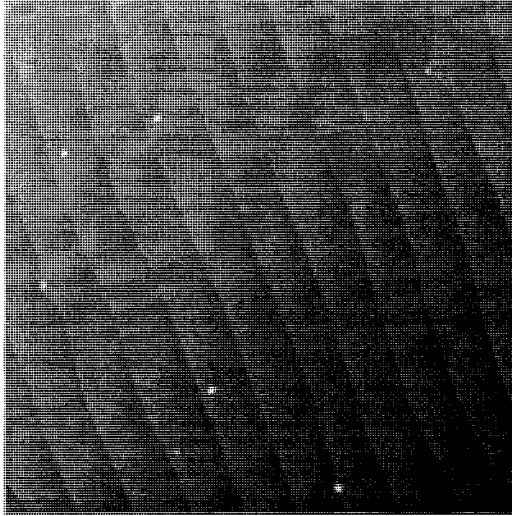
Figure B-3: An AFM image of the 6H-SiC(0001) surface. All the steps are the same triple bi-layer height, i.e. ~ 8 Å. Image size: 3×3 μm^2.

The LEEM bright and dark-field images have shown wide terraces on the surfaces. It is found that all the steps are the same triple bi-layers height of ~ 8 Å. An atomic force microscopy (AFM) picture of the surface is shown in Figure B-3. The availability of wide terraces allows for electron scattering in a single-domain. The corresponding diffraction IV spectra can be used to determine the surface structure and chemical stoichiometry. In all LEEM IV measurements, the same diffraction area has been used. Quantitative dynamical analyses of the LEEM-IV curves are performed to resolve the bulk termination and the surface overlayer structures.

B.3   3×3 reconstruction

When annealed at around 850°C at an ambient of the disilane gas, the 6H-SiC(0001) surface reconstructs into a (3×3) structure. The disilane is used as a Si source for the Si-rich 3×3 structure. A model for the 3×3 reconstruction proposed by Schardt *et al.* [214] is shown

in Figure B-4. In one 3×3 superlattice unit cell, there are three Si overlayers including one adlayer, one trimer layer and one adatom layer on the Si-C bulk bilayer.

We have tried this model for the 3×3 structure in our experiment. By dynamical *IV* analysis, a moderate level of agreement between the experimental and calculated data is reached. The comparison of experimental and calculated *IV* curves is shown in Figure B-5. Some beams fit well but others do not. This could be caused by the incorrect surface modeling. It is possible to get different surface structures with different experimental procedures. Another possibility is that a certain amount of defects could exist on the terrace affecting the measuring results. High quality sample surfaces will be prepared for new measurements. In the analysis, the "A" termination of the bulk proves to give a better agreement than "B" or "C" termination.

B.4   1×1 structure

When one increases the annealing temperature to 900°C, the 6H-SiC(0001)-3×3 surface becomes a 1×1 structure indicated by the LEED pattern. Various models have been tried for this surface. A best agreement between the experimental and calculated data is given by a Si overlayer model. This model is schematically shown in Figure B-6. In this model, a Si adlayer sits on the "A" bi-layer terminated surface. Furthermore, averaged *t*-matrix calculations for the mixed Si and vacancy overlayer model show a considerable amount of vacancies in the Si adlayer. So the overlayer is not one monolayer of Si. When the sample temperature is increased, some Si atoms in the 3×3 structure evaporate leaving the surface. Depending on how much Si is left on the surface, the overlayer could have only a submonolayer of Si.

The comparison of experimental and calculated *IV* curves is shown in Figure B-7. Over-

(a)

Adatom

trimer

adatom layer

Si-C bilayer

(b)

Figure B-4: 3×3 reconstruction of the 6H-SiC(0001) surface. (a) The side view. Above the Si-C bilayer in the bulk-terminated surface, three Si overlayers reconstructed. They are one adatom layer, a trimer and an adatom in one 3×3 unit cell. (b) The top view of the reconstruction. The large 3×3 unit cell is shown.
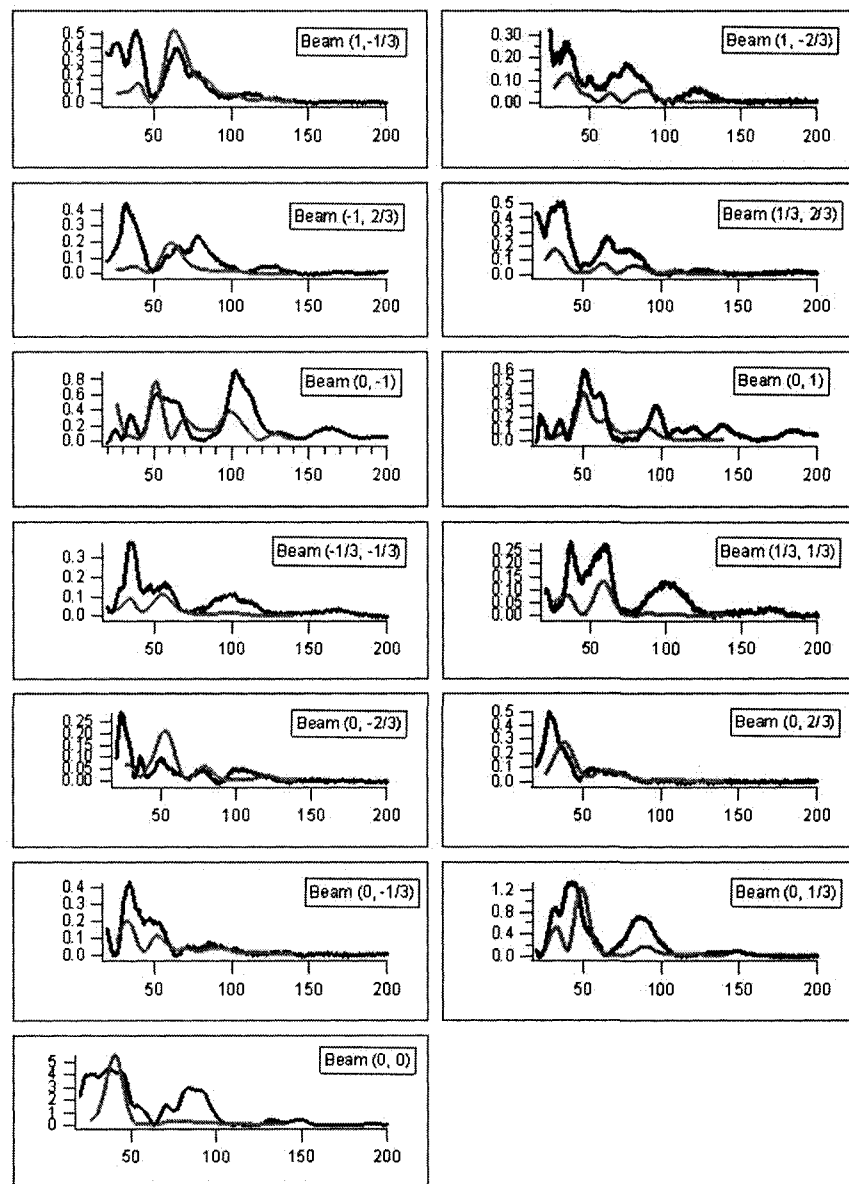
Figure B-5: Comparison of experimental (black) and calculated (gray) *IV* curves for the 6H-SiC(0001)-3×3 surface.
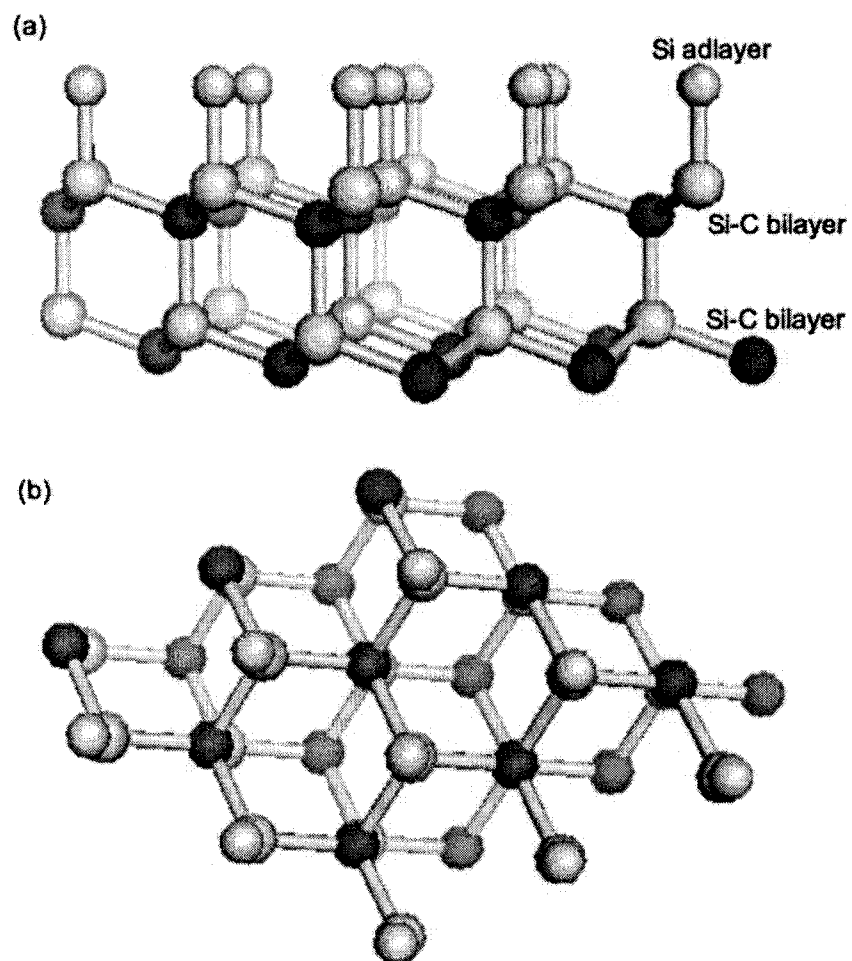
Figure B-6: 6H-SiC(0001)-1×1 surface structure. (a) The side view. Above the two Si-C bilayers in the bulk-terminated surface, one Si overlayer is adsorbed on the top cite. (b) The top view of this surface.

all, there's a good agreement except for the very low energy part. Energy-dependent inner potential has been tried. The real part of inner potential does not improve the fit significantly while the the imaginary part does. The imaginary part of the inner potential is in the form of $E^{1/3}$.

B.5 $\sqrt{3} \times \sqrt{3}$ reconstruction

When the annealing temperature is increased to about 1050°C, a sharp $\sqrt{3} \times \sqrt{3}$ LEED pattern is displayed. Since this surface is the result of the transition from the 1×1 structure, it is natural to model this surface as a $\sqrt{3} \times \sqrt{3}$ overlayer on the bulk-terminated surface. The following possibilities are tried: Si or C overlayer and the registry of the overlayer. It turns out that the a Si overlayer on the T4 site of the underneath "A" bilayer terminated surface gives a best fit between experimental and calculated data. That is, the atoms in the overlayer are situated above the C atoms in the first Si-C bilayer. Figure B-8 shows this model and Figure B-9 shows the *IV* curves. We can see a very good agreement in the *IV* curves obtained. All the previous LEED *IV* work [215] is based on a multi-domain model which can bring more optimization parameters and larger error in the optimized results.

B.6 Summary and conclusions

In our study of the 6H-SiC(0001) surface phase transition, single domain data have been acquired. For all the surface structures, "A" bi-layer bulk termination proves to give better agreements between experimental and calculated *IV* curves. It is found that the amount of Si at the surface decreases with increased temperature. Adatom-trimer-adlayer model for the 3×3 surface does not give a satisfactory result and more work need to be done to
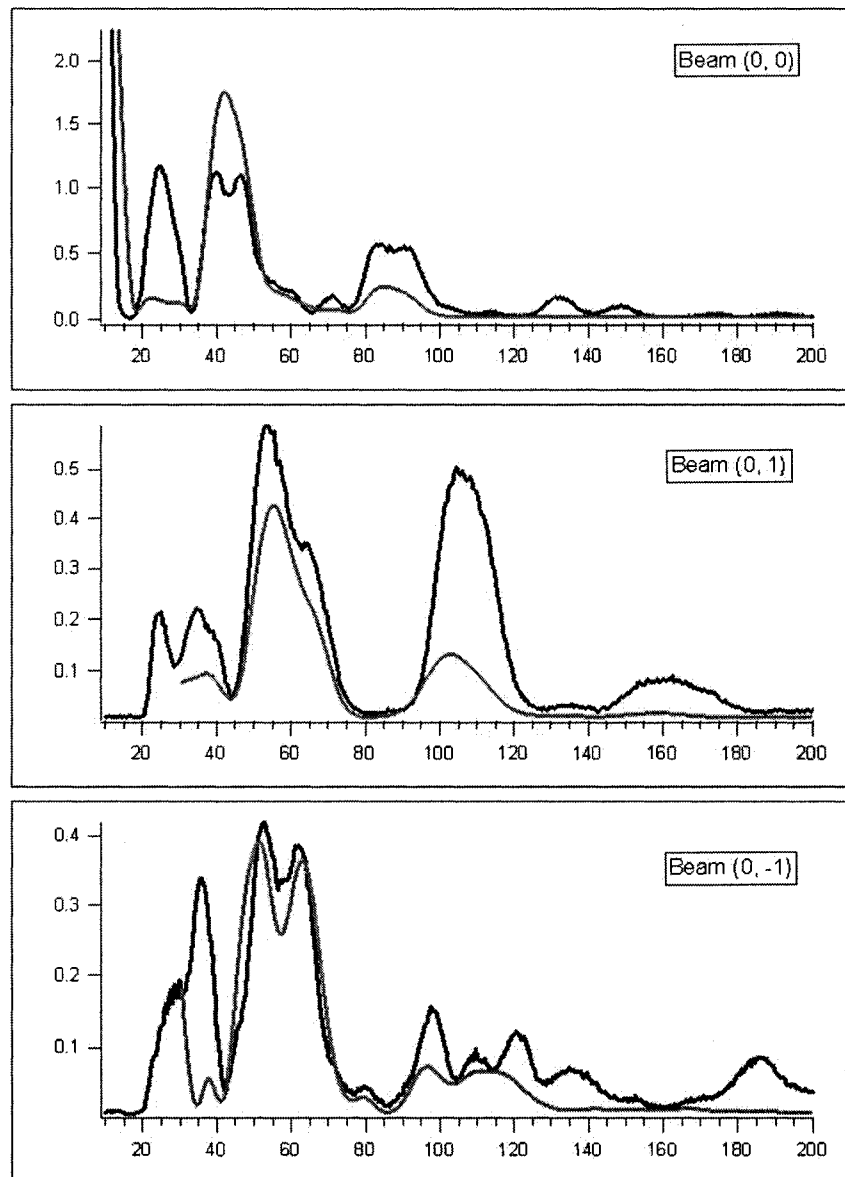
Figure B-7: Comparison of experimental (black) and calculated (gray) *IV* curves for the 6H-SiC(0001)-1×1 surface.

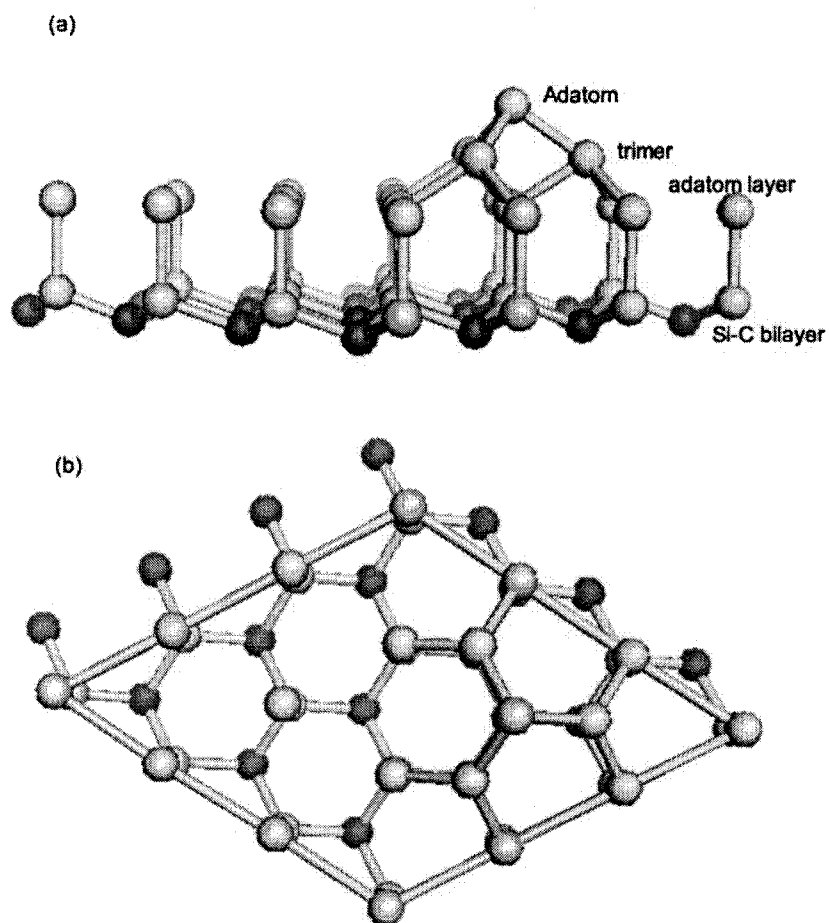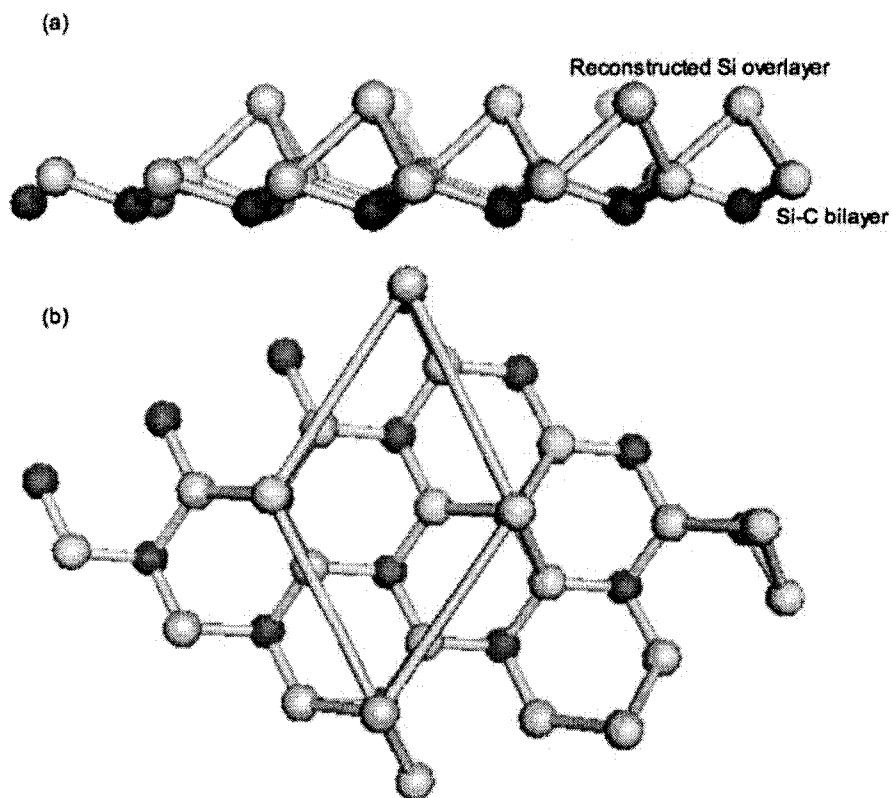Figure B-8: $\sqrt{3}\times\sqrt{3}$ reconstruction of the 6H-SiC(0001) surface. (a) The side view. Above the Si-C bilayer in the bulk-terminated surface, there is a reconstructed $\sqrt{3}\times\sqrt{3}$ Si overlayer. (b) The top view of the reconstruction and the $\sqrt{3}\times\sqrt{3}$ unit cell.
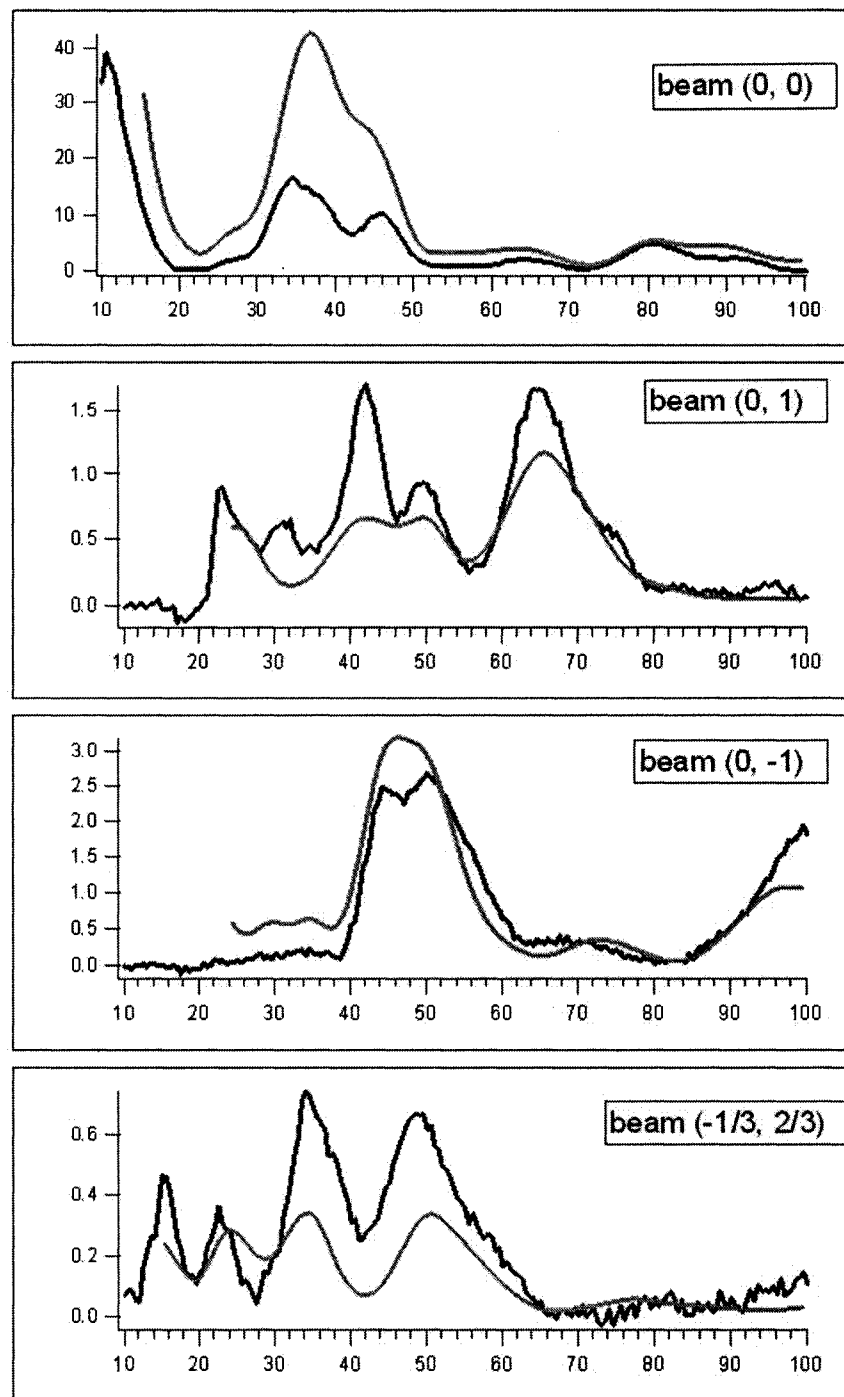
Figure B-9: Comparison of experimental (black) and calculated (gray) IV curves for the 6H-SiC(0001)-$\sqrt{3} \times \sqrt{3}$ surface.

resolve this structure. A mixed Si-vacancy top-site overlayer on 1×1 surface is found. A $\sqrt{3}\times\sqrt{3}$ overlayer at the T4 registry on the substrate surface generates a best fit between experimental and calculated data. Tests of these LEEM analyses are expected to pave the way to study the interface between SiC and graphene and reveal the graphene growth mechanism.

LIST OF REFERENCES

[1] Eremeev, S. V., Rusina, G. G. & Chulkov, E. V. Diffusion properties of Cu(001)-$c(2\times2)$-Pd surface alloys. *Surf. Sci.* **601**, 3640–3644 (2007).

[2] Barnes, C., AlShamaileh, E., Pitkänen, T., Kaukasoina, P. & Lindroos, M. The kinetics of formation and structure of an underlayer alloy: the Cu(100)-$c(2\times2)$-Pd system. *Surf. Sci.* **492**, 55–66 (2001).

[3] Zangwill, A. *Physics at Surfaces* (Cambridge Press Publisher, Cambridge, 1988).

[4] Tromp, R. M., Mankos, M., Reuter, M. C., Ellis, A. W. & Copel, M. A new low energy electron microscope. *Surface Review and Letters* **6**, 1189–1197 (1998).

[5] Ramanathan, K. G. & Srinivasan, T. M. Specific heat of bismuth at liquid helium temperatures. *Phys. Rev.* **99**, 442–443 (1955).

[6] SPECS. STM 150 Aarhus information online: `http://www.specs.de`.

[7] Prutton, M. *Introduction to Surface Physics* (Oxford University Press, USA, 1994).

[8] The Nobel Prize Organization online: `http://nobelprize.org/`.

[9] Duke, C. B. *Surface Science: The First Thirty Years* (North-Holland, North-Holland, 1994).

[10] Lüth, H. *Surfaces and interfaces of solids* (Springer, Berlin, New York, Springer-Verlag, 1993).

[11] Marie-Catherine, D. & Spanjaard, D. *Concepts in Surface Physics* (Springer, New York, 1998).

[12] Venables, J. *Introduction to surface and thin film processes* (Cambridge University Press, Cambridge, 2000).

[13] Plummer, E. W. `http://www.phys.utk.edu/WPWebSite/ewp_main.htm`.

[14] Plummer, E. W., Ismail, Matzdorf, R., Melechko, A. V., Pierce, J. P. & Zhang, J. Surfaces: a playground for physics with broken symmetry in reduced dimensionality. *Surface Science* **500**, 1–27 (2002).

[15] Riviére, J. C. *Surface analytical techniques* (Oxford University Press, New York, 1990).

[16] Davisson, C. & Germer, L. H. Diffraction of electrons by a crystal of nickel. *Phys. Rev.* **30**, 705–740 (1927).

[17] Pendry, J. B. *Low Energy Electron Diffraction* (Academic Press, London, 1974).

[18] Hove, M. A. V. & Tong, S. Y. *Surface Crystallography by LEED* (Springer-Verlag, berlin, 1979).

[19] Van Hove, M. A., Weinberg, W. H. & Chan, C. M. *Low-Energy Electron Diffraction* (Springer Verlag, New York, 1986).

[20] Slater, J. C. A simplification of the hartree-fock method. *Phys. Rev.* **81**, 385–390 (1951).

[21] Kohn, W. & Sham, L. J. Self-consistent equations including exchange and correlation effects. *Phys. Rev.* **140**, A1133–A1138 (1965).

[22] Slater, J. C. *Insulators, semiconductors and metals* (McGraw-Hill, New York, 1967).

[23] Herman, F. & Skillman, S. *Atomic structure calculations* (Prentice Hall, Englewood Cliffs, N. J., 1963).

[24] Clementi, E. *Ab initio* computations in atoms and molecules. *IBM Journal of Research and Development* **9**, 2–19 (1965).

[25] Loucks, T. *Augmented plane wave method* (Benjamin, New York, 1967).

[26] Snow, E. C. Self-consistent energy bands of silver by an augmented-plane-wave method. *Phys. Rev.* **172**, 708–711 (1968).

[27] Pendry, J. B. Ion core scattering and low energy electron diffraction – I. *Journal of Physics C: Solid State Physics* **4**, 2501–2513 (1971).

[28] Beeby, J. L. The diffraction of low-energy electrons by crystals. *J. Phys. C* **1**, 82–87 (1968).

[29] Tong, S. Y. & Hove, M. A. V. Unified computation scheme of low-energy electron diffraction - the combined-space method. *Phys. Rev. B* **16**, 1459 –1467 (1977).

[30] Tong, S. Y. Theory of low-energy electron diffraction. *Progress in Surface Science* **7**, 1–48 (1975).

[31] Pendry, J. B. Fast perturbation schemes for low energy electron diffraction spectra. *Journal of Physics C: Solid State Physics* **4**, 3095–3106 (1971).

[32] Pendry, J. B. Reliability factors for LEED calculations. *J. Phys. C* **13**, 937–944 (1980).

[33] Burchhardt, J., Nielsen, M. M., Adams, D. L., Lundgren, E. & Andersen, J. N. Structure of Al(111)-($\sqrt{3}\times\sqrt{3}$)R30 °-Na: A LEED study. *Phys. Rev. B* **50**, 4718–4724 (1994).

[34] Nielsen, M. M., Burchhardt, J. & Adams, D. L. Structure of Ni(100)-*c*(2×2)-Na: A LEED analysis. *Phys. Rev. B* **50**, 7851–7859 (1994).

[35] Nielsen, M. M., Christensen, S. V. & Adams, D. L. Substitutional adsorption of Li on Al: The structure of the Al(111)-($\sqrt{3} \times \sqrt{3}$)R30°-Li phase. *Phys. Rev. B* **54**, 17902–17909 (1996).

[36] Bevington, P. R. *Data reduction and error analysis for the physical sciences* (McGraw Hill, 1969).

[37] Adams, D. L. A simple and effective procedure for the refinement of surface structure in LEED. *Surf. Sci* **519**, 157–172 (2002).

[38] Adams, D. L. On the calculation of interlayer multiple scattering in LEED. *J. Phys. C* **16**, 6101–6110 (1983).

[39] Adams, D. L., Jensen, V., Sun, X. F. & Vollesen, J. H. multilayer relaxation of the Al(210) surface. *Phys. Rev. B* **38**, 7913–7931 (1988).

[40] Hanson, R. J. & Krogh, F. T. A quadratic-tensor model algorithm for nonlinear least-squares problems with linear constraints. *ACM Trans. Math. Softw* **18**, 115–133 (1992).

[41] Barbieri, A. & Hove, M. A. V. Phase shift package available online: http://electron.lbl.gov/leedpack/leedpack.html.

[42] Rous, P. J., Pendry, J. B., Saldin, D. K., Heinz, K., Müller, K. & Bickel, N. Tensor LEED: A technique for high-speed surface-structure determination. *Phys. Rev. Lett.* **57**, 2951–2954 (1986).

[43] Tong, S. Y., Huang, H., Wei, C. M., Packard, W. E., Men, F. K., Glander, G. & Webb, M. B. Low-energy electron diffraction analysis of the Si(111)7×7 structure. *Journal of Vacuum Science & Technology A: Vacuum, Surfaces, and Films* **6**, 615–624 (1988).

[44] Nascimento, V. B., Moore, R. G., Rundgren, J., Zhang, J., Cai, L., Jin, R., Mandrus, D. G. & Plummer, E. W. Procedure for LEED *I-V* structural analysis of metal oxide surfaces: $Ca_{1.5}Sr_{0.5}RuO_4(001)$. *Physical Review B* **75**, 035408–035418 (2007).

[45] Gavaza, G. M., Yu, Z. X., Tsang, L., Chan, C. H., Tong, S. Y. & Hove, M. A. V. Theory of low-energy electron diffraction for detailed structural determination of nanomaterials: Ordered structures. *Physical Review B* **75**, 014114–014124 (2007).

[46] Maria Blanco-Rey, G. H., Pedro de Andres & King, D. A. A FORTRAN-90 low-energy electron diffraction program (LEED90 v1.1). *Computer Physics Communications* **161**, 151–165 (2004).

[47] Bauer, E. *Electron Microscopy*, vol. 1 (Academic Press, Inc., New York, 1962).

[48] Telieps, W. & Bauer, E. An analytical reflection and emission uhv surface electron microscope. *Ultramicroscopy* **17**, 57–65 (1985).

[49] Telieps, W. & Bauer, E. The (7×7)↔(1×1) phase transition on Si(111). *Surf. Sci.* **162**, 163–168 (1985).

[50] Tromp, R. M. & Reuter, M. C. Design of a new photo-emission/low-energy electron microscope for surface studies. *Ultramicroscopy* **36**, 99–106 (1991).

[51] Tromp, R. M. Low-energy electron microscopy. *IBM J. RES. DEVELOP.* **44**, 503–516 (2000).

[52] Meyer zu Heringdorf, F.-J., Tromp, R. M. & Horn-von Hoegen, M. http://www.leem-user.com/.

[53] Bauer, E. Low energy electron microscopy. *Rep. Prog. Phys.* **57**, 895–938 (1994).

[54] Tromp, R. M. & Hannon, J. B. http://www.research.ibm.com/leem//.

[55] SPECS. FE-LEEM P90 information online: http://www.specs.de/.

[56] Rundgren, J. Electron inelastic mean free path, electron attenuation length, and low-energy electron-diffraction theory. *Phys. Rev. B* **59**, 5106–5114 (1999).

[57] Hedin, L. & Lundqvist, B. I. Explicit local exchange-correlation potentials. *Journal of Physics C: Solid State Physics* **4**, 2064–2083 (1971).

[58] Watson, R. E., Herbst, J. F., Hodges, L., Lundqvist, B. I. & Wilkins, J. W. Effect of ground-state and excitation potentials on energy levels of Ni metal. *Phys. Rev. B* **13**, 1463–1467 (1976).

[59] Neve, J., Rundgren, J. & Westrin, P. A cluster and DVM approach to the generation of LEED potentials: application to Al(111) and Al(111)p(1×1)O. *Journal of Physics C: Solid State Physics* **15**, 4391–4401 (1982).

[60] Segre, E. *The collected works of Enrico Fermi* (The University of Chicago Press, Chicago, 1965).

[61] Anderson, H. A. Metropolis, Monte Carlo and the MANIAC. *Los Alamos Science* **14**, 69–81 (1986).

[62] Metropolis, N., Rosenbluth, A. W., Rosenbluth, M. N., Teller, A. H. & Teller, E. Equation of state calculations by fast computing machines. *J. Phys. Chem.* **21**, 1087–1092 (1953).

[63] Matsumoto, M. & Nishimura, T. Mersenne twister: a 623-dimensionally equidistributed uniform pseudorandom number generator. *ACM Trans. Model. Comput. Simul.* **8**, 3–30 (1998).

[64] Ashcroft, N. E. & Mermin, N. D. *Solid state physics* (Saunders College, Philadelphia, 1976).

[65] Shick, A. B., Ketterson, J. B., Novikov, D. L. & Freeman, A. J. Electronic structrue, phase stability, and semimetal-semiconductor transtitions in Bi. *Physical Review B* **60**, 15484–15487 (1999).

[66] Agergaard, S., Søndergaard, C., Li, H., Nielsen, M. B., Hoffmann, S. V., Li, Z. & Hofmann, P. The effect of reduced dimensionality on a semimetal: the electronic structure of the Bi(110) surface. *New Journal of Physics* **3**, 15.1–15.10 (2001).

[67] Hofmann, P., Gayone, J. E., Bihlmayer, G., Koroteev, Y. M. & Chulkov, E. V. Electronic structure and fermi surface of Bi(100). *Physical Review B* **71**, 195413–195419 (2005).

[68] Hengsberger, M., Segovia, P., Garnier, M., Purdie, D. & Baer, Y. Photoemission study of the carrier bands in Bi(111). *The European Physical Journal B* **17**, 603–608 (2000).

[69] Ast, C. R. & Höchst, H. Fermi surface of Bi(111) measured by photoemission spectroscopy. *Phys. Rev. Lett.* **87**, 177602–177605 (2001).

181

[70] Hofmann, P. The surfaces of bismuth: Structural and electronic properties. *Progress in Surface Science* **81**, 191–245 (2006).

[71] Gonze, X., Michenaud, J.-P. & Vigneron, J.-P. First-principles study of As, Sb, and Bi electronic properties. *Physical Review B* **41**, 11827–11836 (1990).

[72] Koroteev, Y. M., Bihlmayer, G., Gayone, J. E., Chulkov, E. V., Blügel, S., Echenique, P. M. & Hofmann, P. Ubiquitous strong spin-orbit splitting on Bi surfaces. *Phys. Rev. Lett.* **93**, 046403–046406 (2004).

[73] Pascual, J. I., Bihlmayer, G., Koroteev, Y. M., Rust, H.-P., Ceballos, G., Hansmann, M., Horn, K., Chulkov, E. V., Blügel, S., Echenique, P. M. & Hofmann, P. Role of the spin in quasiparticle interference. *Phys. Rev. Lett.* **93**, 196802–196805 (2004).

[74] Orgin, Y. F., Lutskii, V. N. & Elinson, M. I. Observation of quantum size effects in thin bismuth films. *JETP Letters* **3**, 71–73 (1966).

[75] Hoffman, C. A., Meyer, J. R., Bartoli, F. J., Venere, A. D., Xi, X. J., Hou, C. L. & Wang, H. C. Semimetal-to-semiconductor transition in bismuth thin films. *Phys. Rev. B* **48**, 11431–11434 (1993).

[76] Dresselhaus, M. S., Lin, Y. M., Rabin, O., Jorio, A., Filho, A. G. S., Pimenta, M. A., Saito, R., Samsonidze, G. & Dresselhaus, G. Nanowires and nanotubes. *Materials Science and Engineering: C* **15**, 129–140 (2003).

[77] Weitzel, B. & Micklitz, H. Superconductivity in granular systems buil from well-defined rhombohedral Bi clusters: Evidence for Bi-surface superconductivity. *Physical Review Letters* **66**, 385–388 (1991).

[78] Nagao, T., Sadowski, J. T., Saito, M., Yaginuma, S., Fujikawa, Y., Kogure, T., Ohno, T., Hasegawa, Y., Hasegawa, S. & Sakurai, T. Nanofilm allotrope and phase transformation of ultrathin Bi film on Si(111)-7×7. *Phys. Rev. Lett.* **93**, 105501–105504 (2004).

[79] Sadowski, J. T., Nagao, T., Yaginuma, S., Fujikawa, Y., Al-Mahboob, A., Nakajima, K., Sakurai, T., Thayer, G. E. & Tromp, R. M. Thin bismuth film as a template for pentacene growth. *Applied Physics Letters* **86**, 073109–073111 (2005).

[80] Jona, F. Low-energy electron diffraction study of surfaces of antimony and bismuth. *Surface Science* **8**, 57–76 (1967).

[81] Mönig, H., Sun, J., Koroteev, Y. M., Bihlmayer, G., Wells, J., Chulkov, E. V., Pohl, K. & Hofmann, P. Structure of the (111) surface of bismuth: LEED analysis and first-principles calculations. *Physical Review B* **72**, 085410–085416 (2005).

[82] Sun, J., Mikkelsen, A., Jensen, M. F., Koroteev, Y. M., Bihlmayer, G., Chulkov, E. V., Adams, D. L., Hofmann, P. & Pohl, K. Structural determination of the Bi(110) semimetal surface by LEED analysis and *ab initio* calculations. *Physical Review B* **74**, 245406–245413 (2006).

[83] Liu, Y. & Allen, R. E. Electronic structure of the semimetals Bi and Sb. *Phys. Rev. B* **52**, 1566–1577 (1995).

[84] Ast, C. R. & Höchst, H. Electronic structure of a bismuth bilayer. *Phys. Rev. B* **67**, 113102–113105 (2003).

[85] Edelman, V. S., Sharvin, D. Y., Khlyustikov, I. N. & Troyanovskii, A. M. STM revealing of twin microlayers with quantized width on cleaved bismuth surface. *Europhys. Lett.* **34**, 115–120 (1996).

[86] Cucka, P. & Barrett, C. S. The crystal structure of Bi and of solid solutions of Pb, Sn, Sb and Te in Bi. *Acta. Cryst.* **15**, 865–872 (1962).

[87] Erfling, H. D. Studies of the thermal expansion of solids at low temperatures. ii. chromium, β-manganese, molybdenum, rhodium, beryllium, graphite, thallium, zirconium, bismuth, antimony, tin and beryl. *Ann. Phys.* **34**, 136–160 (1939).

[88] Krakauer, H., Posternak, M. & Freeman, A. J. Linearized augmented plane-wave method for the electronic band structure of thin films. *Phys. Rev. B* **19**, 1706–1719 (1979).

[89] Wimmer, E., Krakauer, H., Weinert, M. & Freeman, A. J. Full-potential self-consistent linearized-augmented-plane-wave method for calculating the electronic structure of molecules and surfaces: O_2 molecule. *Phys. Rev. B* **24**, 864–875 (1981).

[90] Moruzzi, V. L., Janak, J. F. & Williams, A. R. *Calculated Electronic Properties of Metals* (Pergamon, New York, 1978).

[91] Li, C., Freeman, A. J., Jansen, H. J. F. & Fu, C. L. Magnetic anisotropy in low-dimensional ferromagnetic systems: Fe monolayers on Ag(001), Au(001), and Pd(001) substrates. *Phys. Rev. B* **42**, 5433–5442 (1990).

[92] Nielsen, H. B. & Adams, D. L. r-factor analysis of the effect of non-structural parameters in LEED, applied to Al(111). *J. Phys. C:* **15**, 615–632 (1982).

[93] Ast, C. R. & Höchst, H. Indication of charge-density wave formation on Bi(111). *Phys. Rev. Lett.* **90**, 016403– 016406 (2003).

[94] Goodman, R. M. & Somorjai, G. A. Low-energy electron diffraction studies of surface melting and freezing of lead, bismuth and tin single-crystal surfaces. *J. Chem. Phys.* **52**, 6325–6331 (1970).

[95] Ast, C. R. & Höchst, H. Two-dimensional band structure and self-energy of Bi(111) near the $\bar{\Gamma}$ point. *Phys. Rev. B* **66**, 125103–125111 (2002).

[96] Gayone, J. E., Kirkegaard, C., Wells, J. W., Hoffmann, S. V., Li, Z. & Hofmann, P. Determining the electron-phonon mass enhancement parameter λ on metal surfaces. *Applied Physics A* **80**, 943–949 (2005).

[97] Andersen, J. N., Nielsen, H. B., Petersen, L. & Adams, D. L. Oscillatory relaxation of the Al(110) surface. *J. Phys. C* **17**, 173–192 (1984).

[98] Jona, F., Shih, H. D., Jepsen, D. W. & Marcus, P. M. On the structure of reconstructed Si(001)2×1 and Ge(001)2×1 surfaces. *J. Phys. C: Solid State Phys.* **12**, L455–L461 (1979).

[99] Jezequel, G., Barski, A., Steiner, P., Solal, F., Roubin, P., Pinchaux, R. & Petroff, Y. Indirect transitions in angle-resolved photoemission. *Physical Review B* **30**, 4833–4836 (1984).

[100] Y.M. Koroteev, G. B. & Chulkov, E. *private communication.* .

[101] Walfried, C., McIlroy, D. N., Zhang, J., Dowben, P. A., Katrich, G. A. & Plummer, E. W. Determination of the surface Debye temperature of Mo(112) using valence band photoemission. *Surface Science* **363**, 296–302 (1996).

[102] Kirkegaard, C., Kim, T. K. & Hofmann, P. Self-energy determination and electron-phonon coupling on Bi(110). *New Journal of Physics* **7**, 99-1–22 (2005).

[103] Kim, T. K., Sorensen, T. S., Wolfring, E., Li, H., Chulkov, E. V. & Hofmann, P. Electron-phonon coupling on the Mg(0001) surface. *Physical Review B* **72**, 075422 (2005).

[104] Besenbacher, F. Scanning tunnelling microscopy studies of metal surfaces. *Reports on Progress in Physics* **59**, 1737–1802 (1996).

[105] Campbell, C. T. Bimetallic surface chemistry. *Annual Review of Physical Chemistry* **41**, 775–837 (1990).

[106] Bardi, U. The atomic structure of alloy surfaces and surface alloys. *Rep. Prog. Phys.* **57**, 939 (1994).

[107] Woodruff, D. P. Photoelectron diffraction: past, present and future. *Journal of Electron Spectroscopy and Related Phenomena* **126**, 55–65 (2002).

[108] Neugebauer, J. & Scheffler, M. Mechanisms of island formation of alkali-metal adsorbates on Al(111). *Phys. Rev. Lett.* **71**, 577–580 (1993).

[109] Stampfl, C., Scheffler, M., Over, H., Burchhardt, J., Nielsen, M., Adams, D. L. & Moritz, W. Identification of stable and metastable adsorption sites of K adsorbed on Al(111). *Phys. Rev. Lett.* **69**, 1532–1535 (1992).

[110] Pleth Nielsen, L., Besenbacher, F., Stensgaard, I., Laegsgaard, E., Engdahl, C., Stoltze, P., Jacobsen, K. W. & Nørskov, J. K. Initial growth of Au on Ni(110): Surface alloying of immiscible metals. *Phys. Rev. Lett.* **71**, 754–757 (1993).

[111] Röder, H., Schuster, R., Brune, H. & Kern, K. Monolayer-confined mixing at the Ag-Pt(111) interface. *Phys. Rev. Lett.* **71**, 2086–2089 (1993).

[112] Oppo, S., Fiorentini, V. & Scheffler, M. Theory of adsorption and surfactant effect of Sb on Ag(111). *Phys. Rev. Lett.* **71**, 2437–2440 (1993).

[113] Leviness, S., Nair, V., Weiss, A. H., Schay, Z. & Guczi, L. Acetylene hydrogenation selectivity control on PdCu/Al$_2$O$_3$ catalysts. *J. Molecular Catalysis* **25**, 131–140 (1983).

[114] Ponec, V. Cu and Pd, two catalysts for CH$_3$OH synthesis: the similarities and the differences. *Surf. Sci.* **272**, 111–117 (1992).

[115] Park, C. W. & Vook, R. W. Electromigration-resistant Cu-Pd alloy films. *Thin Solid Films* **226–247**, 238–247 (1993).

[116] Hu, C., Gignac, L., Rosenberg, R., Liniger, E., Rubino, J., Sambucetti, C., Domenicucci, A., Chen, X. & Stamper, A. K. Reduced electromigration of Cu wires by surface coating. *Applied Physics Letters* **81**, 1782–1784 (2002).

[117] Koymen, A. R., Lee, K. H., Yang, G., Jensen, K. O. & Weiss, A. H. Temperature-dependent top-layer composition of ultrathin Pd films on Cu(100). *Phys. Rev. B* **48**, 2020–2023 (1993).

[118] Smith, G. C., Norris, C. & Binns, C. The electron states of ultra-thin Pd overlayers on Cu(100) and Ag(111). *Vacuum* **31**, 523–524 (1981).

[119] Graham, G. W. Carbon monoxide chemisorption on Cu(100)-c(2×2)Pd. *Surf. Sci.* **171**, L432 (1986).

[120] Lu, S. H., Wang, Z. Q., Wu, S. C., Lok, C. K. C., Quinn, J., Li, Y. S., Tian, D., Jona, F. & Marcus, P. M. Structural and electronic properties of a surface alloy of Pd and Cu on Cu{001}. *Phys. Rev. B* **37**, 4296–4298 (1988).

[121] Pope, T. D., Griffiths, K. & Norton, P. R. Surface and interfacial alloys of Pd with Cu(100): structure, photoemission and CO chemisorption. *Surf. Sci.* **306**, 294–312 (1994).

[122] Pope, T. D., Griffiths, K., Zhdanov, V. P. & Norton, P. R. Kinetics of surface alloy formation: Cu(100)-$c(2\times2)$Pd. *Phys. Rev. B* **50**, 18553 (1994).

[123] Pope, T. D., Vos, M., Tang, H. T., Griffiths, K., Mitchell, I. V., Norton, P. R., Liu, W., Li, Y. S., Mitchell, K. A. R., Tian, Z. J. & Black, J. B. A structural study of Pd/Cu(100) surface alloys. *Surf. Sci.* **337**, 79–91 (1995).

[124] Murray, P. W., Stensgaard, I., Lægsgaard, E. & Besenbacher, F. Growth and structure of Pd alloys on Cu(100). *Surf. Sci.* **365**, 591–601 (1996).

[125] Hannon, J. B., Ibach, H. & Stoltze, P. Vibrational modes of the Cu(100)-$c(2\times2)$-Pd surface. *Surf. Sci.* **355**, 63–70 (1996).

[126] Shen, Y. G., Yao, J., O'Connor, D. J., King, B. V. & MacDonald, R. J. Au-segregated dealloying and Pd-induced clock reconstructing of Cu(001). *J. Phys.: Condens. Matter* **8**, 4903 (1996).

[127] Valden, M., Aaltonen, J., Pessa, M., Gleeson, M. & Barnes, C. J. Heterogeneity in the surface structure of a Cu(100)-$c(2\times2)$-Pd surface alloy. *Chem. Phys. Lett.* **228**, 519–526 (1994).

[128] Kudrnovský, J., Bose, S. K. & Drchal, V. Origins of surface alloy formation: Cu(001)-$c(2\times2)$-Pd as a case study. *Phys. Rev. Lett.* **69**, 308–311 (1992).

[129] Black, J. E. & Tian, Z. J. Palladium atoms on a copper surface: A molecular dynamics study. *Comments Cond. Mat. Phys* **16**, 281 (1993).

[130] Bilić, A., Shen, Y. G., King, B. V. & O'Connor, D. J. Embedded atom method study of Pd thin films on Cu(001). *Surf. Rev. Lett.* **5**, 959 (1998).

[131] Garcés, J. E., Mosca, H. O. & Bozzolo, G. H. Atomistic modeling of Pd/Cu(100) surface alloy formation. *Surf. Sci.* **459**, 365 (2000).

[132] Harrison, M. J., Woodruff, D. P. & Robinson, J. Surface alloys, surface rumpling and surface stress. *Surf. Sci.* **572**, 309 (2004).

[133] Eremeev, S. V., Rusina, G. G., Sklyadneva, I. Y., Borisova, S. D. & Chulkov, E. V. Diffusional and vibrational properties of Cu(001)-$c(2\times2)$-Pd surface alloys. *Physics of The Solid State* **47**, 758–764 (2005).

[134] Li, L., Xun, K., Zhou, Y., Wang, D. & Wu, S. First-principles calculation of the atomic and electronic structure of the surface alloy Cu(001)$c(2\times2)$-Pd. *Phys. Rev. B* **71**, 075406 (2005).

[135] Wang, Z. Q., Li, Y. S., Lok, C. K. C., Quinn, J., Jona, F. & Marcus, P. M. Atomic and electronic structure of a surface alloy–comparison with the bulk alloy. *Solid State Communications* **62**, 181–186 (1987).

[136] Chambliss, D. D., Wilson, R. J. & Chiang, S. Nucleation and growth of ultrathin Fe and Au films on Cu(100) studied by scanning tunneling microscopy. vol. 10, 1993–1998 (AVS, 38th National Symposium of the American Vacuum Society, 1992).

189

[137] Chambliss, D. D. & Chiang, S. Surface alloy formation studied by scanning tunneling microscopy: Cu(100)+Au-$c(2\times2)$. *Surf. Sci.* **264**, L187–L192 (1992).

[138] D. Naumovich, T. G. J. O., A. Stuck & Schlapbach, L. Erratum to 'submonolayer films of Au on Cu(001) studied by photoelectron diffraction'. *Surf. Sci.* **277**, 235–235 (1992).

[139] D. Naumovich, T. G. J. O., A. Stuck & Schlapbach, L. Submonolayer films of Au on Cu(001) studied by photoelectron diffraction. *Surf. Sci.* **269-270**, 719–723 (1992).

[140] P. Hu, L. M. d. l. G. M. P. B., A. Wander & King, D. A. An adsorbate-stabilised vacancy structure for Cu on W{100}: A surface alloy. *Surf. Sci.* **286**, L542–L546 (1993).

[141] Wuttig, M., Gauthier, Y. & Blügel, S. Magnetically driven buckling and stability of ordered surface alloys: Cu(100)-$c(2\times2)$Mn. *Phys. Rev. Lett.* **70**, 3619–3622 (1993).

[142] M. Wuttig, T. F., C. C. Knight & Gauthier, Y. LEED structure determination of two ordered surface alloys: Cu(100)-$c(2\times2)$Mn and Ni(100)-$c(2\times2)$Mn. *Surf. Sci.* **292**, 189–195 (1993).

[143] Wuttig, M. & Knight, C. C. LEED structure determination of tetragonal MnNi films on Ni(100). *Phys. Rev. B* **48**, 12130–12135 (1993).

[144] D. Tian, R. F. L., Jona, F. & Marcus, P. M. A low-energy electron diffraction study of the Pd{001}$c(2\times2)$-Mn adsorbed system. *Solid State Communications* **74**, 1017–1020 (1990).

[145] Aminpirooz, S., Schmalz, A., Becker, L., Pangher, N., Haase, J., Nielsen, M. M., Batchelor, D. R., Bo/gh, E. & Adams, D. L. Temperature-dependent local geometries

in the system Al(100)-$c(2\times2)$-Na: A surface extended X-ray-absorption fine-structure study. *Phys. Rev. B* **46**, 15594–15597 (1992).

[146] Bauer, E., Poppa, H., Todd, G. & Davis, P. R. The adsorption and early stages of condensation of Ag and Au on W single-crystal surfaces. *Journal of Applied Physics* **48**, 3773–3787 (1977). URL http://link.aip.org/link/?JAP/48/3773/1.

[147] Soria, F. & Poppa, H. Comparison of the early stages of condensation of Cu and Ag on Mo(100) with Cu and Ag on W(100). *Journal of Vacuum Science and Technology* **17**, 449–452 (1980). URL http://link.aip.org/link/?JVS/17/449/1.

[148] Bardi, U. & Ross, P. N. Superlattice leed patterns observed from [111] and [100] oriented single crystals of TiPt₃. *Surf. Sci.* **146**, L555–L560 (1984).

[149] Wu, S. C., Lu, S. H., Wang, Z. Q., Lok, C. K. C., Quinn, J., Li, Y. S., Tian, D., Jona, F. & Marcus, P. M. Cu{001} $c(2\times2)$-Pd: An ordered surface alloy. *Phys. Rev. B* **38**, 5363 (1988).

[150] Murray, P. W., Stensgaard, I., Lægsgaard, E. & Besenbacher, F. Mechanisms of initial alloy formation for pd on Cu(100) studied by STM. *Phys. Rev. B* **52**, R14404–R14414 (1995).

[151] AlShamaileh, E., Barnes, C. & Wander, A. Cu-capped surface alloys of Pt/Cu{100}. *J. Phys.: Condens. Matter* **15**, 1879–1887 (2003).

[152] Alonso, J. A. & March, N. H. *Electrons in Metals and Alloys* (Academic, London, 1989).

[153] Graham, G. W., Schmitz, P. J. & Thiel, P. A. Growth of Rh, Pd, and Pt films on Cu(100). *Phys. Rev. B* **41**, 3353 (1990).

[154] Anderson, G. W., Pope, T. D., Jensen, K. O., Griffiths, K., Norton, P. R. & Schultz, P. J. Annealing properties of the 0.5-ML Pd/Cu(100) surface alloy. *Phys. Rev. B* **48**, 15283 (1993).

[155] Goapper, S., Barbier, L. & Salanon, B. Step pairing induced by surface alloying: Pd/Cu(1, 1, 11). *Surf. Sci.* **409**, 81 (1998).

[156] Sklyadneva, I. Y., Rusina, G. G. & Chulkov, E. V. Vibrational properties of $Cu(100)-c(2 \times 2) - Pd$ surface and subsurface alloys. *Phys. Rev. B* **68**, 045413 (2003).

[157] Shustorovich, E. *Metal-Surface Reaction Energetics: Theory and Applications to Heterogeneous Catalysis, Chemisorption, and Surface Diffusion* (VCH Publishers, Inc., New York, 1991).

[158] Oura, K., Lifshits, V., Saranin, A., Zotov, A. & Katayama, M. *Surface Science: An Introduction* (Springer-Verlag, Berlin Heidelberg, 2003).

[159] Antczaka, G. & Ehrlicha, G. Jump processes in surface diffusion. *Surf. Sci. Rep.* **62**, 39–61 (2007).

[160] Shewmon, P. G. *Diffusion in solids* (McGraw-Hill, New York, 1963).

[161] Christian, J. W. *The theory of Transformations in Metals and Alloys Part I.* (Pergamon, New York, 2002).

[162] Wrigley, J. D. & Ehrlich, G. Surface diffusion by an atomic exchange mechanism. *Phys. Rev. Lett.* **44**, 661–663 (1980).

[163] Kellogg, G. L. & Feibelman, P. J. Surface self-diffusion on Pt(001) by an atomic exchange mechanism. *Phys. Rev. Lett.* **64**, 3143–3146 (1990).

[164] Schmid, A. K., Hamilton, J. C., Bartelt, N. C. & Hwang, R. Q. Surface alloy formation by interdiffusion across a linear interface. *Phys. Rev. Lett.* **77**, 2977–2980 (1996).

[165] Flores, T., Junghans, S. & Wuttig, M. Atomic mechanisms of the diffusion of Mn atoms incorporated in the Cu(100) substrate: an STM study. *Surf. Sci.* **371**, 1–13 (1997).

[166] Flores, T., Junghans, S. & Wuttig, M. Atomic mechanisms of the formation of an ordered surface alloy: an STM investigation of Mn/Cu(100). *Surf. Sci.* **371**, 14–29 (1997).

[167] Hannon, J. B., Klünker, C., Giesen, M., Ibach, H., Bartelt, N. C. & Hamilton, J. C. Surface self-diffusion by vacancy motion: Island ripening on Cu(001). *Phys. Rev. Lett.* **79**, 2506–2509 (1997).

[168] Klünker, C., Hannon, J. B., Giesen, M., Ibach, H., Boisvert, G. & Lewis, L. J. Activation energy for the decay of two-dimensional islands on Cu(100). *Phys. Rev. B* **58**, R7556–7559R (1998).

[169] van Gastel, R., Somfai, E., van Albada, S. B., van Saarloos, W. & Frenken, J. W. M. Nothing moves a surface: Vacancy mediated surface diffusion. *Phys. Rev. Lett.* **86**, 1562–1565 (2001).

[170] Grant, M. L., Swartzentruber, B. S., Bartelt, N. C. & Hannon, J. B. Diffusion kinetics in the Pd/Cu(001) surface alloy. *Phys. Rev. Lett.* **86**, 4588–4591 (2001).

[171] Anderson, M. L., D'Amato, M. J., Feibelman, P. J. & Swartzentruber, B. S. Vacancy-mediated and exchange diffusion in a Pb/Cu(111) surface alloy: Concurrent diffusion on two length scales. *Phys. Rev. Lett.* **90**, 126102 (2003).

[172] Bourassa, R. R. & Lengeler, B. The formation and migration energies of vacancies in quenched copper. *J. Phys. F: Met. Phys.* **6**, 1405–1413 (1976).

[173] Jona, F., Legg, K. O., Shih, H. D., Jepsen, D. W. & Marcus, P. M. Random occupation of adsorption sites in the $c(2\times2)$ structure of CO on Fe(001). *Phys. Rev. Lett.* **40**, 1466–1469 (1978).

[174] Crampin, S. & Rous, P. J. The validity of the average t-matrix approximation for low-energy electron diffraction from random alloys. *Surf. Sci. Lett.* **244**, L137–L142 (1991).

[175] Sun, J., Hannon, J. B., Kellogg, G. L. & Pohl, K. Local structural and compositional determination via electron scattering: Heterogeneous Cu(001)-Pd surface alloy. *Physical Review B* **76**, 205414–205423 (2007).

[176] Demuth, J. E., Marcus, P. M. & Jepsen, D. W. Analysis of low-energy-electron-diffraction intensity spectra for (001), (110), and (111) nickel. *Phys. Rev. B* **11**, 1460–1474 (1975).

[177] Noonan, J. R., Davis, H. L. & Jenkins, L. H. LEED analysis of a Cu(110) surface. *J. Vac. Sci. Technol.* **15**, 619–621 (1978).

[178] Davis, H. L. & Noonan, J. R. Cu(100) multilayer relaxation. *J. Vac. Sci. Technol.* **20**, 842–845 (1982).

[179] Walter, S., Blum, V., Hammer, L., Müller, S., Heinz, K. & Giesen, M. The role of an energy-dependent inner potential in quantitative low-energy electron diffraction. *Surf. Sci.* **458**, 155–161 (2000).

[180] Lind, D. M., Dunning, F. B. & Walters, G. K. Surface-structural analysis by use of spin-polarized low-energy electron diffraction: An investigation of the Cu(100) surface. *Phys. Rev. B* **35**, 9037–9044 (1987).

[181] Jiang, Q. T., Fenter, P. & Gustafsson, T. Geometric structure and surface vibrations of Cu(001) determined by medium-energy ion scattering. *Phys. Rev. B* **44**, 5773–5778 (1991).

[182] Hannon, J. B., Sun, J., Pohl, K. & Kellogg, G. L. The origins of nanoscale heterogeneity in ultra-thin films. *Phys. Rev. Lett.* **96**, 246103–246106 (2006).

[183] Frenkel, D. & Smit, B. *Understanding Molecular Simulation From Algorithms to Applications* (Academic Press, San Diego, 2002).

[184] Chadi, D. J. Atomic and electronic structures of reconstructed Si(100) surfaces. *Phys. Rev. Lett.* **43**, 43–47 (1979).

[185] Tromp, R. M., Hamers, R. J. & Demuth, J. E. Si(001) dimer structure observed with scanning tunneling microscopy. *Phys. Rev. Lett.* **55**, 1303–1306 (1985).

[186] Schlier, R. E. & Farnsworth, H. E. Structure and adsorption characteristics of clean surfaces of germanium and silicon. *The Journal of Chemical Physics* **30**, 917–926 (1959).

[187] Lander, J. J. & Morrison, J. Low-energy electron-diffraction study of silicon surface structures. *Journal of Chemical Physics* **37**, 729–746 (1962).

[188] Landemark, E., Karlsson, C. J., Chao, Y.-C. & Uhrberg, R. I. G. Core-level spectroscopy of the clean Si(001) surface: Charge transfer within asymmetric dimers of the 2×1 and c(4×2) reconstructions. *Phys. Rev. Lett.* **69**, 1588–1591 (1992).

[189] Wolkow, R. A. Direct observation of an increase in buckled dimers on Si(001) at low temperature. *Phys. Rev. Lett.* **68**, 2636–2639 (1992).

[190] Yin, M. T. & Cohen, M. L. Theoretical determination of surface atomic geometry: Si(001)-(2×1). *Phys. Rev. B* **24**, 2303–2306 (1981).

[191] Northrup, J. E. Electronic structure of Si(100)c(4×2) calculated within the GW approximation. *Phys. Rev. B* **47**, 10032–10035 (1993).

[192] Uhrberg, R. I. G., Hansson, G. V., Nicholls, J. M. & Flodström, S. A. Experimental studies of the dangling- and dimer-bond-related surface electron bands on Si(100) (2×1). *Phys. Rev. B* **24**, 4684–4691 (1981).

[193] Hamers, R. J. & Kohler, U. K. Determination of the local electronic structure of atomic-sized defects on Si(001) by tunneling spectroscopy. *Journal of Vacuum Science & Technology A: Vacuum, Surfaces, and Films* **7**, 2854–2859 (1989).

[194] Wertheim, G. K., Riffe, D. M., Rowe, J. E. & Citrin, P. H. Crystal-field splitting and charge flow in the buckled-dimer reconstruction of Si(100)2×1. *Phys. Rev. Lett.* **67**, 120–123 (1991).

[195] Tong, S. Y. & Maldonado, A. L. The structure of Si(001)-2×1 surface - studied by low energy electron diffraction. *Surface Science* **78**, 459–466 (1978).

[196] White, S. J., Frost, D. C. & Mitchell, K. A. R. LEED investigations of some models for reconstructed (100) surfaces of silicon. *Solid State Communications* **42**, 763–765 (1982).

[197] Yang, W. S., Jona, F. & Marcus, P. M. Atomic structure of Si(001)2×1. *Phys. Rev. B* **28**, 2049–2059 (1983).

[198] Holland, B. W., Duke, C. B. & Paton, A. The atomic geometry of Si(100)-(2×1) revisited. *Surface Science* **140**, L269–L278 (1984).

[199] Ignatiev, A., Jona, F., Debe, M., Johnson, D. E., White, S. J. & Woodruff, D. P. Three independent LEED studies of clean Si(100) surfaces. *Journal of Physics C: Solid State Physics* **10**, 1109–1119 (1977).

[200] Over, H., Wasserfall, J., Ranke, W., Ambiatello, C., Sawitzki, R., Wolf, D. & Moritz, W. Surface atomic geometry of Si(001)-(2×1): A low-energy electron-diffraction structure analysis. *Phys. Rev. B* **55**, 4731–4736 (1997).

[201] Mikkelsen, A. *Ph.D dissertation. Chapter 8.* (Aarhus, 2004).

[202] Grykol, J. & Allen, R. E. Dimer switching on Si(100). *Ultramicroscopy* **42-44**, 793–800 (1992).

[203] de La Figuera, J., Puerta, J. M., Cerda, J. I., El Gabaly, F. & McCarty, K. F. Determining the structure of Ru(0001) from low-energy electron diffraction of a single terrace. *Surface Science* **600**, L105–L109 (2006).

[204] Moritz, W. Effective calculation of LEED intensities using symmetry-adapted functions. *Journal of Physics C: Solid State Physics* **17**, 353–362 (1984).

[205] G. Kleinle, W. M. & Ertl, G. An efficient method for LEED crystallography. *Surface Science* **238**, 119–131 (1990).

[206] Over, H., Ketterl, U., Moritz, W. & Ertl, G. Optimization methods and their use in low-energy electron-diffraction calculations. *Phys. Rev. B* **46**, 15438–15446 (1992).

[207] M. Gierer, H. O. & Moritz, W. *Private communication* .

[208] Moritz, W. *Private communication* .

[209] Rundgren, J. Optimized surface-slab excited-state muffin-tin potential and surface core level shifts. *Phys. Rev. B* **68**, 125405–125413 (2003).

[210] Tanuma, S. & C. J. Powell, D. R. P. Calculations of electron inelastic mean free paths. II. data for 27 elements over the 50 - 2000 eV. *Surf. Interface Anal* **17**, 911–926 (1991).

[211] Choyke, W. J., Matsunami, H. & Pensl, G. *Silicon Carbide* (Springer, New York, 2004).

[212] Berger, C., Song, Z., Li, X., Wu, X., Brown, N., Naud, C., Mayou, D., Li, T., Hass, J., Marchenkov, A. N., Conrad, E. H., First, P. N. & de Heer, W. A. Electronic Confinement and Coherence in Patterned Epitaxial Graphene. *Science* **312**, 1191–1196 (2006).

[213] Forbeaux, I., Themlin, J.-M. & Debever, J.-M. Heteroepitaxial graphite on 6H-SiC(0001): Interface formation through conduction-band electronic structure. *Phys. Rev. B* **58**, 16396–16406 (1998).

[214] Schardt, J., Bernhardt, J., Starke, U. & Heinz, K. Crystallography of the (3×3) surface reconstruction of 3c-SiC(111), 4H-SiC(0001), and 6H-SiC(0001) surfaces retrieved by low-energy electron diffraction. *Phys. Rev. B* **62**, 10335–10344 (2000).

[215] Deng, B., Chen, Y. & Xu, G. Study on ($\sqrt{3} \times \sqrt{3}$)-R30° reconstruction of 6H-SiC(0001) surface by ATLEED. *ACTA PHYSICA SINICA* **50**, 106–110 (2001).